Inhomogeneous phenomena in nematic liquid crystals

A Thesis submitted to the
Board of Studies in Physical Sciences
for the degree of

Doctor of Philosophy

of

Homi Bhabha National Institute

By,

Amit Kumar Bhattacharjee

The Institute of Mathematical Sciences
Chennai, India

2010

Declaration

We hereby certify that we have read this dissertation prepared under our direction and recommend that it may be accepted as fulfilling the dissertation requirement.

Ronojoy Adhikari

Gautam I. Menon

I hereby declare that the presented research work in this thesis has been carried out by me except otherwise specified in the thesis, under the guidance of my thesis advisors Dr. R. Adhikari and Dr. G. I. Menon. The work is original and has not been submitted earlier as a whole or in part of a degree / diploma at this or any other Institution / University.

Amit Kumar Bhattacharjee

September 2010,
The Institute of Mathematical Sciences,
Chennai 600 113, India

ACKNOWLEDGEMENTS

I thank my advisors for introducing me to a few of the most intricate and fascinating problems in the mesoscale physics of soft matter. Their guidance, patience and perseverance has been an example to keep me focused to my research work in the most difficult years of graduate studies. Their clear explanation of scientific ideas, way of teaching, careful analysis of my never ending queries made my basic understanding of the theoretical framework, relating the research problem with the very first principles of the subject. While it was enjoyable to discuss science with them, I am particularly indebted to RA for those late hour discussions that enlightened me deeply to understand the computational intricacies, whose outcome is the numerical work presented in this thesis. I thank both of them for the way they led me towards the completion of the thesis. Apart from research, they literally stood as a friend, philosopher and guide in every form of my life, to mention a few, from tea-time debates, grilling-times, playing musical instruments or the support provided in the distressed condition of my health crisis. They were an integral part of my graduate life which I will definitely cherish throughout the rest of my life.

I like to thank all the faculty members of Matscience, who helped my learning process, either as the graduate course instructors or as the doctoral committee members or even as non-sleepy listeners to my presentations. It will be a crime not to pay gratitude to the system administrators, Ravi and Moni, without whose enormous efforts, the computational work would not have come to realm. I also like to thank Mangal for hardware and software management of the parallel clusters with remarkable pace that smoothened out my computational journey. Lastly, I want to thank my seniors, batchmates and juniors for having me inside a friendly discussion of different aspects of science, life and reality! I owe a lot to my batchmates for all those disasters we cooked up together.

At this point, I also like to thank all my teachers from my *good-old* school to the University, whose tremendous and untiring efforts cannot be overlooked, that made me understand the beauty of theoretical science and research as a pathway. Particularly working with Surajit Sengupta as a summer student had set my initial motives for pursuing computational materials research. I want to thank my teachers at CTS of IIT Kharagpur to grow my interest and challenges in theoretical science. I owe a lot to Asim Mukherjee, whose delivery of the clear concepts at the college simplified a lot of my basic understanding of the subject as a puzzled kid.

Lastly, but most importantly, I want to thank my parents for their continuous support. They never intruded to my life, instead encouraged me a lot to pursue what I dream about, listening to my successes and failures with utmost care and friendly discussions. They introduced to me a Hawaiian guitar at a very early age, playing which is still my passion after science.

SYNOPSIS

This thesis addresses problems involving inhomogeneous order parameter configurations at a phase transition between isotropic and nematic phases in liquid crystals. We propose new fluctuating equations of motion and accurate numerical algorithms for this class of problems. We apply our methods to study the nematic-isotropic interface, the dynamics of defects in spinodal decomposition, and the growth of droplets in nucleation.

Nematic liquid crystals, formed in suspensions of sufficiently anisotropic molecules, exhibit orientational order in the absence of translational order. The order parameter of the nematic state, represented as $\mathbf{Q}$, is a tensor quantity, constrained by symmetry and tracelessness. Close to the phase boundary separating isotropic and nematic phases, thermal fluctuations assume importance, leading to enhanced light-scattering, nucleation and the spontaneous generation and diffusion of defects [24].

The formalism of Landau-Ginzburg theory and the simplest time-dependent relaxational equations which represent its dynamics provide a coherent approach to understanding inhomogeneous phenomena in nematic liquid crystals. These time-dependent Ginzburg-Landau (TDGL) equations, however, ignore thermal fluctuations. In this thesis, we promote the TDGL equations to Langevin equations by adding noise terms which preserve the symmetry and tracelessness of the order parameter. This allows us to study the dynamics of large inhomogeneous fluctuations of nematic order within a continuum description.

We then develop efficient numerical methods, based on the method of lines (MOL), for solving both deterministic and stochastic versions of the TDGL equations. These are typically polynomially accurate in the discretization. For highly accurate simulations, which converge exponentially in the discretization, we develop a spectral collocation scheme for obtaining the steady-state solutions of the TDGL equations. The numerical methods are benchmarked by comparing our results with analytical and, when available, previous numerical results. The deterministic and stochastic TDGL equations together with the numerical methods we have developed are then applied to three problems, which we describe in detail below.

Local and spatially varying properties of the isotropic-nematic interface

Elastic deformations of the nematic director are classified into three categories, namely splay, bend and twist deformation associated to the free energy with the Frank elastic constants K_1, K_2 and K_3. However in the tensorial description of the order parameter, this reduces into two elastic constants L_1 and L_2. The one-constant approximation assigns a single elastic constant K for K_1, K_2 and K_3 which results $\kappa(= L_2/L_1)$ to be zero. For any nonzero κ, splay and bending constants are degenerate while twist is small compared to both [32]. However in experiments bending constant is found to be stronger than splay constant [51], which is not accounted in the theory.

The computation of the spatial variation of the nematic order parameter at the isotropic-nematic interface was first posed and solved in a particular limit by de Gennes who introduced a simple uniaxial ansatz for **Q** [23]. In the absence of elastic anisotropy, this ansatz reduces the five degrees of freedom required to describe the local nematic order to one. This simplifying ansatz is known as the "de Gennes ansatz". Popa-Nita *et al.* [57] studied the emergence of biaxiality at the interface, incorporating elastic anisotropy in the limit of planar anchoring, by adapting a parameterization introduced by Sen and Sullivan [64]. However, several *ad hoc* approximations were made for analytical simplification and apart from a few general remarks, the nature of order parameter profiles for an arbitrary oblique anchoring imposed on the director far from the interface boundary was not addressed.

These issues are resolved here by solving the deterministic TDGL equations, retaining *all* the degrees of freedom of the orientational tensor. We show that provided elastic anisotropy is absent that depicts of equal splay, bend and twist constants, the classical de Gennes ansatz is valid, as expected. Once such anisotropy is present, the interface becomes biaxial in nature for any anchoring condition other than homeotropic. We show how the spectral methods we develop for the numerical study of the planar anchoring limit may be generalized to the case in which an oblique anchoring condition is imposed on the director far from the interface. The results indicate that spatial variations of the scalar uniaxial and biaxial order parameters are largely confined to the neighbourhood of the interface, while director orientations interpolate smoothly between the planar or homoeotropic anchoring selected at the interface to the imposed orientation at the boundary.

Defect dynamics and early time diffusive scaling in spinodal kinetics

A broken continuous symmetry phase quenched from high temperatures orders through the annihilation of topological defects. These are singularities of the order parameter field. Defects may be classified according to the underlying homotopy group associated with the order parameter space. The creation and annihilation of these defects is governed by the multiplication rules and commutativity of the elements in the group [49].

We devise a simple way of identifying point defects in a nematics by identifying singular structures from the suppression of the scalar degree of order. While conventional analysis of Schlieren textures based on the rotation of the principal axis are unable to locate all the defects, our methodology locates them precisely. Crucially, the defects can be located without computing topological circuits, reducing the computational expense of a defect-finding algorithm considerably.

We find, consistent with energetic arguments, that half-integer charge defects are stable at late stages of the dynamics while integer charge defects are observed only at the early stage. Point defects in two dimensions correspond to line disclinations in three dimensions, where the combination and annihilation of lines is more complex. We identify line defects in uniaxial and biaxial nematics by generalizing our defect finding algorithm to three dimensions.

We also develop visualization methods for studying the dynamics of topological defects in nematic systems. Using these methods, we find that the dynamics exhibits a clear signature of the intercommutation of defect lines. At late stages, we see the formation of closed loops which finally disappear from the system. There is an ongoing debate concerning the dynamical scaling exponent for phase ordering in uniaxial nematics [12, 14, 77, 25, 26]. By calculating correlation functions and structure factors, we show that dynamical scaling holds, with the correlation length $L(t)$ growing with time as $L(t) \sim t^{\alpha}$ with $\alpha = 0.50 \pm 0.005$, indicating diffusive growth. We find agreement with Porod's law obtained at intermediate and late stages of the dynamics, governed principally by defect-antidefect annihilation processes. We also recover a diffusive growth at the very late stage of dynamics, as conjectured by Goldenfeld *et al.* [77]. In addition, we also study the effects of thermal fluctuations on the defect density.

Breakdown of classical nucleation theory in growth kinetics

A central problem in classical nucleation theory is the calculation of the shape of a nucleating bubble of the ordered phase in the metastable regime. This shape is required to calculate the barrier height, the nucleation rate and the first passage time. Because of the anisotropy of the nematic phase, little is known conclusively about the shape of the nucleating nematic bubble. Early experimental work by Bernal and Fankuchen found evidence for a non-spherical nematic nucleus in a isotropic background [9]. Herring, Chandrasekhar and Virga obtained a non-spherical nucleus making the specific assumption of a homogeneous director field inside the droplet [33, 16, 73]. More recently, Prinsen *et al.* [59] have calculated non-trivial shapes and director fields inside the droplet using a Rapini-Papoular phenomenological surface free energy [61]. Cuetos and Dijkstra use Monte Carlo simulations to obtain a non-spherical droplet with a uniform director field [22].

Our methods can access these properties without any approximation. The surface free energy is accounted for automatically in our formulation. We show that in the presence of elastic anisotropy, an initially spherical uniaxial nematic nucleus immersed in an isotropic background changes shape to an ellipsoid, with the long axis oriented depending on the sign of the elastic anisotropy κ. $\kappa > 0$ results to a large bending constant compared to twist constant while $\kappa < 0$ leads to a larger twist constant. However, splay and bend constants remain degenerate.

In two dimension and in the presence of thermal fluctuations, two regimes are observed, depending on the sign of the elastic anisotropy. For positive anisotropy, integer charged defects develop inside the nematic bubble with ellipsoidal shapes deviating sufficiently from circularity. The defects observed in the case of positive anisotropy remain even at late stages of the dynamics, by which time bubbles have coalesced completely and the nematic phase fluctuates in equilibrium.

For negative anisotropic contribution, a uniform director field emerges but the bubbles are observed to be ellipsoidal. Without the anisotropic elastic term, circular nematic bubbles nucleate with uniform director configuration. Classical nucleation theory, which assumes a uniform order parameter configuration is thus inapplicable in the case of both positive and negative elastic anisotropy since the order parameter configurations can be non-uniform and the droplet shape is far from being spherical.

LIST OF PUBLICATIONS

- A.K. Bhattacharjee, Gautam I. Menon and R. Adhikari. 2008.
  Numerical method of lines for the relaxational dynamics of nematic liquid crystals,
  Phys. Rev. E **78**, 026707.

- S.M. Kamil, A.K. Bhattacharjee, R. Adhikari and Gautam I. Menon. 2009.
  Biaxiality at the isotropic - nematic interface with planar anchoring,
  Phys. Rev. E **80**, 041705.

- S.M. Kamil, A.K. Bhattacharjee, R. Adhikari and Gautam I. Menon. 2009.
  The isotropic-nematic interface with an oblique anchoring condition,
  J. Chem. Phys. **131**, 174701.

- A.K. Bhattacharjee, Gautam I. Menon and R. Adhikari. 2010.
  Fluctuating dynamics of nematic liquid crystals using the stochastic method of lines,
  J. Chem. Phys. **133**, 044112.

Contents

Acknowledgements **ii**

Synopsis **iii**

List of Publications **vi**

1 Introduction **1**

1.1 Liquid crystalline Mesophases 1
1.2 Nematic liquid crystals 3
1.3 Definition of the order parameter 4
1.4 Mean field description : Statics 6
1.4.1 Phase diagram 9
1.5 Kinetics at zero temperature 10
1.6 Organization of the thesis 11

2 Order parameter fluctuation in nematic liquid crystal **13**

2.1 Introduction 13
2.2 Fluctuating kinetics of the order parameter 14
2.3 Static and dynamic correlations 16
2.3.1 Correlations in the linear theory 16
2.3.2 Correlations in the nonlinear theory 17
2.4 Conclusion 17

3 Numerical method for order parameter dynamics **19**

3.1 Introduction 19
3.2 Non-dimensionalization of the parameters 20
3.3 Method of lines 21
3.4 Spectral collocation technique 22
3.4.1 Benchmark of Allen-Cahn equation 23
3.5 Stochastic method of lines 24
3.5.1 Benchmark of Ornstein-Uhlenbeck process 24
3.5.2 Discretization of fluctuating nematodynamics 25
3.5.3 Correlations in the linear theory 26
3.5.4 Correlations in the nonlinear theory 28

3.6 High performance computation 29
  3.6.1 Benchmark of Allen-Cahn equation 30
3.7 Visualization of order parameter fields 31
  3.7.1 Scalar field in Allen-Cahn equation 31
  3.7.2 Tensor field in nematics 32
3.8 Conclusion 33

4 Local and nonlocal properties of the isotropic-nematic interface 35
4.1 Introduction 35
4.2 Verification of de Gennes ansatz 39
4.3 Isotropic-nematic interface with planar anchoring 40
  4.3.1 Benchmarking the spectral collocation technique 41
  4.3.2 Local biaxiality at the interface 41
4.4 The isotropic-nematic interface with oblique anchoring 43
  4.4.1 Non-locality of the tilt angle with $\kappa > 0$ 46
  4.4.2 Non-locality of the tilt angle with $\kappa < 0$ 47
4.5 Fluctuation of the I-N interface 47
4.6 Conclusion 48

5 Diffusive scaling and defect morphology in the spinodal kinetics of nematics 51
5.1 Introduction 52
5.2 Phase ordering in uniaxial nematics 56
  5.2.1 Point defects : core structure and dynamics 56
  5.2.2 Dynamical scaling in two dimensions 57
  5.2.3 Intercommutation, loop formation of line defects in three dimensions 60
5.3 Fluctuating defect kinetics 61
5.4 Phase ordering in biaxial nematics 62
  5.4.1 Point defects : core structure and dynamics 62
  5.4.2 Dynamical scaling in two dimensions: separation of time scale 64
  5.4.3 Visualization of line defects commutation in three dimensions 66
5.5 Conclusion 69

6 Breakdown of classical nucleation theory in nucleation kinetics 71
6.1 Introduction 71
6.2 Structure of nucleated nematic droplets in two dimensions 73
  6.2.1 Circular droplets with uniform director at $\kappa = 0$ 74
  6.2.2 Complex droplet geometry with integer defect at $\kappa > 0$ 74
  6.2.3 Ellipsoidal droplets with uniform director at $\kappa < 0$ 78
6.3 Structure of nucleated nematic droplets in three dimensions 80
  6.3.1 Spherical droplets with $\kappa = 0$ 80
  6.3.2 Ellipsoidal droplets with $\kappa > 0$ 82
  6.3.3 Ellipsoidal droplets with $\kappa < 0$ 82
6.4 Conclusion 86

7 Conclusions 89

A Nematodynamic equations 93

B Equation for the isotropic-nematic interface 97

C Index of animations 99

Bibliography 103

List of Figures

1.1 Experimental realization of Kibble mechanism 2
1.2 Schlieren textures in Optical microscopy 2
1.3 Schematic representation of isotropic and nematic phase 3
1.4 Free energy diagram 8
1.5 Phase diagram 10

3.1 Interface in Allen-Cahn equation 23
3.2 Autocorrelation function for the Ornstein-Uhlenbeck process 25
3.3 Orientational distribution 26
3.4 Structure factor in linear theory 27
3.5 Autocorrelation of Langevin Equation 28
3.6 Structure factor in nonlinear theory 29
3.7 Isosurfaces of the scalar field 31
3.8 Visualization of tensor field 32

4.1 I-N interface geometry 37
4.2 Diagram verifying de Gennes ansatz 40
4.3 Spectral convergence in I-N interface 41
4.4 Uniaxial and biaxial order with planar anchoring 42
4.5 Uniaxial-biaxial degrees and local tilt with oblique anchoring 45
4.6 Uniaxial-biaxial degrees and local tilt with oblique anchoring 47
4.7 Interface with thermal fluctuation 48

5.1 Uniaxial and biaxial order and textures in uniaxial nematic crystal 55
5.2 Defect core structure in uniaxial phase 56
5.3 Dynamical scaling of the direct correlator in the uniaxial phase 57
5.4 Data collapse of the structure factor in the uniaxial phase 58
5.5 Defect strings in uniaxial phase 59
5.6 Inter-commutation of defect strings 60
5.7 Dynamical scaling of the structure function of the uniaxial phase in 3D 61
5.8 Effect of thermal fluctuations on density of point defects 62
5.9 Point defects and texture in biaxial phase 63
5.10 Biaxial defect core structure 64
5.11 Dynamical scaling in the biaxial phase in 2D 65

5.12 Dynamical scaling in biaxial quench 65
5.13 Defect strings in biaxial phase 67
5.14 Intercommutation of biaxial defect strings 68
5.15 Dynamical scaling of the structure function of the uniaxial phase in 3D 68

6.1 Circular drops with $\kappa = 0$ 75
6.2 Shape of nematic drops at zero temperature with $\kappa = 0$ 76
6.3 Ellipse-shaped drops with $\kappa > 0$ 77
6.4 Shape of nematic drops at zero temperature with $\kappa > 0$ 78
6.5 Nucleating ellipse-shaped drops at $\kappa < 0$ 79
6.6 Shape of nematic drops at zero temperature with $\kappa < 0$ 80
6.7 Spherical droplets in 3-dimensions with $\kappa = 0$ 81
6.8 Cross-section and field structure of nucleating drops 82
6.9 3D structures of uniaxial droplets with $\kappa > 0$ 83
6.10 Field structure and cross-section of a droplet with $\kappa > 0$ 84
6.11 Nucleating drops with $\kappa < 0$ 85
6.12 Droplet Cross-section and field structure with $\kappa < 0$ 86

List of Tables

3.1 Non-dimensionalization of parameters in the GLdG theory 20
3.2 Scaling of the parallel algorithm 30

4.1 Numerical parameters in the interface studies 39

5.1 Numerical parameters in the spinodal kinetics studies 54

6.1 Numerical parameters in the nucleation kinetics studies 73

Chapter 1

Introduction

We begin with a brief survey of different liquid crystalline phases. The nematic phase and its order parameter are then described. A brief introduction to methodologies for studying statics and dynamics within the coarse-grained Ginzburg-Landau-de Gennes description of nematic liquid crystals is provided. We conclude with an outline of the thesis and its central results.

1.1 Liquid crystalline Mesophases

Soft materials have a mechanical response which differs substantially from that of typical crystalline solids at the same pressure and temperature. For example, typical shear elastic constants in soft materials are of order 10 Pa, while for hard materials such as iron or copper, these constants can be of order 10^{11} Pa ($1Pa = 1\ N/m^2$). This implies that order in such soft materials is easily affected by thermal fluctuations as well as by applied forces of moderate strength. Response in such materials is often complex and non-linear, leading to a whole range of exotic non-equilibrium phenomena.

Examples of soft matter include a large number of materials encountered in everyday life, such as liquids, polymers, colloids, gels, foams and living cells. Of these many examples, a class of soft materials which exhibits properties characteristic of both solids and liquids in thermal equilibrium simultaneously is of special interest. Such phases are commonly known as “mesophases”, since their properties are intermediate between two commonly encountered extremes. Liquid crystalline materials display a great variety of such mesophases, exhibiting order intermediate between the perfect rotational and translational order of the crystal and the disorder characteristic of the isotropic fluid.

Such *mesophases* are broadly classified into two classes: disordered crystal mesophases and ordered fluid mesophases. Disordered crystal mesophases retain a crystal lattice structure, while the (in general, anisotropic) molecules lack a common orientation. Such phases are usually known as “plastic crystals”. Ordered fluid mesophases exhibit orientational order in the absence of full translational order. Such phases are commonly known as “liquid crystals”. They are found in systems of elongated molecules.

Liquid crystals can be “thermotropic” or “lyotropic”. In thermotropic liquid crystals, transitions between different phases can be driven by a change in temperature. Thus, they play an important role in a variety of technological applications *e.g.* in temperature sensors, electro-optic displays etc. Common examples are N-(p-methoxybenzylidene)-p'-n-butylaniline (MBBA) and cholesteryl nanonate.

Transitions in lyotropic liquid crystalline mesophases can be driven by varying the solvent concentration, thus changing the density. Examples of molecules forming such phases are the long rod-shaped tobacco mosaic virus (TMV) and the polymer deoxyribo-nucleic acid (DNA).

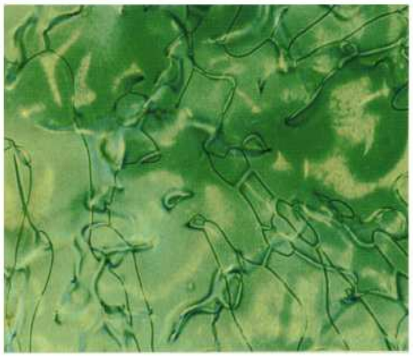

Figure 1.1: Topological defect entanglement in a nematic liquid crystal film of width 790μm after a temperature quench, showing monopoles, boojums and various integer and half-integer defects. Picture from Turok *et al.* [21].

Both thermotropic and lyotropic liquid crystals behave like fluids in that they cannot sustain shear. However, in contrast to ordinary fluids, they can transmit torques, due to the fact that molecules in liquid crystalline states are orientationally ordered. Their solid-like properties originate from the fact that they have an optic axis. They thus exhibit birefringence, as in anisotropic crystals. This anisotropy is also reflected in a large number of measured properties, including the electric and magnetic susceptibilities.

Molecules which form nematic mesophases are typically optically inactive. Chiral molecules, on the other hand, can form *cholesteric* phases where such chirality is manifest. In the cholesteric phase, the direction of average molecular alignment order rotates in a helical manner about a common axis, with the pitch of the helix often being of order a few thousand angstroms.

Phases with partial order in the positions of the molecules are generically classified as *smectic*. Smectics are divided into three broad classes, A,B and C. The smectic-A phase is composed of molecules aligned parallel to each other in an arrangement of periodically stacked layers. There is no translational order in each layer. While each layer thus behaves as a fluid, the periodicity in the layering is a property of a solid, rather than a liquid. The Smectic-C phase differs from the Smectic-A in that individual molecules are tilted away from the layer normal. In the Smectic-B phase, the individual layers have 6-fold

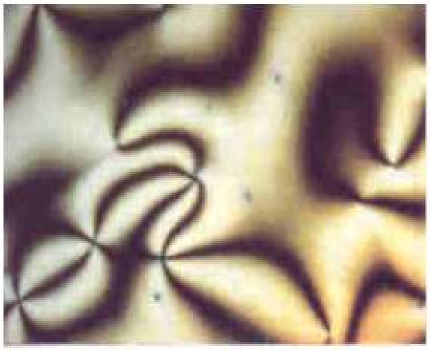

Figure 1.2: The schlieren textures with two and four brushes exhibited by a uniaxial nematic film at 114.8° centigrade. Picture from Chandrasekhar *et al.* [17].

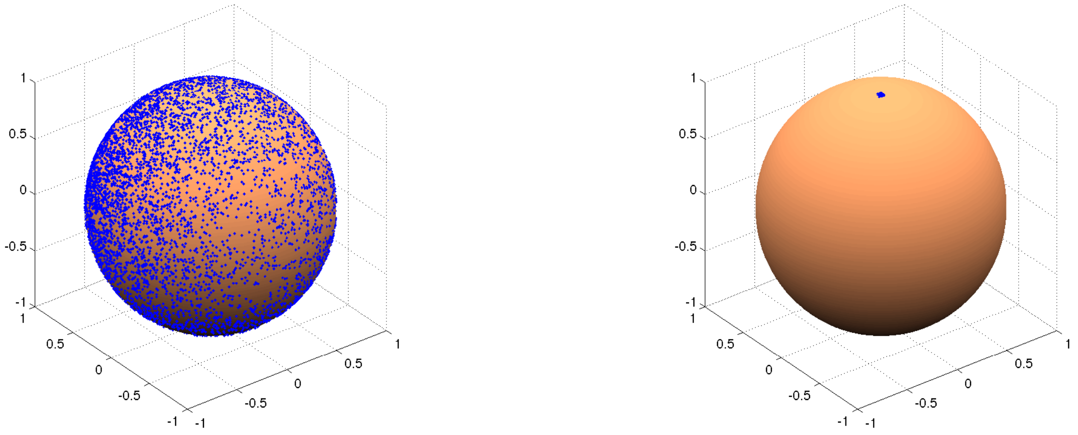

(a) Isotropic phase

(b) Nematic phase

Figure 1.3: (a) shows a unit sphere with an uniform director distribution at the isotropic phase and (b) shows the uniaxial nematic phase with concentric director distribution. Frame (a) is generated in a numerical solution of the GLdG equation for nematics, discussed in the subsequent section, in the isotropic phase, with the numerical parameters $A = 0.05, L_1 = 10A, B = C = E' = L_2 = 0$ on a 16^2 lattice system, while frame (b) is generated with the parameters, $A = -3.5, B = -0.5, C = 2.67, L_1 = 32, L_2 = E' = 0$ on a 64^2 lattice system.

bond-orientational order Many more such remarkable mesophases have been identified and classified. A detailed summary can be found in Ref. [38].

1.2 Nematic liquid crystals

This thesis studies properties of nematic mesophases, of which two examples from experiment are shown in Fig.(1.1-1.2). To define order in liquid crystalline phases, it is necessary to identify how such phases differ from isotropic liquid phases. The symmetry of the isotropic liquid phase is described through the group $\mathcal{T}(3) \times \mathcal{O}(3)$ [38]. These groups describe translational and rotational symmetry of the molecules in three Cartesian directions and around three independent axes. Individual molecules exhibit an uniform angular distribution, as shown in Fig.[1.3(a)] where the orientation of individual molecules is denoted by points on the surface of a unit sphere.

The nematic phase breaks the $\mathcal{O}(3)$ rotational symmetry, selecting an arbitrary direction for the molecules to orient in parallel. This differs significantly from other systems (*e.g.* ferromagnetic spin systems) that also break rotational symmetry by aligning in a particular direction. Nematic liquid crystals consisting of polar or apolar molecules, need not show ferro-electricity in response to an external field. This indicates that opposite directions of orientation of the nematic molecules are equivalent. The symmetry point group of the nematic phase is denoted as $\mathcal{T}(3)\times\mathbb{D}_{\infty h}$ in the Schoenflies notation [38]. If only one direction of orientation of the molecules exists, defining a single optic axis, then the phase is called the *uniaxial nematic*.

Fig.[1.3(b)] shows the distribution of local orientations plotted on the unit sphere. The angular distribution peaks at the poles, with the location of the peak defining the average direction of orientation of the molecules. If there is a peak at θ, there must be an equivalent peak at $\pi-\theta$, reflecting the uniaxiality of the phase. The same symmetry group also applied to a phase called *discotic* where the molecules orient themselves to an axis perpendicular to their long axis. The other phase exhibited by such molecules is the *biaxial nematic* phase, where the additional axes of the molecule, apart from the axis defining uniaxial ordering, may also order, leading to two different optical axes overall. The symmetry group of this phase is thus designated as $\mathcal{T}(3)\times\mathbb{D}_{2h}$ [38].

1.3 Definition of the order parameter

The nematic phase is characterized by a broken rotational symmetry in the presence of translational symmetry. A scalar order parameter (such as the density characterizing a liquid-gas transition) or a vector order parameter (such as the magnetization characterizing the paramagnetic to ferromagnetic transition in spin systems), are insufficient to quantify order in the nematic phase. As macroscopic response functions of the bulk material, such as electronic polarizability, refractive index or diamagnetic susceptibility, are tensorial and anisotropic in nature, orientational order in the nematic phase can be quantified in the same spirit through a second-rank, symmetric traceless tensor, $Q_{\alpha\beta}$ [24]. The tracelessness imposes the condition that material response is isotropic in the orientationally and translationally disordered fluid phase.

The principal axes of this tensor, obtained by diagonalizing $\mathbf{Q}$, specify the direction of nematic ordering. The principal values represent the strength of nematic ordering.

Locally, nematic order is defined through

$$\mathbf{Q}(\mathbf{x},t)=\int du f(\mathbf{x},\mathbf{u},t)\,\overline{\mathbf{uu}}\equiv\langle\overline{\mathbf{uu}}\rangle \tag{1.1}$$

where $f(\mathbf{x},\mathbf{u},t)$ is the molecular orientational distribution function at the position $\mathbf{x}$ at time t which counts the number of molecules with long axis oriented in the direction $\mathbf{u}$, $\overline{X}$ defines the symmetric traceless part of an arbitrary real second rank tensor $\mathbf{X}$ with

$$\overline{X}=\frac{1}{2}\left(X+X^T\right)-\frac{1}{d}\mathrm{Tr}(X)\mathcal{I}, \tag{1.2}$$

where X^T denotes the transpose of the tensor i.e. $(X^T)_{\alpha\beta}=X_{\beta\alpha}$, d denotes the dimension and $\mathcal{I}$ is the identity matrix. The average is defined as $<\cdot>\equiv\int du f(\mathbf{x},\mathbf{u},t)(\cdot)$.

We can separate the variables of the distribution function by going to principal axes. The three principal axes specify the director $\mathbf{n}$, the codirector $\mathbf{l}$ and the joint normal to these, $\mathbf{m}$. Since the spherical harmonics form a complete basis of orthonormal functions, the orientational distributional function can be expanded as,

$$f(\mathbf{x},\mathbf{u},t)=\sum_{i=0}^{\infty}g_i(\mathbf{x},t)Y^i(\mathbf{u}), \tag{1.3}$$

where $g_i(\mathbf{x},t)$ are the expansion coefficients and $Y^i(\mathbf{u})$ are the spherical harmonics. We can expand $Y^i(\mathbf{u})$ in multiple moments, which yields the form of the distribution function as,

$$f(\mathbf{x},\mathbf{u},t)\approx\frac{1}{4\pi}[1+\mathbf{u}\cdot\mathbf{p}(\mathbf{x},t)+(u_\alpha u_\beta-\frac{1}{3}\delta_{\alpha\beta})Q_{\alpha\beta}(\mathbf{x},t)+\cdots]. \tag{1.4}$$

where,

$$\begin{align} 1 &= \int du f(\mathbf{x},\mathbf{u},t), \tag{1.5}\\ \mathbf{p}(\mathbf{x},t) &= \int du\mathbf{u}f(\mathbf{x},\mathbf{u},t), \tag{1.6}\\ \mathbf{Q}(\mathbf{x},t) &= \int du\,\overline{\mathbf{u}\mathbf{u}}\,f(\mathbf{x},\mathbf{u},t). \tag{1.7}\end{align}$$

Eq.(1.5) is the normalization, Eq.(1.6) is the polarization and Eq.(1.7) is the nematic order of the system. As a conventional nematic phase is non-polar, we may take $\mathbf{p}=0$ and the first nontrivial contribution to the orientational order comes from the second moment of the expansion. Note that $g_i(\mathbf{x},t)$ also contains information about the density $\rho(\mathbf{x},t)$ of the phase. For simplicity, we assume that $\rho(\mathbf{x},t)$ is uniform throughout the system.

Given the two principal values S and T, the order parameter can be written as

$$Q_{\alpha\beta}=\frac{3}{2}S(n_\alpha n_\beta-\frac{1}{3}\delta_{\alpha\beta})+\frac{T}{2}(l_\alpha l_\beta-m_\alpha m_\beta), \tag{1.8}$$

where $\alpha,\beta\equiv x,y,z$ denote the Cartesian directions in the local frame and,

$$\begin{align} S &= \langle P_2(\cos\theta)\rangle=\langle(\cos^2\theta-\frac{1}{3})\rangle, \tag{1.9}\\ T &= \langle\sin^2\theta\cos 2\phi\rangle, \tag{1.10}\end{align}$$

are measures of uniaxial and biaxial alignment. The S and T are proportional to the spherical harmonics Y_{20} and Y_{22} respectively. These are bounded as $-\frac{1}{3}\leq S\leq\frac{2}{3}$, $0\leq T<3S$. $S=\frac{2}{3}$ correspond to the nematic phase, whereas $S=0$ correspond to the isotropic phase. The (polar) angle between $\mathbf{n}$ and $\mathbf{u}$ is θ, while the (azimuthal) angle between $\mathbf{l}$ and $\mathbf{u}$ is ϕ with the bound, $-1\leq cos\theta\leq 1$ and $0\leq\phi<2\pi$ respectively. Y_{uv} are the spherical harmonics defined as

$$Y_{uv}(\theta,\phi)=\sqrt{\frac{2u+1}{4\pi}\frac{(u-v)!}{(u+v)!}}P_u^v(cos\theta)\exp(iv\phi), \tag{1.11}$$

where $P_u^v(cos\theta)$ are the associated Legendre polynomials, which forms a complete set of orthogonal functions in the index u for each v on the specified interval [1].

The tensor $\mathbf{Q}$ is diagonal in a coordinate system aligned with the principal axes with the form,

$$\mathbf{Q} = \begin{pmatrix} -(S+T)/2 & 0 & 0 \\ 0 & -(S-T)/2 & 0 \\ 0 & 0 & S \end{pmatrix}. \tag{1.12}$$

The order parameter defined in this manner distinguishes different phases that either preserve or break the rotational symmetry. For example, in the nematic phase corresponding to the $\mathbb{D}_{\infty h}$ group, there are three values of T which lead to two degenerate eigenvalues of the matrix (1.12), namely $T = 0, \pm 3S$. The last two represent the discotic phase. In the uniaxial nematic phase, $T = 0$ and the tensor (1.8) takes the form $\mathbf{Q} = (3/2)S\overline{\mathbf{nn}}$. On the other hand, in the biaxial phase corresponding to the $\mathbb{D}_{2h}$ group, $T \neq 0$ and $\mathbf{Q}$ is represented by Eq.(1.8). In an isotropic phase, all three eigenvalues are equal and the principal directions are equivalent, hence $S = T = 0$.

A chosen coordinate system that diagonalizes the $\mathbf{Q}$ matrix at a given point in space does not automatically diagonalize the same matrix at other points in space. In a frame of reference which is not aligned with the principal axes, we can expand the orientational tensor in a basis of symmetric traceless matrices $T^i_{\alpha\beta}$ [30, 66] as

$$Q_{\alpha\beta}(\mathbf{x}, t) = \sum_{i=1}^{5} a_i(\mathbf{x}, t) T^i_{\alpha\beta}, \tag{1.13}$$

where, $\mathbf{T}^1 = \sqrt{\frac{3}{2}}\,\overline{\hat{\mathbf{z}}\hat{\mathbf{z}}}$, $\mathbf{T}^2 = \sqrt{\frac{1}{2}}(\hat{\mathbf{x}}\,\hat{\mathbf{x}} - \hat{\mathbf{y}}\,\hat{\mathbf{y}})$, $\mathbf{T}^3 = \sqrt{2}\,\overline{\hat{\mathbf{x}}\,\hat{\mathbf{y}}}$, $\mathbf{T}^4 = \sqrt{2}\,\overline{\hat{\mathbf{x}}\,\hat{\mathbf{z}}}$ and $\mathbf{T}^5 = \sqrt{2}\,\overline{\hat{\mathbf{y}}\,\hat{\mathbf{z}}}$ respectively. The complete basis of matrices is orthogonal in the sense that $T^i_{\alpha\beta}T^j_{\alpha\beta} = \delta_{ij}$. In this basis, $\mathbf{Q}$ takes the form

$$\mathbf{Q} = \frac{1}{\sqrt{2}} \begin{pmatrix} -\frac{a_1}{\sqrt{3}} + a_2 & a_3 & a_4 \\ a_3 & -\frac{a_1}{\sqrt{3}} - a_2 & a_5 \\ a_4 & a_5 & \frac{2a_1}{\sqrt{3}} \end{pmatrix}. \tag{1.14}$$

The usefulness of this expansion will be apparent in subsequent chapters of this thesis.

1.4 Mean field description : Statics

The Ginzburg-Landau-de Gennes (GLdG) phenomenological free energy functional $\mathcal{F}$ [23] describing the isotropic-nematic transition is obtained from a local expansion in powers of $\mathcal{O}(3)$ rotationally invariant combinations of the order parameter,

$$\mathcal{F}_h[\mathbf{Q}] = \frac{1}{2}A\mathrm{Tr}\mathbf{Q}^2 + \frac{1}{3}B\mathrm{Tr}\mathbf{Q}^3 + \frac{1}{4}C(\mathrm{Tr}\mathbf{Q}^2)^2 + E'(\mathrm{Tr}\mathbf{Q}^3)^2, \tag{1.15}$$

where we consider terms upto sixth order in the order parameter. We do not include some additional terms allowed by symmetry in the spirit of simplifying the model[1]. Here $A =$

---

[1] In the absence of external force fields (e.g. gravity, electric field etc), the linear term in the free energy expansion automatically drops out accounting to the traceless property of $\mathbf{Q}$.

$A_0(1-T/T^*)$, where T^* denotes the supercooling transition temperature. From the inequality

$$(\mathrm{Tr}\mathbf{Q}^2)^3/6 \geq (\mathrm{Tr}\mathbf{Q}^3)^2, \tag{1.16}$$

higher powers of $\mathrm{Tr}\mathbf{Q}^3$ can be excluded for the simplest description of the uniaxial phase. The uniaxial phase is described by $E' = 0$ whereas $E' \neq 0$ describes the biaxial phase. For nematic rod-like molecules $B < 0$, whereas for disc-like molecules $B > 0$. The quantities C and E' are always taken to be positive to ensure stability and boundedness of the free energy in both the isotropic and nematic phases.

To the local free energy, non-local terms arising from rotationally invariant combinations in the lowest order in gradients of the order parameter must be added which account for low energy long range distortions [23],

$$\mathcal{F}_{el}[\partial\mathbf{Q}] = \frac{1}{2}L_1(\partial_\alpha Q_{\beta\gamma})(\partial_\alpha Q_{\beta\gamma}) + \frac{1}{2}L_2(\partial_\alpha Q_{\alpha\beta})(\partial_\gamma Q_{\beta\gamma}), \tag{1.17}$$

where the indices α, β, γ denote the three Cartesian directions in the local frame, L_1 and L_2 are the elastic constants with L_1 corresponding to the isotropic elastic contribution and L_2 to the anisotropic elasticity. According to Einstein's summation convention, repeated indices are summed over. Surface terms of the same order in gradients may also be added, but we omit them in the work presented in this thesis, with an assumption that contributions from the surface can be neglected in the problems we study.

Unlike $O(n)$ spin systems, in nematic liquid crystals, space and spin coordinates are not decoupled. In a description of the elasticity of the nematic phase due to Ericksen and Leslie, which works with the *director* field $\mathbf{n}$, the scalar order parameter variation is neglected and three broad classes of elastic distortions, namely *splay*, *bend* and *twist* result,

$$\mathcal{F}_{el}[\partial\mathbf{n}] = \frac{1}{2}K_1(\nabla\cdot\mathbf{n})^2 + \frac{1}{2}K_2(\mathbf{n}\cdot\nabla\times\mathbf{n})^2 + \frac{1}{2}K_3(\mathbf{n}\times\nabla\times\mathbf{n})^2. \tag{1.18}$$

The relationship between L_1, L_2 and the Frank constants K_1, K_2 and K_3 is the following [24, 32],

$$K_1 = K_3 = \frac{9}{4}(2L_1 + L_2)S^2, K_2 = \frac{9}{2}L_1S^2. \tag{1.19}$$

The vectors $\mathbf{n}, \mathbf{l}$ and $\mathbf{m}$ represent the broken symmetries of the system and small fluctuations of these from the average alignment will be hydrodynamic modes. The amplitude S and T are non-hydrodynamic, contributing to the local part of the free energy.

The total free energy of the phase including local and gradient terms is given as,

$$\begin{aligned} F \;=\; & \int d^3\mathbf{x}[\frac{1}{2}A\mathrm{Tr}\mathbf{Q}^2 + \frac{1}{3}B\mathrm{Tr}\mathbf{Q}^3 + \frac{1}{4}C(\mathrm{Tr}\mathbf{Q}^2)^2 + E'(\mathrm{Tr}\mathbf{Q}^3)^2 + \\ & \frac{1}{2}L_1(\partial_\alpha Q_{\beta\gamma})(\partial_\alpha Q_{\beta\gamma}) + \frac{1}{2}L_2(\partial_\alpha Q_{\alpha\beta})(\partial_\gamma Q_{\beta\gamma})]. \end{aligned} \tag{1.20}$$

In Fig.(1.4) we show the local part of the free energy and the corresponding stable phases. The presence of the cubic term is manifest in the asymmetric double well shape of the free

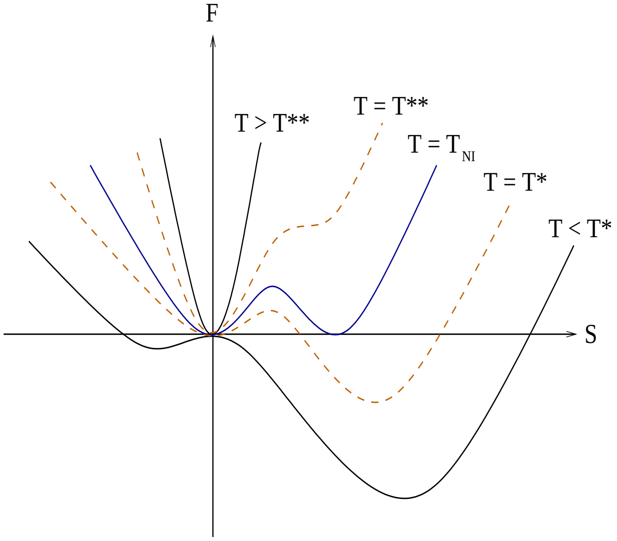

Figure 1.4: The variation of the local free energy with the degree of uniaxiality in the nematic phase.

energy which in turn is responsible for the first order nature of the phase transition. Setting $A = 0$ in Eq.(1.15) yields the supercooling spinodal line. The superheating spinodal line is obtained through the condition that the ordered phase becomes absolutely unstable. The isotropic phase is absolutely stable for temperatures above the superheating temperature T^{**}. For temperatures between $T_{NI} < T < T^{**}$, the isotropic phase is stable and the nematic phase is metastable. For temperatures in the range $T^* < T < T_{NI}$, with T^* being the supercooling temperature, the isotropic phase is metastable and the nematic phase is stable. For temperatures below T^*, the only stable state is the nematic phase. Positive S corresponds to the uniaxial nematic phase while negative S corresponds to the discotic phase.

The inequality presented in Eq.(1.16) can be represented in a coordinate independent form with two parameters q and ω, which are the normalized measure of the uniaxiality and biaxiality, defined through the relation

$$q^2 = \mathrm{Tr}\mathbf{Q}^2 = \frac{1}{2}(3S^2 + T^2), \tag{1.21}$$

$$q^3(1-\omega) = \sqrt{6}\mathrm{Tr}\mathbf{Q}^3 = \sqrt{\frac{27}{8}}(S^3 - ST^2) \tag{1.22}$$

with ω is bounded between $[0, 1]$. The condition $\omega = 0$ corresponds to the fully uniaxial phase and $\omega > 1$ corresponds to the biaxial phase with the upper bound $\omega = 1$, corresponding to a fully biaxial phase [4].

Elimination of q from the above two equations results in the following form of ω,

$$\omega = 1 \pm \frac{\sqrt{27}(ST^2 - S^3)}{(3S^2 + T^2)^{3/2}}. \tag{1.23}$$

The ± sign is chosen so as to satisfy the inequality $ST^2 \geq S^3$ while retaining the bound on ω.

1.4.1 Phase diagram

A phase diagram that locates isotropic, uniaxial nematic, biaxial nematic and discotic phases in terms of the parameters of the local free energy defined in Eq.(1.15) can be calculated given the form of the Landau-Ginzburg-de Gennes free energy functional. (We correct minor errors in the calculations of the phase boundaries reported in Ref. [32].) With the form of the order parameter defined in Eq.(1.12), the homogeneous part of the free energy can be rewritten as,

$$\mathcal{F}_h[\mathbf{Q}] = \alpha(S) + T^2\beta(S) + \frac{1}{2}T^4\gamma(S) \tag{1.24}$$

where

$$\begin{aligned} \alpha(S) &= \frac{3}{4}AS^2 + \frac{1}{4}BS^3 + \frac{9}{16}CS^4 + \frac{9}{16}E'S^6, & (1.25)\\ \beta(S) &= \frac{1}{4}A - \frac{1}{4}BS + \frac{3}{8}CS^2 + \frac{9}{8}E'S^4, & (1.26)\\ \gamma(S) &= \frac{1}{8}C + \frac{9}{8}E'S^2. & (1.27) \end{aligned}$$

The minimization condition $\delta\mathcal{F}_h/\delta T = 0$ results in the uniaxial phase $T = 0$ and the biaxial phase $T = \pm\sqrt{-\beta(S)/\gamma(S)}$. As C and E' are always positive to ensure boundedness of the free energy, $\gamma(S) > 0$ and $\beta(S) < 0$. The uniaxial and biaxial free energies are,

$$\begin{aligned} \mathcal{F}_U(S) &= \alpha(S), & (1.28)\\ \mathcal{F}_B(S) &= \alpha(S) - \frac{\beta(S)^2}{2\gamma(S)}. & (1.29) \end{aligned}$$

The first order isotropic to uniaxial nematic transition at the critical value $S = S_c$ is obtained through the conditions $\mathcal{F}_U(S_c) = \mathcal{F}'_U(S_c) = 0$ and $\mathcal{F}''_U(S_c) > 0$. This then imposes the conditions

$$\begin{aligned} A &= \frac{3}{4}CS_c^2 + \frac{9}{4}E'S_c^4, & (1.30)\\ B &= -\frac{9}{2}CS_c - 9E'S_c^3. & (1.31) \end{aligned}$$

The second order uniaxial to biaxial transition at the critical value $S = S'_c$ is obtained through the conditions $\mathcal{F}''_U(S_c) = \mathcal{F}''_B(S_c) = 0$ and $\mathcal{F}_U(S_c) = \mathcal{F}_B(S_c)$. Hence,

$$\begin{aligned} A &= -\frac{9}{2}CS_c'^2, & (1.32)\\ B &= -\frac{45}{4}E'S_c'^3. & (1.33) \end{aligned}$$

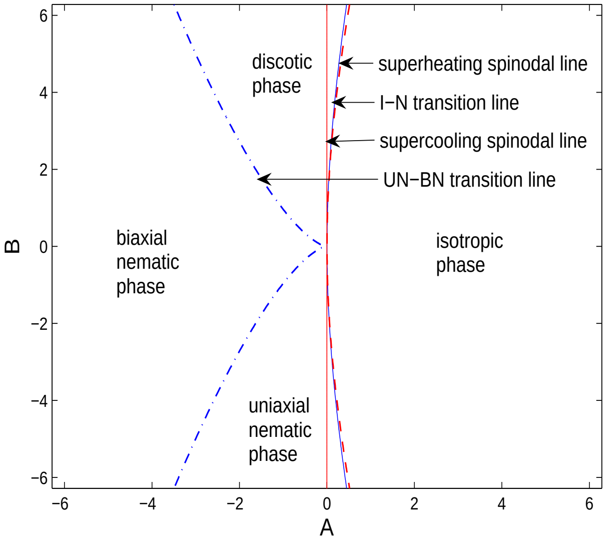

Figure 1.5: The mean field phase diagram obtained from the Landau-de Gennes free energy (1.15). The phase boundaries are given by solutions of the following algebraic equations : $4B^4E+B^2C(3C^2-144AE') = A(81C^4-864AC^2E'+2304A^2E'^2)$ for the isotropic to uniaxial nematic transition; $25A^3E'^2 = -18B^2C^3$ for the uniaxial to biaxial nematic transition; $A = 0$ for the supercooling spinodal; $9B^4E' + 8B^2(C^3 - 36ACE') = 192A(C^2 - 4AE')^2$ for the superheating spinodal.

The phase diagram is shown in Fig.(1.5). In the diagram, there are lines separating the nematic phase with $S > 0$ from the discotic phase, in addition to the isotropic to nematic transition lines. There are also two uniaxial to biaxial nematic second order lines in addition to the two first order isotropic-uniaxial nematic lines. One of these transition lines marks the transition to the nematic phase with $S > 0$ and the other for the discotic phase with $S < 0$. The four phases meet at the bicritical Landau point $A = B = 0$. At the bicritical point, the isotropic to nematic transition is second order rather than first order.

1.5 Kinetics at zero temperature

Once perturbed from the stable state, the order is restored in the system through different routes. In the absence of flow, mean-field theory assigns the order parameter a value which minimizes the free energy. Neglecting hydrodynamics, the governing dynamics for the non-conserved order parameter can be taken to be overdamped and relaxational in nature, following from

$$\partial_t Q_{\alpha\beta} = -\Gamma_{\alpha\beta\mu\nu}\frac{\delta F}{\delta Q_{\mu\nu}}, \tag{1.34}$$

with

$$\Gamma_{\alpha\beta\mu\nu} = \Gamma[\delta_{\alpha\mu}\delta_{\beta\nu} + \delta_{\alpha\nu}\delta_{\beta\mu} - \frac{2}{3}\delta_{\alpha\beta}\delta_{\mu\nu}]. \tag{1.35}$$

Here the choice of the matrix of kinetic coefficients $\Gamma_{\alpha\beta\mu\nu}$, a fourth rank symmetric, traceless tensor, ensures that the dynamics preserve the symmetry and traceless property of the order parameter. In the absence of long-range forces, a local approximation for the kinetic coefficients is adequate, and Γ can be taken as a constant[2].

Using the LGdG free energy, the equation of motion of the order parameter takes the form

$$\begin{aligned} \partial_t Q_{\alpha\beta}(\mathbf{x},t) &= -\Gamma\ [(A + C\mathrm{Tr}Q^2)Q_{\alpha\beta}(\mathbf{x},t) + (B + 6E'\mathrm{Tr}Q^3)\,\overline{Q^2_{\alpha\beta}(\mathbf{x},t)} \\ &\quad -L_1\nabla^2 Q_{\alpha\beta}(\mathbf{x},t) - L_2\,\overline{\nabla_\alpha(\nabla_\gamma Q_{\beta\gamma}(\mathbf{x},t))}\ ]. \end{aligned} \tag{1.36}$$

While these equations are adequate for analytical calculations of both static and dynamical correlation functions, the change of basis described in Eq.(1.13) is more convenient for numerical solutions. In this basis, the equation of motion takes the form,

$$\partial_t a_i = -\Gamma\ [(A + CTrQ^2)a_i + (B + 6E'TrQ^3)T^i_{\alpha\beta}\,\overline{Q^2_{\alpha\beta}} - L_1\nabla^2 a_i - L_2\,\overline{T^i_{\alpha\beta}T^j_{\beta\gamma}\partial_\alpha\partial_\gamma a_j}\ ]. \tag{1.37}$$

The full set of five coupled nonlinear equation are shown in Appendix A.

The advantage of this change of basis is now apparent. Rather than solve for the dynamics of the full 3×3 matrix $Q_{\alpha,\beta)}$, as Eq.(1.36) would suggest, the transformation ensures that we solve only for the 5 independent parameters which define a symmetric, traceless matrix. In this basis, tracelessness is ensured *apriori*, leading to considerable numerical simplification.

1.6 Organization of the thesis

We briefly describe the outline of the subsequent chapters of this thesis.

- CHAPTER 2 describes the dynamics of the orientational tensor in the presence of thermal fluctuations. We discuss the autocorrelations and structure factor within both the linear and nonlinear theory of nematic liquid crystals.

- CHAPTER 3 discusses a numerical methodology for solving the dynamics of the nematic orientational tensor at zero and finite temperature. We benchmark our codes against known results. We then show how these methods can be incorporated in high performance computational codes and illustrate several visualization techniques that we have developed.

- CHAPTER 4 is devoted to the application of numerical methods to the study of the isotropic-nematic interface. It starts with providing a numerical proof of the "de Gennes ansatz" for the I-N interface with planar anchoring. A calculation of biaxiality with non-zero L_2 parameter is also presented. The chapter concludes with a discussion of the interface with oblique anchoring.

---

[2] In a more general case, $\Gamma = \Gamma(\mathbf{Q})$

- Chapter 5 studies phase ordering in quenches to the uniaxial and biaxial phase from the isotropic phase. Our results describe the morphology of complex defects, study the separation of time scales and extract associated dynamical scaling exponents obtained at different times. We also study the effect of thermal fluctuations on defect statistics.
- Chapter 6 describes the nucleation kinetics of uniaxial nematic droplets in two and three dimensions. We characterize droplet conformations, obtaining signatures of defect structures inside droplets.
- Chapter 7 concludes the thesis with a summary of the main results and suggestions for future directions which could extend the work presented in this thesis.

Chapter 2

Order parameter fluctuation in nematic liquid crystal

In this chapter we present explicit noisy Langevin equations for the time evolution, within the time-dependent Ginzburg-Landau-de Gennes model, of the components of the nematic order parameter $Q_{\alpha\beta}$. We show how these equations can be used to obtain the static and dynamic correlations of the order parameter. We calculate these correlations in the linear as well as in the non-linear theory. The stochastic forces which enter these TDGL equations are expanded in an appropriate symmetric tensorial basis, ensuring the traceless symmetric property of the order parameter at all times.

While earlier analytic calculations of Stratonovich probed the static and dynamic properties in the linear regime [67], a purely analytic calculation within the fully non-linear theory appears to be impossible. No numerical approach to the problem exists in the literature. The methodology described and used in this chapter and subsequent ones enables us to numerically check the results of the linear theory as well as to address the non-linear noisy problem for the first time.

2.1 Introduction

Liquid crystals are easily deformable by thermal forces. In thermal equilibrium, individual nematic particles are immersed in an heat bath of surrounding molecules. Interactions with these molecules lead to random thermal forces acting on the particles and dissipation in the form of heat. Thus, while on an average the mean velocity of each particle is zero, the standard deviation of velocity fluctuations is non-zero. At equilibrium, the strength of thermal fluctuations and the magnitude of energy dissipation are connected to the temperature of the bath via a fluctuation-dissipation relation. Quantitatively, the strength of fluctuations is manifest in two point correlations of the order parameter. This correlation function is measured in light scattering experiments [55].

In the isotropic phase, correlations in the orientational tensor are described by an Ornstein-

Zernicke form [53],

$$\langle Q_{\alpha\beta}(0)Q_{\mu\nu}(\mathbf{x})\rangle \sim \frac{e^{-|\mathbf{x}|/\xi}}{|\mathbf{x}|^{(d-1)/2}}[\delta_{\alpha\mu}\delta_{\beta\nu}+\delta_{\alpha\nu}\delta_{\beta\mu}-\frac{2}{3}\delta_{\alpha\beta}\delta_{\mu\nu}] \tag{2.1}$$

where d is the dimension and ξ is a correlation length measuring the characteristic distance over which fluctuations are correlated. This correlation length ξ increases rapidly as the supercooling temperature T^* is approached, diverging as $(T-T^*)^{-\nu}$ with $\nu = 0.5$, a divergence which is preempted by the isotropic-nematic transition in equilibrium. These "nematic swarms", nematic droplets of size ξ, produce enhanced opalescence close to the isotropic-nematic transition, in many ways resembling the critical opalescence seen in fluids close to their critical points arising out of large-scale density fluctuations [24].

Fluctuations in the nematic phases are disregarded in the previously studied liquid crystal problems, as the free energy differance between different phases are typically larger than the thermal energy k_BT [77]. However, fluctuations play a central role in the dynamics and the transition pathways between different phases. It is crucial to incorporate noise in the problems that we have studied and their importance will be apparent in the later chapters of the thesis. Fluctuations in the uniaxial nematic phase of a liquid crystal have been studied with the assumption that such effects only affect the director degree of freedom, preserving the magnitude of the nematic order parameter S. In general however, the nematic order parameter has five independent components. Although the Ericksen-Leslie theory of nemato-hydrodynamics has been widely used to study dynamical properties, it neglects fluctuations in the amplitude of uniaxiality in the uniaxial nematic phase, as well as biaxial fluctuations. A systematic way to account for these different fluctuations is to study the dynamics of the full tensor $\mathbf{Q}$.

In the next section we derive fluctuating equations of motion for $\mathbf{Q}$. In subsequent sections, we show how this equation of motion may be used to calculate static and dynamic correlators in the isotropic as well as the uniaxial nematic phase.

2.2 Fluctuating kinetics of the order parameter

In the high density and high viscosity limit, fluctuations in the local density and velocity are small and can be neglected. In the limit that hydrodynamic interactions may be neglected, *i.e.* the Rouse or free-draining limit, the dynamical fluctuations of $Q_{\alpha\beta}$ are not coupled to the fluctuations in other hydrodynamic variables. At non-zero temperature, the bath variables exert a fluctuating force on the molecules of the nematic sample. This in turn results in fluctuations in the local orientation of the nematic. In the presence of thermal fluctuations, the Langevin equations for the nematic orientation tensor are those appropriate to a non-conserved order parameter with an overdamped, relaxational dynamics of the form [11]

$$\partial_t Q_{\alpha\beta} = -\Gamma_{\alpha\beta\mu\nu}\frac{\delta F}{\delta Q_{\mu\nu}} + \xi_{\alpha\beta}, \tag{2.2}$$

where the kinetic coefficient $\Gamma_{\alpha\beta\mu\nu}$ is defined in Eq.(1.35). In the uniaxial nematic phase having long range interaction between the molecules, a more complicated form of the kinetic coefficient involving the symmetry allowed terms of the orientation tensor may be sought[1].

The $\xi_{\alpha\beta}$ are symmetric, traceless Gaussian white noises, which satisfy a fluctuation-dissipation relation at equilibrium of the form

$$\begin{aligned} \langle \xi_{\alpha\beta}(\mathbf{x},t)\rangle &= 0, && (2.3)\\ \langle \xi_{\alpha\beta}(\mathbf{x},t)\xi_{\mu\nu}(\mathbf{x}',t')\rangle &= 2k_BT\Gamma_{\alpha\beta\mu\nu}\delta(\mathbf{x}-\mathbf{x}')\delta(t-t'). && (2.4)\end{aligned}$$

Here k_B is the Boltzmann constant, T is the temperature of the bath and $\langle\rangle$ denotes the average over the probability distribution of the noise ξ. These Langevin equations, together with the fluctuation-dissipation relation for the noise, ensure that the stationary one-point probability distribution of $Q_{\alpha\beta}$, $P[Q_{\alpha\beta}]$, converges to Boltzmann equilibrium in the long time limit with $P[Q_{\alpha\beta}] \sim \exp(-F/k_BT)$.

The equations presented above are five coupled, non-linear stochastic partial differential equations, with a noise term which has a tensorial structure. A numerical method of solution must maintain the symmetry and traceless of $Q_{\alpha\beta}$. To ensure equilibrium dynamics, it must also maintain the balance between fluctuation and dissipation. These two stringent requirements may be satisfied by transforming to a basis in which $Q_{\alpha\beta}$ is traceless and symmetric by construction. Symmetry and tracelessness of $Q_{\alpha\beta}$ is then automatically ensured. The noise can be constructed out of independent Gaussian noises.

Here we present an explicit construction of the noise, implemented by expanding in the same basis. We write

$$\xi_{\alpha\beta}(\mathbf{x},t) = \sum_{i=1}^{5}\xi_i(\mathbf{x},t)T^i_{\alpha\beta}, \tag{2.5}$$

where each $\xi_i(\mathbf{x},t)$ is a zero-mean Gaussian white noise. From the orthogonality of the basis the inverse relation is

$$\xi_i(\mathbf{x},t) = \sum_{\alpha,\beta}\xi_{\alpha\beta}(\mathbf{x},t)T^i_{\alpha\beta}. \tag{2.6}$$

From this, and the fluctuation-dissipation relation it follows that

$$\begin{aligned} \langle \xi_i(\mathbf{x},t)\xi_j(\mathbf{x}',t')\rangle &= \sum_{\alpha\beta\mu\nu}\langle \xi_{\alpha\beta}(\mathbf{x},t)\xi_{\mu\nu}(\mathbf{x}',t')\rangle T^i_{\alpha\beta}T^j_{\mu\nu}, && (2.7)\\ &= \sum_{\alpha\beta\mu\nu} 2k_BT\Gamma_{\alpha\beta\mu\nu}T^i_{\alpha\beta}T^j_{\mu\nu}\delta(\mathbf{x}-\mathbf{x}')\delta(t-t'), \\ &= 2k_BT\Gamma\delta_{ij}\delta(\mathbf{x}-\mathbf{x}')\delta(t-t'). \end{aligned}$$

This shows that the non-trivially correlated noise $\xi_{\alpha\beta}$ can be constructed from uncorrelated noises ξ_i. Thus, by construction, the noise $\xi_{\alpha\beta}$ is symmetric, traceless and satisfies the fluctuation-dissipation relation.

---

[1] In the uniaxial nematic phase, Stratonovich has shown that three fourth rank tensors incorporating combinations of the director $\mathbf{n}$ and δ can account for the two transverse fluctuations along with the longitudinal fluctuation of the nematic director [67].

The equations of motion in this basis are [11],

$$\partial_t a_i \quad = \quad -\Gamma\,[(A + C\mathrm{Tr}Q^2)a_i + (B + 6E'\mathrm{Tr}Q^3)T^i_{\alpha\beta}\,\overline{Q^2_{\alpha\beta}} - L_1\nabla^2 a_i] + \xi_i. \tag{2.8}$$

where $\overline{Q^2_{\alpha\beta}}$ is the traceless symmetric projection of $Q^2_{\alpha\beta}$.

2.3 Static and dynamic correlations

Static and dynamical correlations in the isotropic and nematic phases can be calculated using the Langevin equations described above. The real-space correlation function is defined as

$$C(\mathbf{r}, t) = \frac{\int d^3\mathbf{x}\; Q_{\alpha\beta}(\mathbf{x}, t)Q_{\beta\alpha}(\mathbf{x} + \mathbf{r}, t)}{\int d^3\mathbf{x}\; Q_{\alpha\beta}(\mathbf{x}, t)Q_{\beta\alpha}(\mathbf{x}, t)}, \tag{2.9}$$

while its Fourier transform is,

$$S(\mathbf{k}, t) = \frac{Q_{\alpha\beta}(\mathbf{k}, t)Q_{\beta\alpha}(-\mathbf{k}, t)}{\int d^3\mathbf{k}\; Q_{\alpha\beta}(\mathbf{k}, t)Q_{\beta\alpha}(-\mathbf{k}, t)}. \tag{2.10}$$

We evaluate these functions numerically (Chapter 5). We present the auto-correlation and the structure factor[2] for the fluctuating nematic theory in the Gaussian approximation and the uniaxial nematic case in the subsections which follow.

2.3.1 Correlations in the linear theory

When anharmonic terms are ignored in the GLdG free energy functional, the Langevin equations are linear and correlation functions can be calculated explicitly in the **T** basis. The Langevin equations of motion in Fourier space in terms of

$$a_i(\mathbf{q}, t) = \int d^3x \exp(-i\mathbf{q}\cdot\mathbf{x})a_i(\mathbf{x}, t), \tag{2.11}$$

are

$$\partial_t a_i(\mathbf{q}, t) = -\Gamma(A + L_1 q^2)a_i(\mathbf{q}, t) + \xi_i(\mathbf{q}, t). \tag{2.12}$$

From this expression, the static and dynamic correlations follow immediately,

$$C_{ij}(\mathbf{q}) = \langle a_i(\mathbf{q})a_j(-\mathbf{q})\rangle = \frac{k_B T}{A + L_1 q^2}\delta_{ij}, \tag{2.13}$$

and

$$\begin{aligned} C_{ij}(\mathbf{q}, \tau) \quad &= \quad \langle a_i(\mathbf{q}, t)a_j(-\mathbf{q}, t + \tau)\rangle \\ &= \quad C_{ij}(\mathbf{q})\exp[-\Gamma(A + L_1 q^2)\tau], \end{aligned} \tag{2.14}$$

The static and dynamic correlations for $Q_{\alpha\beta}$ are then obtained by returning to the original basis. The stationary probability distribution generated by the Langevin dynamics is Gaussian with zero mean and variance $C_{ij}(\mathbf{q})$, consistent with Boltzmann equilibrium.

---

[2] The auto-correlation is defined as the correlation in time (in real or in Fourier space) of the order parameter fluctuations while the structure factor is the correlation in space at equal times.

2.3.2 Correlations in the nonlinear theory

The nematic equations of motion [Eq.(2.8)] are plainly anharmonic and the analytical solutions obtained in the previous subsection within the harmonic expansion are no longer available for comparison. To study the correlations in the fluctuating uniaxial nematic phase ($E' = 0$), we extract the fluctuations of the angular displacements from the uniform nematic ground state using an approach based on the Frank free energy.

Consider an uniform uniaxial nematic with director $\mathbf{n}_0$ with small fluctuations $\delta\mathbf{n}(\mathbf{x})$. Decomposing the fluctuations into parts parallel and perpendicular to $\mathbf{n}_0$ and imposing the normalization of the director, we find from the Frank free energy that,

$$\langle|\delta\mathbf{n}_\perp(\mathbf{q})|^2\rangle = \frac{k_B T}{K q^2}, \tag{2.15}$$

where $K = (9S^2/2)L_1$ is a Frank constant [32]. This arises due to the the hydrodynamic character of director fluctuations about the uniform $\mathbf{n}_0$ obtained in the ordered phase. These fluctuations are Goldstone modes. Since fluctuations in the plane perpendicular to $\mathbf{n}_0$ can be characterized through a single angle θ, an equivalent result is

$$\langle\theta(\mathbf{q})\theta(-\mathbf{q})\rangle = k_B T/K q^2. \tag{2.16}$$

2.4 Conclusion

In this chapter, we have presented a fluctuating model-A TDGL equation for the nematic orientation tensor. Such an an equation has not, to our knowledge, appeared before in the literature, possibly because the $\mathbf{Q}$ description is somewhat more uncommon than the Frank description in terms of the director $\mathbf{n}$. The tensor form of the stochastic force is constructed so as to satisfy the symmetry and tracelessness properties of the tensorial order parameter at all times, while its magnitude is chosen so as to obey the fluctuation dissipation relation. We have shown how such a construction leads us to a set of five coupled non-linear stochastic differential equations, which can be numerically integrated. An accurate numerical methodology can then provide a way to benchmark analytic calculations in the fully non-linear regime as well as allow calculations in a regime where order parameter amplitude fluctuations cannot be neglected.

We present such a methodology in the next Chapter, which we then use to evaluate static and dynamic correlations in the linear theory, comparing these results to the analytic ones obtained above. The transverse correlation of the director is calculated in the fully non-linear theory where analytic results do not exist and compared to results based on the expansion method indicated above.

Chapter 3

Numerical method for order parameter dynamics

In this chapter, we describe several numerical methodologies for the integration of the tensorial nematic equation of motion obtained in the previous chapter. We believe that these methods are applied to the study of the dynamic behaviour of nematic liquid crystals for the first time.

We first illustrate the non-dimensionalization of the different parameters arising in the Landau-de Gennes theory, thus setting basic length and time scales for the problems addressed in this thesis. We describe a numerical method, known as the method of lines, for integrating the deterministic part of the equation without approximation, illustrating this method using a parabolic initial value problem. The numerical implementation makes it possible to address several long-standing problems without resort to approximations: the structure of the isotropic-nematic interface, the structure of nematic droplets in an isotropic environment and dynamical scaling in coarsening kinetics. These form the topics of later chapters.

We then present a highly accurate technique for discretizing the derivative operator appearing in the GLdG equation. This spectral collocation technique is implemented for the first time, to our knowledge, for the TDGL equations for nematics. We illustrate the underlying idea using the example of a scalar equation. The accuracy of the technique makes it possible to understand several subtle properties of the isotropic-nematic interface. It can be applied to several associated problems which have not yet been addressed due to lack of efficient numerical methods [57].

We calculate the two-point correlations in real and Fourier space for the general nematic problem, working with the full non-linear theory. We then describe how these techniques can be extended to high performance computation. We conclude this chapter with an illustration of a new visualization technique for scalar and tensor fields relevant to our problem.

3.1 Introduction

The equations for the relaxational dynamics of the orientational order parameter presented in the previous chapter are a set of five coupled and parabolic differential equations. These

Uniaxial order	$S = 3(1 + \sqrt{1 - 24AC/B^2})/4$
Uniaxial order at coexistence	$S_c = -2B/9C$
Free energy at coexistence	$\mathcal{F}_c = 9CS_c^4/16$
Correlation length	$l_c = \sqrt{54C(L_1 + 2L_2/3)/B^2}$
Relaxation time	$\tau = (\Gamma \mathcal{F}_c)^{-1}$

Table 3.1: The dimensional parameters used for non-dimensionalization the order parameters, free energy with length and time scale.

are highly non-linear, contain anisotropic gradient terms and are coupled strongly to each other.

The problems we study are categorized into two classes. One ignores the effect of fluctuations and focuses on the solution of the five partial differential equations (PDE). The other class of problems incorporates the fluctuating noise term, thus making these equations stochastic differential equations. No analytical solutions are available for these equations in general in either of these cases. Efficient and accurate numerical methods must therefore be sought. Conventionally, the methods used to solve the deterministic equations are based on the standard finite difference technique [77]. The elegancy in our method can be well justified in terms of computational efficiency, when extended to the stochastic problems, as discussed in the subsequent sections.

3.2 Non-dimensionalization of the parameters

We scale the order parameter as $Q^*_{\alpha\beta} = Q_{\alpha\beta}/S_c$ and $S^* = S/S_c$, while the free energy is scaled as $\mathcal{F}^* = \mathcal{F}/\mathcal{F}_c$. Here $\mathcal{F}_c$ is proportional to the free energy barrier between the isotropic and nematic minima at coexistence. We measure lengths in units of l_c. Finally, time is non-dimensionalised by the characteristic relaxation time τ.

The dimensional quantities which we use to scale the parameters are defined in terms of the Landau parameters in the Table 3.1. We choose the discretization length $\Delta x = \Delta y = \Delta z = 1$ and the integration time step $\Delta t = 1$. These define simulation units of length and time. To ensure that discretization errors and artifacts are kept to a minimum, the discretization length must be much smaller than the characteristic length $\Delta x = \Delta y = \Delta z \ll l_c$. The integration time step must be much smaller than the characteristic time scale $\Delta t \ll \tau$. The dimensionless discretization scales must then satisfy $\Delta x \rightarrow \Delta x/l_c \ll 1$, $\Delta y \rightarrow \Delta y/l_c \ll 1$, $\Delta z \rightarrow \Delta z/l_c \ll 1$ and $\Delta t \rightarrow \Delta t/\tau \ll 1$.

Our simulations are performed maintaining the above conditions, on grid sizes ranging from 16^2 to 1024^2 in two dimensions and 32^3 to 256^3 in three dimensions.

3.3 Method of lines

In this section we present a method, based on the strategy of semi-discretization, whereby an initial value deterministic PDE is discretized only in the spatial variables to yield a set of coupled ordinary differential equations (ODE). These ODEs can be solved using powerful general purpose solvers. In the literature, this semi-discretization strategy goes by the name of the '*method of lines*' (MOL) [44, 43], since the solutions are obtained along fixed lines in the space-time plane.

To illustrate the idea of MOL, consider a parabolic initial-value problem in a single spatial variable x, the diffusion equation for a scalar field $\psi(x,t)$ given as,

$$\partial_t \psi(x,t) = D\nabla^2 \psi(x,t). \tag{3.1}$$

The semi-discretization technique proceeds by restricting the field $\psi(x,t)$ to a set of N discrete 'collocation' points, $x_n = n\Delta x$, $n = 1, 2, \ldots, N$, spaced Δx apart, and then uses a discrete approximation for the Laplacian based on these points. The simplest of these approximations is based on local polynomial interpolation, resulting in finite difference (FD) schemes [43]. However, the MOL is not restricted to finite differences. When high accuracy is needed, global interpolation based on trigonometric or Chebyshev polynomials can be used to generate spectral approximations of derivatives [70]. When conservation laws need to be respected, finite volume approximations to the derivatives can be used [42]. In complicated geometries, a finite-element discretization may be the most appropriate.

In this example, the simplest approximation is based on nearest-neighbour finite differences, for which

$$\nabla^2 \psi(x_n) = \frac{1}{(\Delta x)^2}[\psi(x_{n+1}) - 2\psi(x_n) + \psi(x_{n-1})] + O[(\Delta x)^2]. \tag{3.2}$$

Inserting this into the diffusion equation, we obtain a set of coupled ordinary differential equations

$$\partial_t \psi(x_n, t) = \frac{1}{(\Delta x)^2}[\psi(x_{n+1}) - 2\psi(x_n) + \psi(x_{n-1})]. \tag{3.3}$$

This coupled set of ODEs, together with initial and boundary conditions, can now be integrated with a suitable numerical integration scheme which ensures accuracy, efficiency, and stability. It is at this stage that the flexibility of the MOL is most apparent, since any number of numerical integration schemes can be implemented without affecting the spatial discretization. Depending on the nature of the system of ODEs, the optimal choice may be either an explicit scheme, an implicit scheme, or one which is designed to handle stiffness. In the above example, for instance, it is well known that an explicit Euler integration scheme leads to an instability unless the time step Δt is constrained by the Courant-Friedrichs-Lewy condition $\Delta t < (\Delta x)^2/2D$ [43]. In contrast, an implicit integration scheme based on the trapezoidal rule gives the stable Crank-Nicolson update [43]. In general, semi-discretization followed by numerical quadrature provides an elegant way of deriving many of the well-known schemes for parabolic PDEs.

The practical implementation of PDE solvers using the MOL discretization is simple since the spatially discretized ODE system can be passed directly to a general purpose ODE solver. The complexity, both algorithmic and computational, in the numerical integration can thereby be transferred directly to the ODE solver library.

We have followed the MOL discretization to construct a solver for PDEs describing the deterministic dynamics of the orientational order parameter presented in the previous chapter. We have used standard nearest-neighbour second-order accurate finite difference formula for first and second derivatives in the spatial discretization [1]. More accurate difference approximations to derivatives can be obtained using Fornberg's general formula [29]. For the temporal integration, we have used the ODE solver routines in the GNU Scientific Library [27]. For the problems we study in this thesis, we find that an explicit multi-stage integrator gives a good compromise between accuracy, stability and computation expense.

Finally, it should be mentioned that the MOL discretization is not restricted to parabolic initial value problems, but also applies to hyperbolic and mixed parabolic - hyperbolic PDEs [44]. This allows the method to be extended to situations where effects of advection from hydrodynamic flow need to be accounted for. On an Intel(R) Core(TM)2 Duo CPU with speed 2.66GHz, the MOL code takes 0.33 seconds for one time step once a lattice size of 256^2.

3.4 Spectral collocation technique

The simplest way of deriving the FD form of the derivative presented in Eq.(3.2) is to construct a local polynomial interpolant $P(x_n)$ of degree ≤ 2 with $P(x_{n+1}) = \psi_{n+1}, P(x_n) = \psi_n$ and $P(x_{n-1}) = \psi_{n-1}$ and differentiating $P(x_n)$ and evaluating at $x = x_n$. The degree of the polynomial can be increased to yield a dense differentiation matrix that converges as $O[(\Delta x)^{degree}]$. In the spectral collocation method (SCM), the spatial part is discretized through an expansion in an orthogonal basis of Chebyshev polynomials in a bounded interval. The spatial discretization is done on the Chebyshev points $x_j = \cos(j\pi/N), j = 0, 1, \cdots, N$ which are the projections of equispaced points on the upper half periphery of a unit circle on the x-axis bounded by the interval $[-1, 1]$. This points which cluster mostly at the boundaries, constructed from Chebyshev polynomials, are used to construct the differentiation matrix. This is carried out by construction of a global polynomial interpolant $\leq N$ and differentiation and evaluation of the interpolant at the required space point. Differentiation operators constructed from this Chebyshev interpolant are spectrally accurate, in the sense that the error vanishes exponentially in the number of retained polynomials.

The implementation of boundary condition in SCM is fairly straightforward for the problems related either to a bounded interval or an open interval. For problems with periodic domain, trigonometric polynomial interpolant is constructed on equispaced grid, whereas, for problems with non-periodic domain, algebraic polynomial interpolant is constructed on unevenly spaced grid, one of the examples are the Chebyshev interpolant. Imposing either

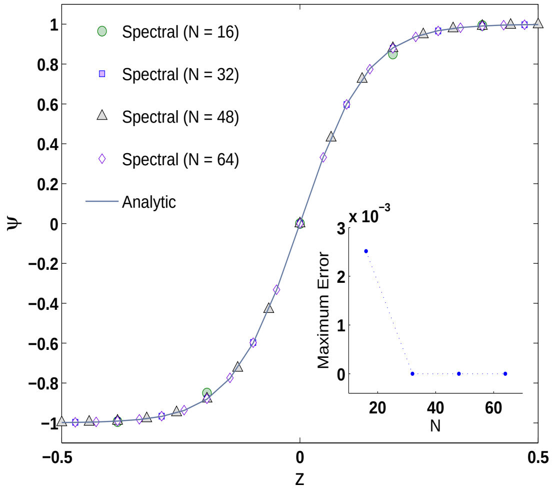

Figure 3.1: Variation of the scalar magnetization ψ across the planar interface. Symbols represent spectral data, solid curves are the analytic solution of Eq.(3.4). The inset shows the maximum error obtained doing a spectral calculation in the least square approximation. The numerical parameters are $\epsilon = 0.01$ and $N = 16, 32, 48$ and 64.

Dirichlet, Neumann or Robin boundary condition[1] is easy to implement in SCM, which can either be implemented through restricting the interpolants to satisfy the boundary condition or by adding additional equations to enforce the boundary condition without restricting the interpolant.

3.4.1 Benchmark of Allen-Cahn equation

To illustrate the idea of SCM, consider a parabolic initial-value problem in a single spatial variable z: the one dimensional Allen-Cahn bistable equation for a scalar field $\psi(z, t)$ representing a nonlinear reaction-diffusion system given as

$$\partial_t \psi(z, t) = \psi(z, t) - \psi^3(z, t) + \epsilon \nabla^2 \psi(z, t), \tag{3.4}$$

whose solution has a profile $\psi(z, t) = tanh(z/\xi)$ bounded between ±1 and $\xi = \sqrt{2\epsilon}$ denote the correlation length. The interpolant is constructed so as to satisfy Dirichlet boundary conditions. In Fig.(3.1), we plot the equilibrium profile of $\psi(z)$ with increasing number of Chebyshev polynomial N from 16 to 64. In the inset, we show how the maximum error committed using the SCM goes down with N. The DMSUITE library is used for the numerical implementation of SCM [74].

---

[1] The Dirichlet condition specifies field values at the boundary, the Neumann condition specifies the derivative of the field at the boundary while the Robin condition specifies both Dirichlet and Neumann conditions simultaneously at the boundary.

3.5 Stochastic method of lines

The fluctuating nematodynamic equations contained in Eq.(1.34) are five non-linear stochastic partial differential equations which can only be studied numerically. Here we combine the method of lines for solving initial-value PDEs presented in the previous section, with a stochastic version of the Runge-Kutta integrator for systems of stochastic ordinary differential equations. This enables us to construct an accurate and efficient solver for the equations of fluctuating nematodynamics. The results we present in this thesis were first described in [10], where a method of lines approach was used to solve the deterministic time-dependent Ginzburg-Landau equations numerically. The methodology here can thus be thought of as a generalization of the method of lines to stochastic PDEs. To apply the MOL to stochastic PDEs, we must account for the fact that integrators for ODEs do not automatically provide efficient and accurate solutions of stochastic differential equations (SDE). Qualitatively, the noise term in a SDE is a rapidly varying function and hence must be integrated with some care. At a more technical level, the noise is a Wiener process and the theory of stochastic integration must be used to evaluate it correctly [31].

Common stochastic integrators include those due to Maryuama [46] and Milstein [50]. In our work, we use an integrator proposed recently by Wilkie [75], based on a multi-step Runge-Kutta strategy. The integrator is accurate and easy to implement by making small changes to a deterministic Runge- Kutta integrator. Further, since it is an explicit integrator, no matrix inversions are involved. This makes it attractive when the MOL semi-discretization produces a large system of ODEs, as in our case.

3.5.1 Benchmark of Ornstein-Uhlenbeck process

To test Wilkie's algorithm for a stochastic Runge-Kutta integrator (SRK4), and to check the validity of the fluctuation-dissipation relation, we perform a simple benchmark test on the Ornstein-Uhlenbeck process, which is the velocity of a Brownian particle represented as the Ito differential equation,

$$dv(t) = -\Gamma v(t)dt + dW(t), \tag{3.5}$$

where $dW(t) = \sqrt{2k_BT\Gamma dt}\,\mathcal{N}(0,1)$ is the increment of the stochastic variable in the interval dt, and $\mathcal{N}(0,1)$ is a zero-mean unit-variance normal deviate. By construction, the increments of this stochastic variable are independent and normally distributed with mean $\langle dW(t)\rangle = 0$. The particular choice of the variance ensures that the equilibrium distribution of v is a Gaussian with variance k_BT. The stationary two-point autocorrelation of the velocity from Eq.(3.5) is,

$$\langle v(t)v(t+\tau)\rangle = k_BT\exp(-\Gamma\tau). \tag{3.6}$$

Fig.(3.2) shows the autocorrelation as a function of time and the histogram of equal-time fluctuations of v. It is well known that statistical error committed due to a time integration over a single realization is error-prone with an uncertainly of 20% in order, which reduces by a factor of $1/\sqrt{N}$, where N is the number of independent realization of the sample [78]. The variance $\langle v^2\rangle = k_BT$ is correctly reproduced, as is the exponential decay of the

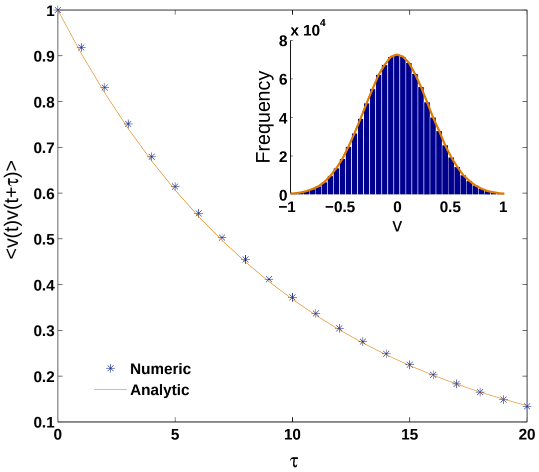

Figure 3.2: Autocorrelation function for the Ornstein-Uhlenbeck process, showing $\langle v(t)v(t+\tau)\rangle$ as a function of the time increment τ. The inset shows the histogram of fluctuations. It is Gaussian with the expected variance. The numerical parameters chosen are $\Gamma = k_BT = 0.1, dt = 1.0$. The average is taken over 10 independent realizations while the integration is performed for 10^6 SRK4 steps.

autocorrelation function. We conclude that SRK4 is suitable as an integrator for problems where the fluctuation-dissipation relation must be maintained.

3.5.2 Discretization of fluctuating nematodynamics

We now apply the MOL together with SRK4 to obtain a stochastic method lines (SMOL) discretization for the equations of fluctuating nematodynamics. We benchmark our numerical results by comparing autocorrelations within a harmonic theory which accurately describes fluctuations about the isotropic phase. We then consider expansions about the ordered state, comparing static correlations obtained analytically within the Frank approximation with our numerical results.

We use a FD discretization with nearest-neighbour stencils for gradients and the Laplacian. We implement periodic boundary conditions. Specifically in three dimensions, we consider a box of dimension L_x, L_y and L_z along the Cartesian directions, and grid these lengths with equal grid spacing $\Delta x = \Delta y = \Delta z = 1$. The latter defines lattice units for the spatial coordinate. We define corresponding discrete time units for the temporal variables by choosing $\Delta t = 1$. Fourier modes are labeled by the wave-vector $\mathbf{q} = (q_x, q_y, q_z)$, where each component is of the form $q_\alpha = 2\pi n_\alpha / L_\alpha$, with $n_\alpha = 0, 1, 2, \ldots, (L_\alpha - 1)$.

With this discretization, the Laplacian in Fourier space is given by

$$\mathcal{L}(\mathbf{q}) = 2[\cos(q_x) + \cos(q_y) + \cos(q_z) - 3]. \tag{3.7}$$

The nearest-neighbour finite difference stencil suffers from lack of isotropy at high wavenumbers. This can be improved through the use of higher-point stencils [1, 54, 65]. Applying the

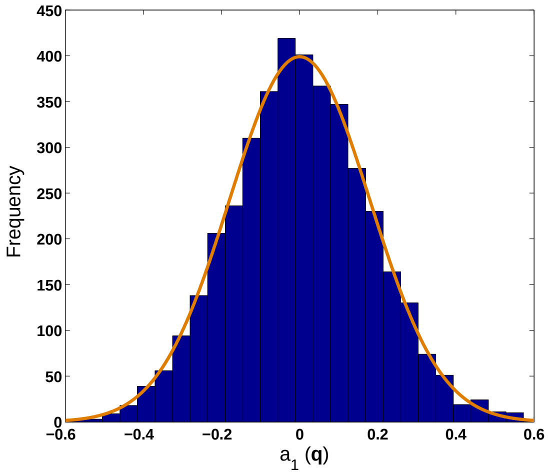

Figure 3.3: Histogram of the real part of $a_i(\mathbf{q})$ for $n_x = n_y = 6$ in a box of dimension $L_x = L_y = 16$, using a harmonic free energy, with $k_BT = A = 0.05$ and $L_1 = 0.5$, $\Gamma = 1.0$. The fluctuations are Gaussian with the expected variance. The histogram is obtained from 20 independent realizations, each realization contributing 4×10^3 time steps.

MOL semi-discretization to Eq.(1.34) reduces it to a system of stochastic ordinary differential equations, whose Fourier representation in the harmonic approximation of Eq.(2.12) is

$$\partial_t a_i(\mathbf{q}, t) = -\Gamma \mathcal{D} a_i(\mathbf{q}, t) + \xi_i(\mathbf{q}, t). \tag{3.8}$$

The Fourier representation of the drift-diffusion dynamics is encoded in the linear operator $\mathcal{D}$,

$$\mathcal{D} = A - L_1 \mathcal{L}(\mathbf{q}). \tag{3.9}$$

Fourier representations of the one and two-dimensional MOL semi-discretizations are obtained by setting the corresponding wavenumbers to zero.

3.5.3 Correlations in the linear theory

The static and dynamic correlations in Fourier space follow in a straightforward manner through the replacement of q^2 by its discrete Laplacian representation. The results are

$$C_{ij}(\mathbf{q}) = \frac{k_BT}{\mathcal{D}} \delta_{ij}, \tag{3.10}$$

$$C_{ij}(\mathbf{q}, \tau) = C_{ij}(\mathbf{q}) \exp(-\Gamma \mathcal{D} \tau). \tag{3.11}$$

It is also useful to define an angle-averaged structure factor $C(q) = \sum_{|\mathbf{q}|=q} C_{ij}(\mathbf{q}\rangle$ for comparison with the numerical simulation.

We now compare theoretical and numerical results: in Fig.(3.3) we show the histogram of the $a_i(\mathbf{q})$ for a particular Fourier mode. This is normally distributed, as expected, with zero

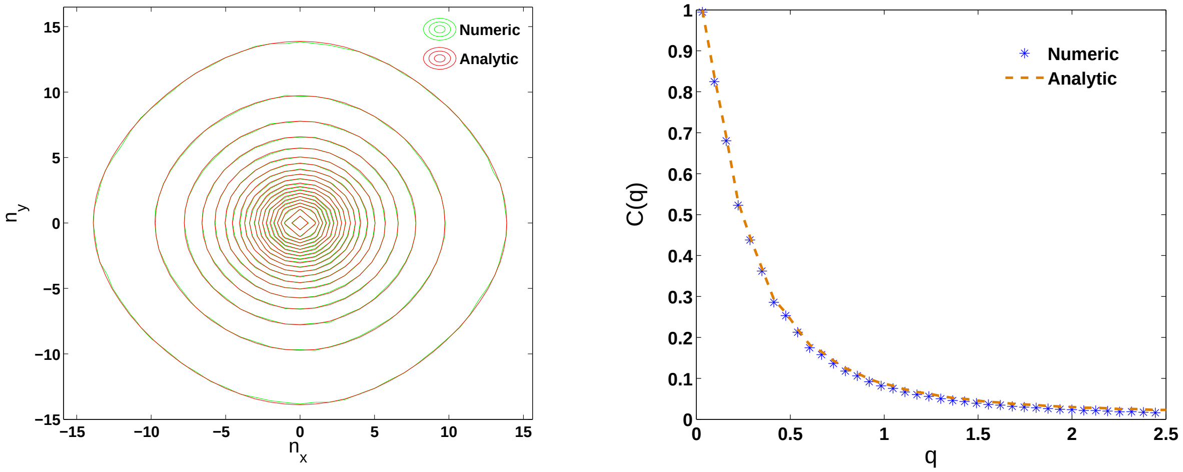

(a) (b)

Figure 3.4: (a) Contour plot of the structure factor $C_{ij}(\mathbf{q})$ and (b) angular average of $C_{ij}(\mathbf{q})$. The parameters are $k_BT = A = 0.05, L_1 = 0.5, \Gamma = 1.0$. The time averaging is over 5×10^4 time steps and ensemble averaging is over 20 independent realizations in a box with $L_x = L_y = 64$. The relaxation time scale for the shortest Fourier mode is $\tau = (\Gamma A)^{-1} = 20$ and the correlation length is $\lambda = \sqrt{L_1/A} = 3.16$.

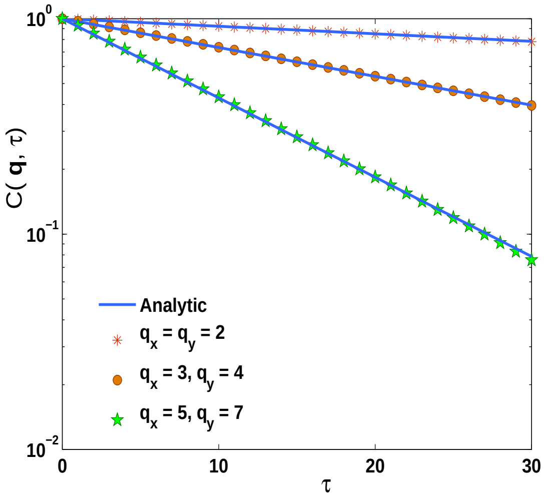

Figure 3.5: Autocorrelation $C_{ij}(\mathbf{q}, \tau)$ for the linear Langevin equation, calculated for small wavenumbers. Numerical parameters are $k_B T = A = 0.0035, L_1 = 0.015, \Gamma = 1.0$. The integration is performed for 5×10^4 time steps on a 16^2 grid. The time average is taken over 4×10^4 time steps and an ensemble average is taken over 25 independent realizations. Time scale for the longest relaxation of the shortest Fourier mode is $\tau = (\Gamma A)^{-1} = 285.7$, the fastest relaxation of the largest Fourier mode is $\tau = 8.1$. The correlation length $\lambda = \sqrt{L_1/A} = 2.1$.

mean and variance as required by thermal equilibrium. Similarly, all Fourier modes examined have correct normal distributions. The variances obtained are compared in Fig.[3.4(a)] with the analytical values by plotting contours of $C_{ij}(\mathbf{q})$. There appears to be excellent agreement.

A closer inspection reveals some degree of anisotropy in both the analytical and numerical results at high wavenumbers. This is attributed to the lack of isotropy of the nearest-neighbour finite-difference Laplacian mentioned earlier. However, the anisotropies are removed upon angular averaging, as shown in Fig.[3.4(b)]. Thus, the present discretization should be adequate in most cases, unless highly accurate isotropies are required from the simulation. From these results, we conclude that correlations in thermal equilibrium are accurately captured by the stochastic method of lines approach.

We next compare the dynamics of fluctuations at equilibrium, by comparing two-point autocorrelation functions calculated analytically and numerically. Fig.(3.5) shows $C_{ij}(\mathbf{q}, \tau)$ for three sets of Fourier modes. The exponential decay of the autocorrelation function is reproduced accurately within the numerics and fit the theoretical curve very closely. We conclude, therefore, that the stochastic method of lines accurately reproduces both static and dynamic fluctuations in a harmonic theory.

3.5.4 Correlations in the nonlinear theory

Finally, we compare theory and simulation in a situation where a linearization of the $Q_{\alpha\beta}$ equations about $Q_{\alpha\beta} = 0$ is inapplicable, that of director fluctuations within the nematic

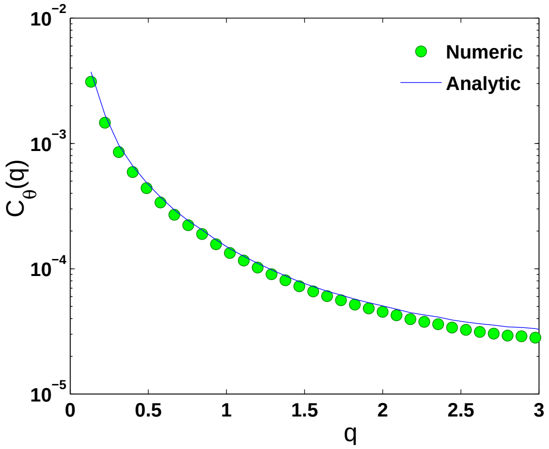

Figure 3.6: Angularly averaged structure factor of the nematic phase. The numerical parameters are $k_BT = 0.05, A = -3.5, B = -10k_BT, C = 2.67, L_1 = 32.0, \Gamma = 0.01$ on a 64^2 grid. The relaxation time scale is $\tau = (\Gamma A)^{-1} = 28.57$, the diffusion time scale of the shortest Fourier mode is $\tau_d = L_x^2/(4\pi^2 L_1 \Gamma) = 324.23$ and the correlation length is $\lambda = \sqrt{L_1/A} = 3.02$. The time average is taken over 5×10^4 time steps and an ensemble average is taken over 20 independent realizations.

phase. In the semi discrete representation, Eq.(2.16) takes the form,

$$\langle \theta(\mathbf{q})\theta(-\mathbf{q})\rangle = -\frac{k_BT}{K\mathcal{L}(\mathbf{q})}. \tag{3.12}$$

Fig.(3.6) shows the angular average of the static correlations of director fluctuations $C_\theta(q) = \sum_{|\mathbf{q}|=q}\langle \theta(\mathbf{q})\theta(-\mathbf{q})\rangle$. The formally divergent $\mathbf{q} = 0$ mode is excluded both from the numerical data and analytical result. Given that the analytical result is obtained from a linearization about the aligned state whereas the numerical solution is calculated from the equations of motion arising from the full non-linear free energy, the agreement between theory and simulation is satisfactory. The SMOL thus accurately captures equilibrium fluctuations in the ordered state as well as in the disordered one.

3.6 High performance computation

In principle, the nematic equations of motion can be numerically integrated on any platform. The time scale for the smallest Fourier mode in the problem to relax goes as $\tau \sim L^d$ where d is the number of space dimensions and L is the system size. However, there are occasions, such as the study of phase transitions, in which behaviour in the thermodynamic limit $L \to \infty$ must be studied, which then implies $\tau \to \infty$. Also, whenever multiple length and time scales coexist, a long time simulation of large system sizes must be performed.

A serial compute machine performs a time update by executing discrete sets of instructions on each lattice node in the subsequent clock time utilizing the CPU memory resulting

Number of processors	CPU time (in secs)
1	0.000392
2	0.000229
6	0.000122
10	0.000095
14	0.000084
18	0.000086
22	0.000076
26	0.000075
30	0.000070

Table 3.2: Scaling of the parallel code with the number of cores in a node for a 128^2 lattice.

into a computational time $\sim L^3$. This increase with system size implies that serial computing cannot access very large system sizes within achievable computational time. This is, instead, achieved through the use of parallel clusters, where the lattice is domain-decomposed into variable sized sub-lattices which are distributed to the processing elements (PE) that contain local information about the sub-lattice. A haloed region of grid spacing Δx owned by the neighboring processors is used to communicate the data between the PE's. Time updates are performed simultaneously on each compute machine of the cluster, thus reducing the computational time by a factor of $1/N$ where N is the number of machines in the cluster.

To remove the instabilities arising due to the use of explicit time update discussed in the previous sections and to achieve convergence of the algorithm of any order in Δt , an implicit time update have to be used. For this purpose, the Jacobian matrix J has to be inverted in each time update. In our algorithm, the Jacobian matrix has to be provided to the integrator to use this.

3.6.1 Benchmark of Allen-Cahn equation

To illustrate the idea, we simulate the dynamics of the Allen-Cahn equation, defined in Eq.(3.4) on a three dimensional lattice with linear dimension L_x, L_y and L_z. We use a lexicographic projection to construct a single index from the lattice index, defined as $m = i + jL_x + kL_xL_y$ where, i, j, and k varies from 0 to $L_x - 1$, $L_y - 1$ and $L_z - 1$ respectively. In the FD approximation, the equation reduces to the form,

$$\begin{aligned}\partial_t \psi_m &= [1 - \psi_m^2 - \frac{6\epsilon}{(\Delta x)^2}]\psi_m + \frac{\epsilon}{(\Delta x)^2}(\psi_{m+1} + \psi_{m-1} + \psi_{m+L_x} + \psi_{m-L_x} + \\ &\quad \psi_{m+L_xL_y} + \psi_{m-L_xL_y}) \end{aligned} \tag{3.13}$$

and the Jacobian matrix, defined as $J_{m;n} = \partial_t \psi_m / \partial \psi_n$ is,

$$\begin{aligned}J_{m;n} &= [1 - 3\psi_m^2 - \frac{6\epsilon}{(\Delta x)^2}]\delta_{m;n} + \frac{\epsilon}{(\Delta x)^2}(\delta_{m+1;n} + \delta_{m-1;n} + \delta_{m+L_x;n} + \delta_{m-L_x;n} + \\ &\quad \delta_{m+L_xL_y;n} + \delta_{m-L_xL_y;n}) \end{aligned} \tag{3.14}$$

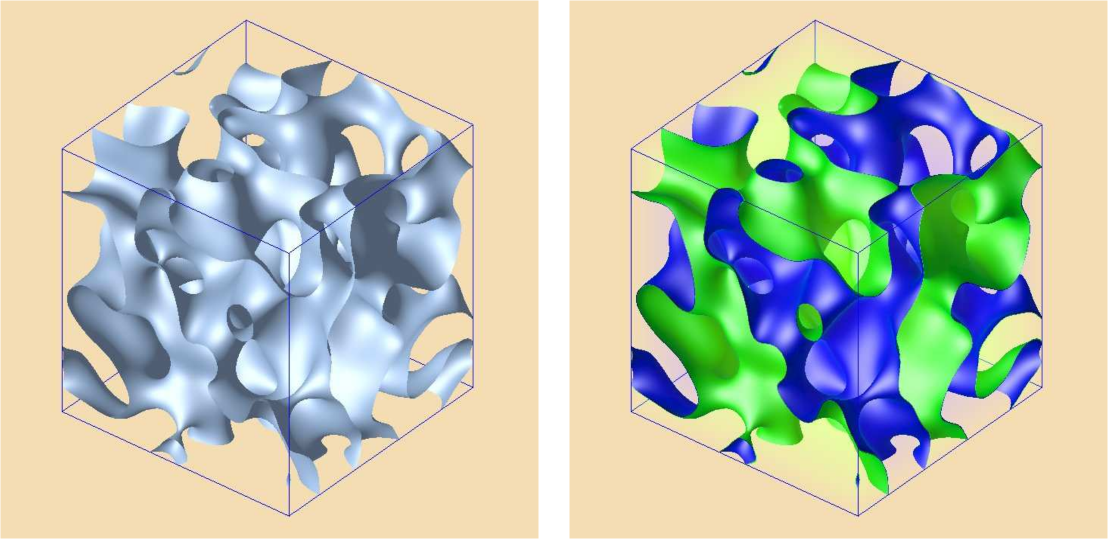
(a) (b)

Figure 3.7: Isosurfaces of the scalar parameter $\psi = 0.1$ at the 5.7×10^3 time step. The difference between the figures are Fig.[3.7(b)] is volume rendered with the values of ψ. The numerics is performed on a 256^3 unit spaced grid with $dt = .01$ and $\epsilon = 4.0$. The initial values are drawn from a random set having interval $(-0.1, 0.1)$

The Jacobian matrix for the nematic equations of motion is shown in the Appendix A.

3.7 Visualization of order parameter fields

3.7.1 Scalar field in Allen-Cahn equation

To visualize the statics and dynamics of the scalar field, we consider the Allen-Cahn equation in three dimensions, defined in Eq.(3.4). We use the MOL technique for the spatial discretization and Crank-Nicholson implicit integrator for the time update. We use the standard PETSc library [6] to domain-decompose the right hand side of the Eq.(3.13) as well as the Jacobian matrix defined in Eq.(3.14). For visualization in three dimensions purpose, we draw isosurfaces of the scalar field corresponding to a specific field value (isovalue).

Fig.[3.7(a)] shows the isosurfaces of the scalar magnetization at an isovalue $\psi = 0.1$. In Fig.[3.7(b)] we plot the isosurfaces shown in the previous frame, but in false colours so that the isosurface corresponding to $\psi = 0.1$ appear blue while $\psi = -0.1$ appear green. We also render the volume with false colours corresponding to the equilibrium field values ± 1, superimposed on the coloured isosurfaces. We notice the surface pinch-off effect at the upper-right corner of the right face of the rectangle. This creates a complete picture of spinodal quench, where the scalar order is set to ± 1 initially and the isosurfaces of lower order tries to equilibrate through the surface pinch off. As magnetization is not a conserved

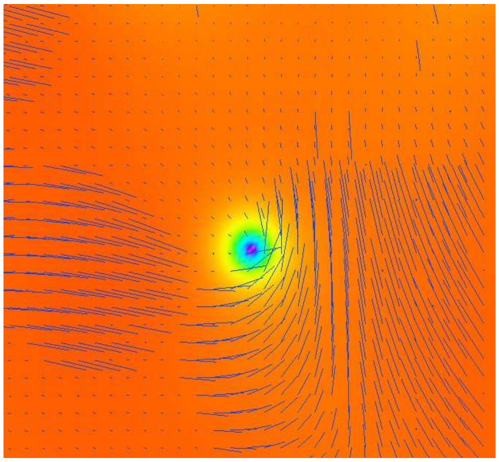

Figure 3.8: Scalar and vector field of the nematic orientation tensor.

quantity, the amount of surface area between ±1 is not constant.

3.7.2 Tensor field in nematics

The nematic orientation tensor consist of two scalar fields, which are the degree of uniaxial ordering S and degree of biaxial ordering T and three vector fields: the nematic director $\mathbf{n}$, codirector $\mathbf{l}$ and the joint normal to this as $\mathbf{m}$. The time update of the nematodynamic equations in the basis of a_i results in a set of a_i on each of the lattice points. With these values, the nematic orientation tensor $\mathbf{Q}$ can be reconstructed. This is symmetric and traceless by construction, but not necessarily diagonal. To extract the scalar and vectorial components from the $\mathbf{Q}$ tensor, we again choose a reference system aligned with the principal axis that diagonalizes the matrix. The largest eigenvalue of the diagonal matrix corresponds to S, while the difference between the other two eigenvalue correspond to T and the corresponding eigenvectors designate the [$\mathbf{nlm}$] triad.

To visualize the scalar field, we colour the field values on every lattice point with its respective value, using a specified convention, *e.g.* dark blue for the lowest value of the field and orange/red for the highest, and all other colours correspond to an ascending field values from blue to orange/red. We also perform a polynomial interpolation of the colours, which smoothen out the colour patches and a continuous coloured plane in two dimensions or volume in three dimensions results.

To visualize the vector field, we draw vectors at each lattice point with either the components in the three Cartesian directions or with the angular coordinates (θ, ϕ) whichever is available. As the parallel and anti-parallel direction are equivalent of the nematic director, we plot a ‘needle’ as opposed to an ‘arrow’ to designate the vector field. We obtain the director field imposed on top of the scalar field, as in Fig.(3.8) to easily visualize the physical situation.

3.8 Conclusion

In this chapter we have described the numerical techniques we will apply in subsequent chapters to solve the deterministic and the stochastic form of the dynamics of nematic orientation tensor. We have shown how the non dimensionalization of the parameters can lead to a simplification in the parameters. We have presented the method of lines applied to the dynamics followed by a spectral collocation technique. The *tanh* interface for the Allen-Cahn equation benchmarks our algorithm.

We then discuss the stochastic method of lines applied to the fluctuating dynamics of nematics. We benchmark the algorithm by calculating the velocity autocorrelation of a Brownian particle. We then exhibit a finite discretization of the dynamic equations, which can be used in the calculation of the static and dynamic correlators. We describe high performance computation applied to the dynamics of a scalar field. We conclude this part of the thesis with a visualization technique for the scalar field and show how a superimposed vector field description can be used for the visualization of the properties of the tensorial field.

Chapter 4

Local and nonlocal properties of the isotropic-nematic interface

In this chapter we discuss applications of the numerical methodology presented in the previous chapter to problems arising in the study of the isotropic-nematic interface. We solve the GLdG equations in equilibrium to obtain the profile of the nematic orientation tensor at the interface as well as in the bulk. We calculate the conformation of the isotropic-uniaxial nematic interface with different anchoring conditions imposed on the director asymptotically distant from the interface. Using our MOL scheme, we test the validity of the "de Gennes ansatz" for the isotropic-uniaxial interface, considering all degrees of freedom of the nematic orientation tensor, unlike previous work. These results demonstrate the validity of the de Gennes ansatz in a well-defined limit of the Landau-Ginzburg-de Gennes theory and specifically illustrates regimes when this ansatz breaks down [57].

In the following section, using our accurate spectral collocation scheme, we show how including elastic anisotropy leads to a biaxial interface with planar anchoring of the nematic director at the nematic boundary. In subsequent sections, by extending our spectral scheme to deal with an arbitrary anchoring of the nematic director, we show how oblique nematic anchoring breaks the local property of the interface, yielding a smooth profile of the tilt angle far from the interface.

We conclude the chapter with a discussion of the effects of thermal fluctuations on the roughness of the interface profile. This is, to our knowledge, the first GLdG calculation of the properties of the noisy isotropic-nematic interface. Such calculations, in the absence of *ad-hoc* approximation of the nematic equations have not been previously performed in the literature.

4.1 Introduction

Liquid crystalline states of matter provide a useful testing ground for statistical mechanical theories of interface structure, since a variety of ordered phases can be accessed in experiments and computer simulations. The structure of the isotropic-nematic (I-N) interface presents a simple example of how interfacial order can differ radically from order in the coexisting bulk phases, since biaxial order is generically expected at the interface even if the stable ordered phase is purely uniaxial.

Suppose we consider a nematic strip in the x-z plane sandwiched between an isotropic medium on both sides. The variation can occur in the z direction while translational symmetry excludes variation along the x direction. The free energy of the nematic strip per unit length consists of contributions both from the bulk term and the surface energy cost for the interface, given as

$$\mathcal{F}/L_z = -aL_x\Delta F + L_x\sigma, \tag{4.1}$$

where a is the stripwidth, L_x is the length of the interface, ΔF is the difference in the free energy density of the nematic to isotropic phase and σ is the line tension of the interface. At any temperature below or above coexistence, $\Delta F \neq 0$. Depending on the sign of ΔF, the interface moves with a velocity v resulting in either an isotropic medium or a nematic medium spanning the system size [56]. At coexistence, $\Delta F = 0$ and $v = 0$. The only contribution to the free energy comes from the surface term and the planar interface is stable in this regime.

The study of the isotropic-nematic interface within the framework of a Landau-Ginzburg description was initiated in an insightful paper by de Gennes [23]. To render the problem analytically tractable, de Gennes made a specific assumption regarding the variation of the components of the order parameter across the interface. For an infinitely extended interface where, by homogeneity, variations perpendicular to the interface alone are allowed, de Gennes assumed that the only quantity which changed across the interface was the uniaxial strength of ordering S. In the de Gennes ansatz, there is no biaxiality and no variation of the director across the interface. This reduces the nematic problem with five degrees of freedom to a more analytically manageable problem involving only a single degree of freedom. The variation of the ordering strength S along the coordinate z normal to the interface located at z_0 can then be obtained analytically as

$$S(z) = \frac{S_c}{2}(1 - \tanh\frac{z - z_0}{w}), \tag{4.2}$$

where $w = \sqrt{2}/S^*$ is the non-dimensional interfacial width, $S^* = S/S_c$ being the non-dimensional strength of ordering and S_c the value at coexistence.

The de Gennes ansatz is exact in the absence of elastic anisotropy. However, the description of the interface in the presence of such anisotropy poses a formidable analytic and numerical problem, since the partial differential equations for the five independent components of $Q_{\alpha\beta}$ contain non-linear couplings, while $Q_{\alpha\beta}$ is itself constrained by symmetry and the requirement that its trace vanish.

Popa-Nita, Sluckin and Wheeler (PSW) [57] studied the I-N interface incorporating elastic anisotropy in the limit of planar anchoring, adapting a parametrization introduced by Sen and Sullivan [64]. These authors neglected the *twist* distortion in their formulation and assumed that the director was contained always in a single plane (say x-z plane). This defines the [$\mathbf{nlm}$] triad through a single angle, called the local tilt angle, and defined as $\theta = \cos^{-1}(\mathbf{k}\cdot\mathbf{n})$. This reduces the five independent degrees of freedom of the problem to three. In the PSW parametrization, the principal axes of $Q_{\alpha\beta}$ remain fixed in space, and the problem reduces to the solution of two coupled non-linear partial differential equations

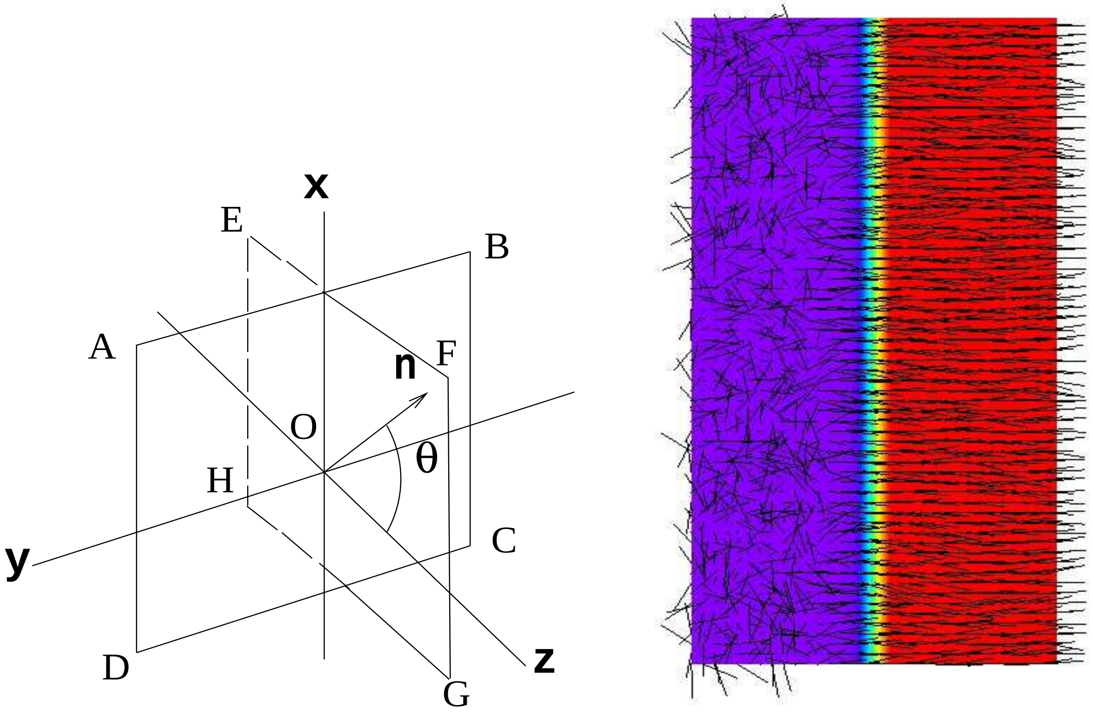

(a) (b)

Figure 4.1: Panel (a) depicts the interface geometry and the coordinate system used in our calculations. The nematic director makes an angle θ with the z axis. It can be chosen to vary between 0 (homoeotropic anchoring) and $\pi/2$ (planar anchoring). The isotropic phase is favoured through boundary conditions, as $z \to -\infty$, whereas the nematic phase is favoured for $z \to \infty$. The plane of the interface is the $x - y$ plane, shown by $ABCD$ in the figure, whereas the director is confined to the $EFGH$ plane as shown. The origin is denoted by O. In panel (b) we show a numerical realization of the interface neglecting thermal fluctuations and with a planar anchoring condition. The nematic strip of width 128 is sandwiched between isotropic phases with periodic boundaries.

in the dimension perpendicular to the interface. These equations represent the variation of the amplitude of uniaxial and biaxial ordering across the interface.

PSW obtained numerical solutions for the variation of S and T across the interface and showed that the solutions of these equations exhibited biaxiality in a region about the interface. The uniaxial order parameter (S) was adequately represented by a tanh profile, as in the original calculation of de Gennes, while the biaxial order parameter (T) exhibited more complex behaviour, peaking towards the isotropic side and with a trough on the nematic side. The biaxial profile was also shown to have a long tail towards the isotropic side, a feature hard to anticipate on physical grounds. For a general anchoring condition this parametrization breaks down, as is obvious from the fact that the order parameter has, in general, five independent components.

We begin with the GLdG expansion of the free energy for a general $Q_{\alpha\beta}$

$$\begin{aligned}\mathcal{F} &= \int dz d\mathbf{x}_\perp [\frac{1}{2}A\mathrm{Tr}\mathbf{Q}^2 + \frac{1}{3}B\mathrm{Tr}\mathbf{Q}^3 + \frac{1}{4}C(\mathrm{Tr}\mathbf{Q}^2)^2 \\ &\quad + \frac{1}{2}L_1(\partial_\alpha Q_{\beta\gamma})(\partial_\alpha Q_{\beta\gamma}) + \frac{1}{2}L_2(\partial_\alpha Q_{\alpha\gamma})(\partial_\beta Q_{\beta\gamma})]. \end{aligned} \tag{4.3}$$

where all the constants are having their meaning as defined previously. The variation happens in $\mathbf{z}$ direction while the interface is in the plane $\perp$ to $\mathbf{z}$ axis. We choose $A = B^2/27C$, thus enforcing phase coexistence between an isotropic and uniaxial nematic phase [32]. The interface is taken to be flat and infinitely extended in the $x-y$ plane. The spatial variation of the order parameter only occurs along the z direction [64].

In the case of planar anchoring, the ordering at infinity is purely uniaxial and taken to be along the x axis. In this case, as shown by Sen and Sullivan, uniaxial and biaxial order vary only with z and the principal axes of the $\mathbf{Q}$ tensor remain fixed in space. The form of $\mathbf{Q}$ is then

$$\mathbf{Q} = \begin{pmatrix} S & 0 & 0 \\ 0 & -\frac{1}{2}(S-T) & 0 \\ 0 & 0 & -\frac{1}{2}(S+T) \end{pmatrix}. \tag{4.4}$$

We solve the nematic equations in equilibrium, which are

$$(A + C\mathrm{Tr}\mathbf{Q}^2)Q_{\alpha\beta}(\mathbf{x},t) + B\,\overline{Q^2_{\alpha\beta}(\mathbf{x},t)} = L_1\nabla^2 Q_{\alpha\beta}(\mathbf{x},t) + L_2\,\overline{\nabla_\alpha(\nabla_\gamma Q_{\beta\gamma}(\mathbf{x},t))}\,. \tag{4.5}$$

These results from the condition $\delta\mathcal{F}/\delta Q = 0$ constrained to the condition of vanishing trace and symmetry of $\mathbf{Q}$. We employ the change in basis $\mathbf{Q} \to \mathbf{T}$ as defined in Eq.(1.13), so that the variational equations take the form,

$$(A + C\mathrm{Tr}\mathbf{Q}^2)a_i + BT^i_{\alpha\beta}\,\overline{Q^2_{\alpha\beta}} = L_1\nabla^2 a_i + L_2\,\overline{T^i_{\alpha\beta}T^j_{\beta\gamma}\partial_\alpha\partial_\gamma a_j}\,. \tag{4.6}$$

The complete set of equations with the boundary conditions are displayed in Appendix B.

We solve this set of equations, employing proper boundary conditions (planar, homeotropic and oblique director anchoring) to study the problems discussed in the following sections. Anchoring of the director at the isotropic-nematic interface can also be imposed through an

Figure	A	B	C	E'	L_1	L_2	Γ	System size
4.1(b)	$B^2/27C$	-0.5	2.67	0	0.01	0	0.1	256^2
4.2	$B^2/27C$	-0.5	2.67	0	0.01	0	1/20	8×512
4.3	$B^2/27C$	-0.5	2.67	0	10^{-6}	36	50	2
4.4	$B^2/27C$	-0.5	2.67	0	10^{-6}	$[4, 90]$	50	2
4.5	$B^2/27C$	-0.5	2.67	0	10^{-6}	36	50	2
4.6	$B^2/27C$	-0.5	2.67	0	10^{-6}	-1	50	2
4.7	$B^2/35C$	-0.5	2.67	0	0.01	0	50	256^2

Table 4.1: Numerical parameters in the Landau-de Gennes theory used to construct the figures.

inclusion of a term proportional to $\varsigma Q_{\alpha\beta}\phi_\alpha\phi_\beta$ in the free energy functional, where ς represents the strength and $\phi_{\alpha;\beta}$ is a quenched field following the interface structure. However in this study, we impose the director anchoring from the degree of anisotropy in the elastic constants as shown in the subsequent sections. In the next section, we verify "de Gennes ansatz" in a particular limit of the GLdG theory. The next section is devoted for the discussion of the nature of I-N interface with planar anchoring of the nematic director at the nematic boundary. We discuss the effect of oblique anchoring of the nematic director in the subsequent section. The GLdG parameters used for the calculations are highlighted in Table 4.1.

4.2 Verification of de Gennes ansatz

We have verified the remarkable de Gennes ansatz through a direct numerical solution. In our numerical calculations, a strip of nematic interface is sandwiched between two isotropic domains with periodic boundary conditions. The system was allowed to relax to the minimum of the free energy. The parameters were chosen such that the width $w \gg \Delta z = 1$, ensuring that discretization errors were kept to a minimum.

The resulting profiles for the variation of S and T are shown in Fig.(4.2). The values obtained for T are consistent with de Gennes' assumption of vanishing biaxiality. The variation of S at each of the two isotropic-nematic interfaces were fitted, using the least-squares method, to the analytical profile, with the saturation value of the order S_c, the location of the interface z_0 and the interface width w as fitting parameters. As shown in the inset to Fig.(4.2), fitted values of w agree remarkably well with the analytic result for a range

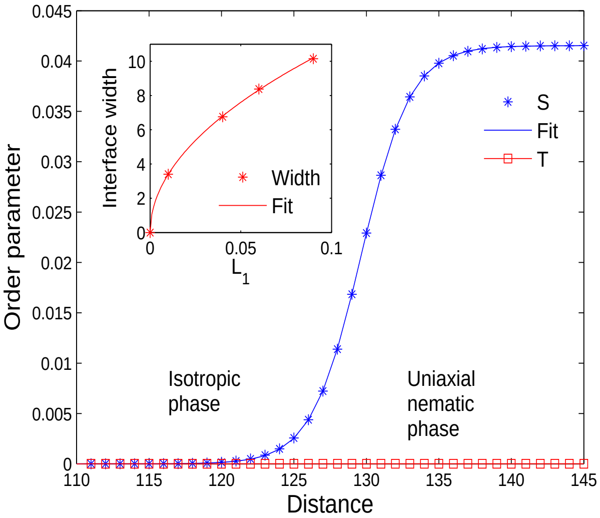

Figure 4.2: Variation of the degree of alignment (S) and biaxiality (T) across the nematic - isotropic interface with planar anchoring. Symbols represent numerical data, solid curves are the de Gennes ansatz (4.2). Nematic strip width = 256. The inset shows the variation of the interfacial width with the elastic constant L_1. The expected quadratic variation is accurately reproduced.

of parameter values. The agreement is accurate to within a fraction of a percent. Similar results were obtained for the saturation value of the order parameter. This benchmark also clearly demonstrates the accuracy of the MOL scheme in reproducing the equilibrium limit of Eq.(1.34).

The de Gennes ansatz also predicts that the energies of planar and homeotropic anchoring are identical when elasticity is isotropic ($L_2 = 0$). We compared the value of the free energies of the interface for both planar and homeotropic anchoring of the director. To machine precision, these answers are identical. Our results for this problem represent the first direct verification of the de Gennes ansatz retaining all degrees of freedom of the orientational tensor.

4.3 Isotropic-nematic interface with planar anchoring

To study the effect of different nematic director anchoring conditions to the I-N interface, we use the spectral collocation technique, described in the previous chapter, to solve the variational equations 4.6. The polynomial interpolant is constructed so as to satisfy Dirichlet boundary conditions. Though the physical problem is for an unbounded interval, our numerical approximation of a bounded interval gives excellent results since all variation in the order parameters is restricted to the region proximate to the interface. de Gennes in his calculation, based on energetic arguments showed that for $L_2 > 0$ planar anchoring was the stable interface conformation while homeotropic anchoring was the most probable

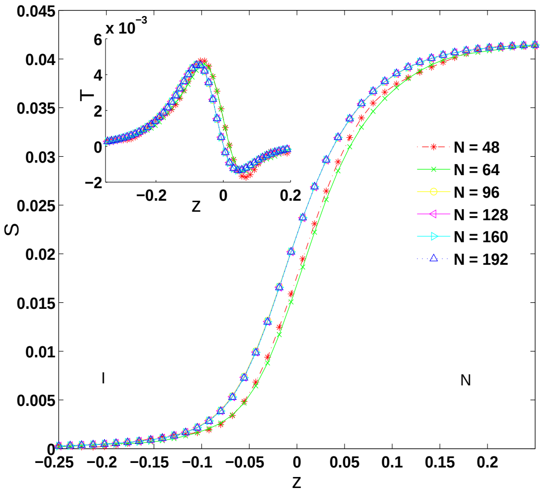

Figure 4.3: Convergence of the uniaxiality parameter S across the nematic-isotropic interface with planar anchoring. The inset shows the convergence of biaxiality parameter T. The convergence is achieved for the polynomials higher than $N = 96$, which is been shown as a single curve for $N = 128, 160$ and 192.

conformation for $L_2 < 0$.

4.3.1 Benchmarking the spectral collocation technique

To reduce the error to a minimum, we perform a systematic check of the nematodynamic equations with incorporating an increasing number of Chebyshev polynomials. We choose $L_1 = 10^{-6}$ in our numerics and obtain L_2 from our choice of κ. The spectral collocation reduces the nematodynamic differential equations (A.1) to non-linear algebraic equations. We solve them using a relaxation method from a well-chosen initial condition, relaxing till the differential change in successive iterations is less than 10^{-5}. Spectral convergence to machine accuracy is obtained by retaining 128 Chebyshev modes, as we have checked by an explicit calculation shown in Fig.(4.3). To compare with analytical and density functional results, the solution at the Chebyshev nodes is interpolated using barycentric interpolation (which is a spectrally accurate global polynomial interpolation) without compromising spectral accuracy.

4.3.2 Local biaxiality at the interface

The central results are depicted in Fig.(4.4). The analytical profile of the biaxiality T in the low $\kappa = L_2/L_1$ limit is due to Kamil *et al.* [35], which we plot together with the previous analytical profile due to PSW [57]. In Fig.[4.4(a)], in the main panel, we plot the biaxiality T for these two analytical approaches and our spectral data. The analytic form of T fits well to the spectral data, particularly away from the main peak, yielding essentially exact agreement deep into the isotropic and nematic sides. The PSW approximation overestimates the peak

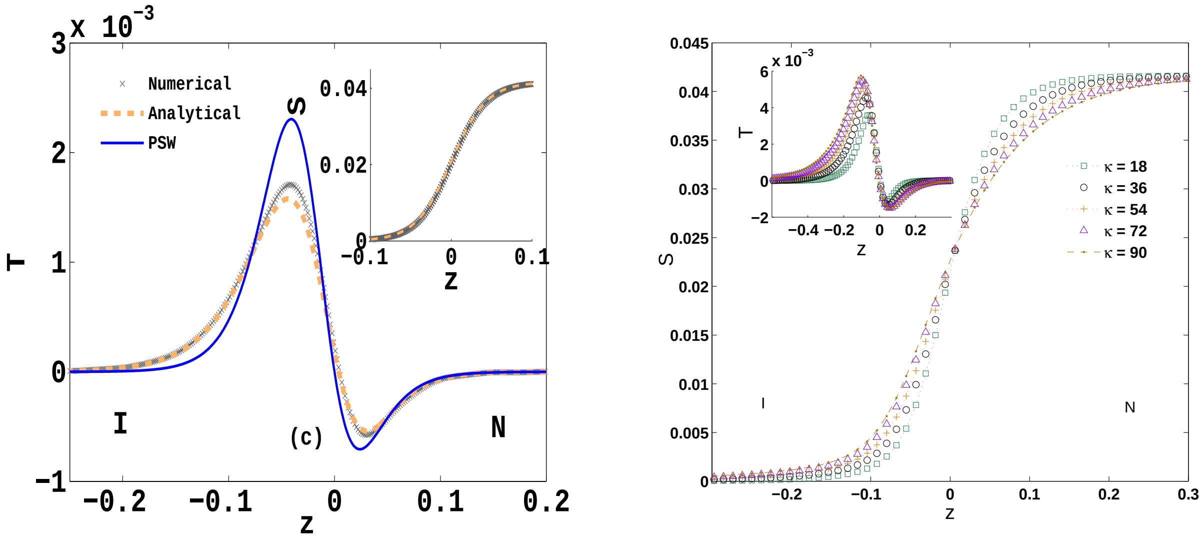

(a) $\kappa = 4$

(b)

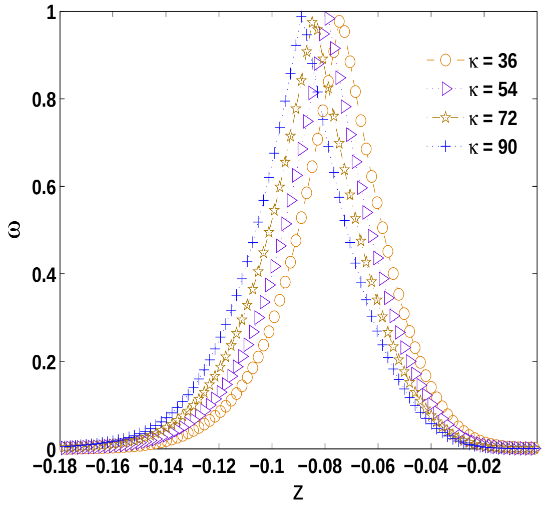

(c)

Figure 4.4: Uniaxial and biaxial profiles across the nematic - isotropic interface with planar anchoring. In (a) (main panel), a comparison of the T profile obtained from the analytical expression by Kamil *et al.*, PSW and our spectral data is plotted. The inset shows that of the uniaxial (S) profile for this case. In (b) (main panel), we show the uniaxial profile and the inset for the biaxial profile with increasing κ. In (c), we show the increasing biaxiality of the biaxial parameter ω, defined in Eq.(1.23) with κ.

value, and also differs sharply in relation to the numerical data deep into the isotropic side. The inset to Fig.[4.4(a)] shows the uniaxial (S) profile for this case. In Fig.[4.4(b)] we show the profile obtained with our method for S and T with increasing κ. Benchmarking this part is outside the scope of an analytical treatment.

4.4 The isotropic-nematic interface with oblique anchoring

Nematic ordering is strongly influenced by confining walls and surfaces, which impose a preferred orientation or "anchoring condition" on the nematic state. Such a preferred orientation yields an anchoring angle, defined as the angle made by the director in the immediate neighbourhood of the surface with the surface normal. Anchoring normal to the surface is termed as homoeotropic, whereas anchoring in the plane of the surface is termed as planar. The intermediate to this two cases is termed as oblique anchoring.

As is the case with surfaces, the interface between a nematic and its isotropic phase can also favour a particular anchoring. The problem of interface structure for the nematic is particularly interesting since it illustrates how the structure in the interfacial region can differ substantially from structure in the bulk. The previous section demonstrated that a region proximate to the interface could exhibit biaxiality within the LGdG theory, even if the stable nematic phase is purely uniaxial, provided planar anchoring is enforced at the nematic boundary. Such biaxiality is absent if the anchoring is homoeotropic [23]. These two limits, of homoeotropic and planar anchoring, lead to interface profiles of S and T which vary only in the vicinity of the interface, as well as orientations which are uniform across the interface [23].

An interesting question is whether an oblique nematic anchoring can be stable at the interface between a bulk uniaxial nematic and its isotropic phase within GLdG theory. Suppose we introduce boundary conditions that impose a specified oblique orientation asymptotically within the nematic phase, where the magnitude of the order parameter is saturated. The question, then, is whether such an imposed orientation is relaxed to a preferred value in the vicinity of the interface. The difficulties with this problem stem from the fact that changes in the local frame orientation on the nematic side of the interface come with an elastic cost arising out of nematic elasticity. This is an effect sensitive, in principle, to system dimensions, since gradients can be smoothed out by allowing the changes to occur over the system size. While this cost can be reduced by suppressing the order parameter amplitudes in regions where order parameter phases vary strongly, the precise way in which this might happen, if at all, is an open question.

PSW [57] studied this problem numerically within a GLdG approach, using a set of variables η_s and μ_s introduced by Sen and Sullivan in ref. [64]. These variables are combinations of the variables S, T and θ. Although the focus of their study was the emergence of biaxiality at the interface with a planar anchoring condition, PSW remarked that if the asymptotic orientation of the director in the nematic phase was set to any value other than 90° (planar anchoring) or 0 (homoeotropic anchoring) for large z, then η_s and μ_s approached this value with non-zero slope. PSW thus concluded that there could be no stable anchoring if the orientation of the director in the nematic phase was neither planar nor homoeotropic, but oblique. The precise nature of the resulting state obtained upon applying an oblique anchoring condition was not addressed by PSW [56, 57].

Density functional calculations on hard-rod systems using Onsager's theory applied to the free isotropic-nematic interface indicate that the minimum surface free energy is obtained when the rods lie parallel to the isotropic- nematic interface, the case of planar anchoring [47, 3]. Molecular simulations of a system of hard ellipsoids, in which an anchoring energy fixes the director orientation in the nematic phase at a variety of angles, indicate that the isotropic-nematic interface favours planar anchoring. These simulations, and a mean-field calculation based on the Onsager functional, find that the angle profile is approximately linear as one moves away from the boundary condition imposed by the wall at one end of the simulation box [76, 71]. These results, in particular concerning the stability of planar anchoring, are consistent with those from other treatments [7, 19, 18, 2, 72].

However, several other papers indicate specific regimes in which homoeotropic or oblique anchoring may be stable. Moore and McMullen [52] numerically evaluate the inhomogeneous grand potential within a specific approximation scheme finding that planar anchoring is preferred at the interface for long spherocylinders, but oblique or homoeotropic anchoring may be an energetically favourable alternative for smaller aspect ratios. Holyst and Poniewierski study such hard spherocylinders in the Onsager limit, noting that oblique anchoring is favoured over a considerable range of aspect ratios [34]. Finally, experiments provide evidence for both oblique [28] and planar anchoring [41], with electrostatic effects possibly favouring oblique anchoring.

We study the isotropic-nematic interface within GLdG theory in the case where an oblique anchoring condition is imposed on the nematic state far from the location of the interface [36]. The analytical treatment to this problem is by Kamil *et.al* which is satisfactory in a limiting case of small κ [36]. For a flat interface, the components of $\mathbf{Q}$ can depend only on the coordinate perpendicular to the interface. We work at phase coexistence, imposing boundary conditions fixing the isotropic phase at $z = -\infty$ and the nematic phase at $z = \infty$. The components of $\mathbf{Q}$ as $z \to \infty$ are chosen so that S is fixed to its value at coexistence S_c, while the axis of the nematic is aligned along a specified (oblique) direction. The coexisting states are separated by an interface in which order parameters rise from zero on the isotropic side of the interface to saturated, non-zero values on the nematic side. Since the two free energy minimum states are degenerate in the bulk, the position of the interface is arbitrary and can be fixed, for concreteness, at $z = 0$ in the infinite system.

However, there are subtleties. Provided all components of $\mathbf{Q}$ vary substantially only in the neighbourhood of the interface, the interface can be located through several, largely equivalent criteria. However, if variations of $\mathbf{Q}$ are not confined to a region proximate to the interface but depend on the system size L irrespective of how large L is, the very isolation of an interface from the bulk is ill-defined. As indicated earlier, it is this situation which obtains in the case of oblique anchoring and the $L \to \infty$ limit must be taken with care.

We summarize the results of the study: A numerical minimization of the GLdG free energy which imposes a specific oblique anchoring condition on the system deep into the nematic while fixing the interface location at the origin shows that the elements of $\mathbf{Q}$ vary with space even far away from the interface, albeit slowly. Only in the limit of homoeotropic

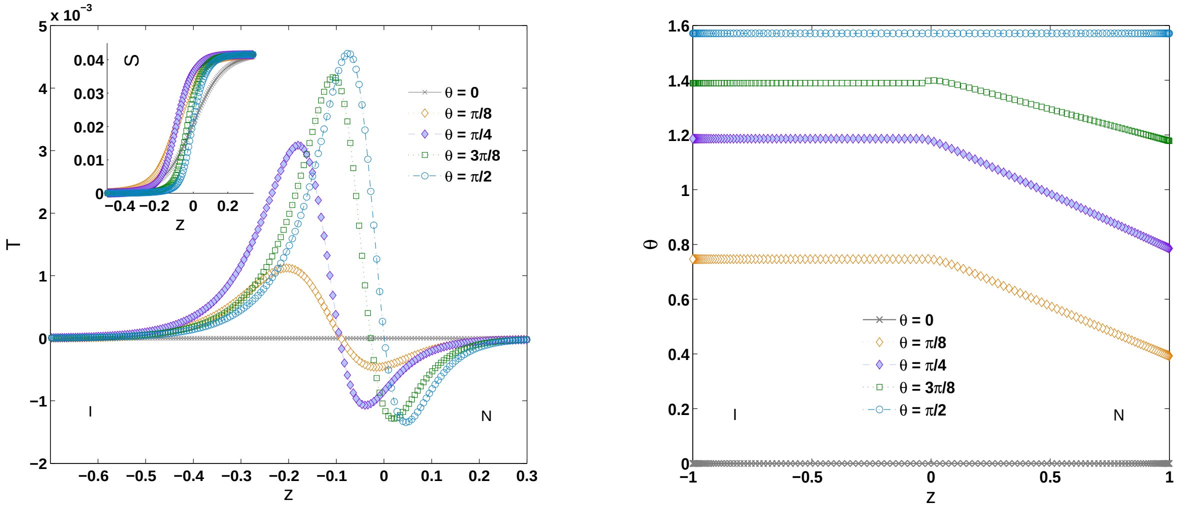

(a) $\kappa = 36$ (b) $\kappa = 36$

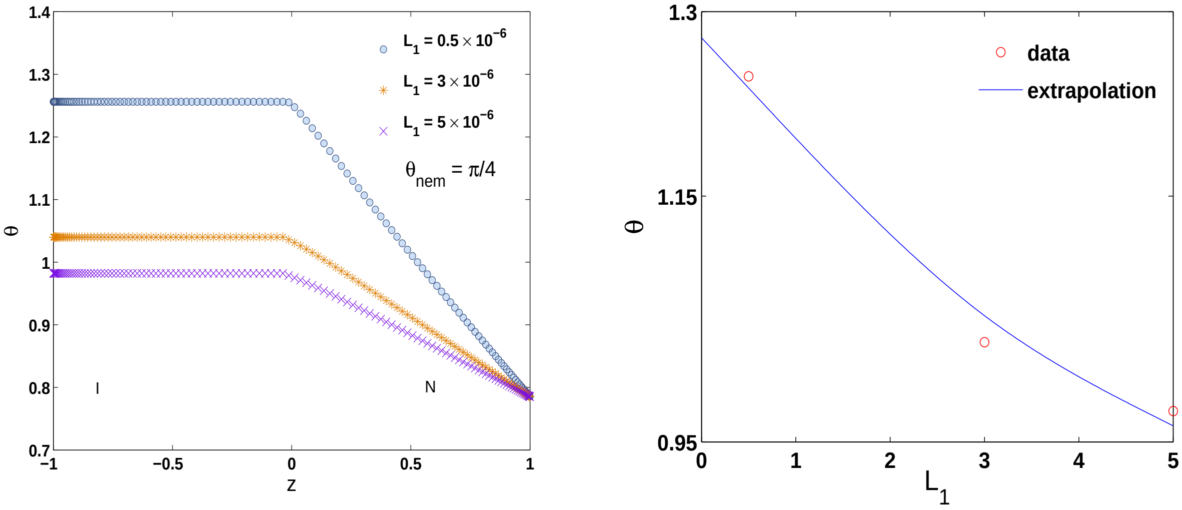

(c) $\kappa = 36$ (d) $\kappa = 36$

Figure 4.5: Panel (a) shows the variation of the uniaxial degree of alignment (S) and biaxiality (T) across the nematic - isotropic interface for oblique nematic anchoring. Panel (b) shows that of the local tilt angle θ. Panel (c) shows the variation of the local tilt angle across the interface for an oblique nematic anchoring fixed to $\theta = \pi/4$ at the nematic boundary. Panel (d) shows the variation of the local tilt angle with different values of the elastic constant and the extrapolation of the data to account for the system size $\to \infty$ or $L_1 \to 0$ limit. 128 Chebyshev polynomials are taken for the numerics.

or planar anchoring is the variation of $\mathbf{Q}$ confined to a finite region. This variation in the case of oblique anchoring can, however, be split into hydrodynamic and non-hydrodynamic components. Generically, the variation of the non-hydrodynamic components, such as the magnitudes of S and T, are confined to a finite region, independent of the system size L, if L is large enough. However, the orientation of the nematic director varies in space: if the asymptotic value of the nematic order parameter at L represents uniaxial ordering along an oblique axis, the director orientation interpolates linearly between either $\pi/2$ preferred at the location of the interface (planar anchoring) or 0 (homoeotropic anchoring), and the value imposed by the boundary condition at L. Whether planar or homeoetropic anchoring is preferred at the interface depends on the sign of the anisotropic elastic term, as initially shown by de Gennes [23].

Our results are broadly consistent with the qualitative observations of PSW, but provide a detailed quantitative analysis in the case of oblique anchoring. In the limit that $L \to \infty$, the total energy cost for elastic distortions of the nematic field $\sim \int (\nabla\theta)^2 dz \sim 1/L$, thus vanishing in the thermodynamic limit. Thus, the isotropic-nematic interface with an oblique anchoring constraint imposed on the nematic side can be regarded as being marginally stable, as opposed to unstable, provided the thermodynamic limit is taken with care.

4.4.1 Non-locality of the tilt angle with $\kappa > 0$

Stability imposes the requirement that $6 + \kappa > 0$ so that the tangential coherence length is a positive quantity. In this section we explore the consequences of a positive value of κ.

The results of our findings are summarized as follows: In Fig.[4.5(a)] we plot the S and T profile for the oblique anchoring angles $0, \pi/8, \pi/4, 3\pi/8$ and $\pi/2$. The T profile shifts origin as the anchoring is shifted from homeotropic to planar. This is also reflected in the profile of S shown in the inset. We also recover the vanishing biaxiality in the homeotropic anchoring case, as first obtained by de Gennes [23]. In Fig.[4.5(b)], we show the monotonic increase in the slope of the local tilt angle θ as the interface is approached from the nematic boundary and also the nematic anchoring is tilted from homeotropic ($\theta = 0$) to planar ($\theta = \pi/2$). As the director on the isotropic side of the interface is a undefined quantity, we plot θ with a straight line for ease. The slope vanishes only when the true thermodynamic limit $L \to \infty$ is achieved. The interface anchoring is smoothly approached from the anchored nematic boundary in a linear way. In Fig.[4.5(c)], for a fixed anchoring of the nematic director at the boundary as $\theta = \pi/4$, how the anchoring angle behaves at the interface as the elastic constant L_1 is decreased, which is effectively to increase the system size of the problem. Finally we show in Fig.[4.5(d)] the increment of the anchoring angle with the decrement of L_1. We mention that the system size is fixed from the boundary between [-1,1] and decrement of the elastic constant L_1 effectively increases the effective correlation length of the problem. In Fig.[4.5(d)] we also plot the polynomial extrapolation of the data that reflects the director anchoring at the $L \to \infty$ limit of the problem, i.e. the $L_1 \to 0$. However the extrapolation is affected severely with only a few points and thus yields a value of $\theta < \pi/2$.

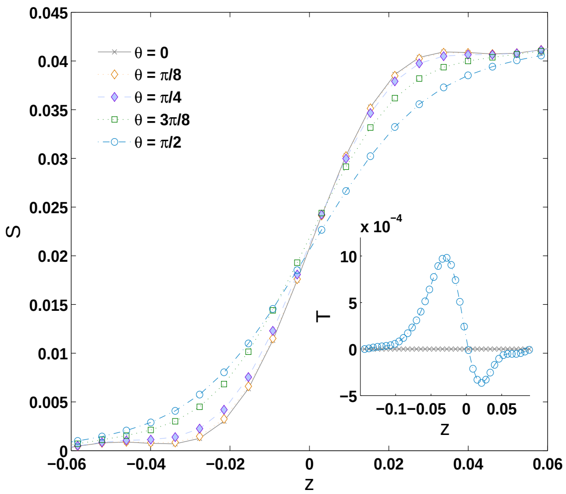

Figure 4.6: Variation of the uniaxial degree of alignment (S) and biaxiality (T) across the nematic - isotropic interface for oblique nematic anchoring. Number of Chebyshev polynomials is $N = 128$

4.4.2 Non-locality of the tilt angle with $\kappa < 0$

In this section we explore the consequences of a negative value for L_2. We find in Fig.[4.6(a)] that, consistent with prediction of de Gennes, a negative κ consistent with stability favours *homoeotropic* anchoring at the interface, in contrast to the case of positive κ. There appears to be no significant difference in the profiles of S and T[1]. In Fig.[4.6(b)] we demonstrate the monotonic decrease in the slope of the local tilt angle θ as the interface is approached from the nematic boundary and also as the nematic anchoring is tilted from homeotropic ($\theta = 0$) to planar ($\theta = \pi/2$). As there is no notion of director in the isotropic side of the interface, we plot θ with a straight line as in the previous subsection. The slope vanishes only when the true thermodynamic limit $L \to \infty$ is achieved, otherwise the interface anchoring is smoothly approached from the anchored nematic boundary.

4.5 Fluctuation of the I-N interface

The nature of the isotropic-nematic phase in the presence of thermal fluctuation has only been previously addressed using molecular dynamics simulations [62]. So far to our knowledge, the nature of the interface described from a fluctuating Ginzburg-Landau theory is not previously addressed.

We perform our numerics with a nematic strip of size 128 sandwiched between isotropic phases with periodic boundaries on a 256^2 lattice. At coexistence, defined in the absence of fluctuations, we see a successive collapse of the uniaxial nematic phase with a local melting of

---

[1] We show the T profile for only planar and homeotropic anchoring due to non-convergence of the profiles in the computational time for intermediate anchoring angles.

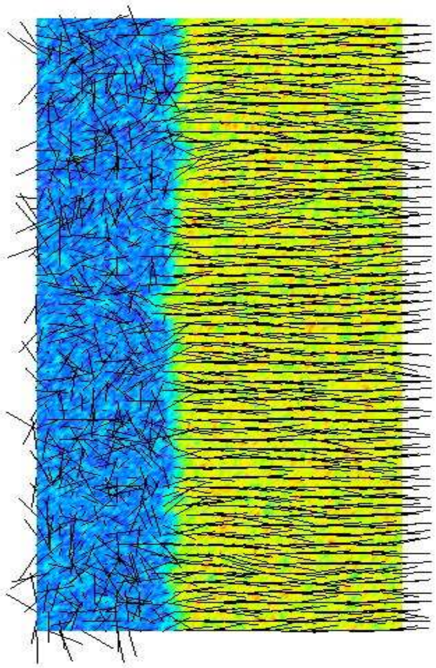

Figure 4.7: Effect of the thermal fluctuation on the metastable I-N interface, computed at mean-field coexistence with planar anchoring. The temperature is set at $k_B T = 1.2988 \times 10^{-6}$.

the interface after certain period in time. Slightly below coexistence, we see an expansion of the fluctuating interface without melting of the interface which finally excludes the isotropic fluid phase completely.

In Fig.(4.7), we exhibit the calculated interface at time $t = 6 \times 10^3$, with the isotropic phase in the left and the nematic phase on the right. Only one side of the interface is shown. Colours indicate the values of the order parameter, with zero on the left (blue colour) and nematic saturation values on the right (yellow colour). The local orientation field is also shown, indicating alignment in the nematic state perpendicular to the interface. The roughening of the interface by noise-induced capillary excitations, an effect absent in the conventional mean field, zero noise treatment of this problem can be clearly seen. The capillary fluctuations add to the interface width computed within a mean-field treatment of the GLdG functional. They also modify the surface tension in nontrivial ways [62].

4.6 Conclusion

In this chapter we have discussed the conformation of the isotropic-uniaxial nematic interface with different anchoring conditions imposed on the director, in the presence and in the absence of elastic anisotropy terms. We obtain the profile of the nematic orientation tensor at the interface as well as in the bulk. We show in the limit $\kappa = 0$, de Gennes ansatz for uniaxial interface is valid. In the limit $\kappa \neq 0$, the interface become biaxial, with planar anchoring of the nematic director at the nematic boundary. We the showed how oblique nematic anchoring breaks the local property of the interface, with a smooth profile of the tilt angle far from the interface. Finally, we demonstrate the effect of thermal fluctuation on the roughness of the interface profile.

Chapter 5

Diffusive scaling and defect morphology in the spinodal kinetics of nematics

This chapter discusses topological defects in uniaxial and biaxial nematic liquid crystals in two and three dimensions. We suggest a novel way to identify and visualize such defects, which relies on the non-trivial variation of the *amplitude* of the order parameter at the defect core with respect to its bulk value. Our visualization methods provide insights into the intercommutation of defects in uniaxial and biaxial systems. We also resolve a controversy concerning the growth exponent in coarsening nematics, using large-scale simulations to access the asymptotic scaling regime.

We begin with a discussion of defect classes predicted by homotopy theory. We discuss the phase ordering of uniaxial nematics in two dimensions, describing how the visualization technique developed and discussed in Chapter 3 can be applied to locate defects in a far more transparent way than currently popular methodologies. We then discuss dynamical scaling laws and growth exponents at different stages of the kinetics. We discuss the core structure of point defects in the uniaxial phase. We describe how string defects in three dimensions may be visualized. We observe defect intercommutation events in our simulations of the coarsening uniaxial nematic. Our visualization methods enable us to describe in some detail the variation of the order parameter structure across such intercommutation events, including the variation of uniaxial and biaxial order parameters across the overlap region. We conclude our study of uniaxial nematics with a discussion of the effects of thermal fluctuations.

We then repeat these studies in the case of phase ordering in biaxial nematic phases. In contrast to predictions of defect entanglement from a group theoretical analysis, we see no such entanglement in our simulations. We discuss the structure of the core in two classes of stable defects in biaxial systems. Finally, we settle an old controversy concerning the observation of *non-universal* exponents in spinodal decomposition in biaxial nematics, observing that these observations are as a consequence of a long cross over to ultimately diffusive i.e. $L(t) \sim t^{1/2}$ behavior.

5.1 Introduction

Nematic systems, as a consequence of a broken continuous symmetry, exhibit fascinating topological defects and complex defect interactions [24]. Their study constitutes a challenging ground for theories, whether of phase ordering kinetics [12, 77], of homotopy theory [49] or the Kibble mechanism in cosmology [37, 21].

A brief summary of prior work on phase ordering in uniaxial and biaxial systems is the following: Zapotocky, Goldbart and Goldenfeld studied the coarsening of both uniaxial and biaxial systems in two dimensions (the order parameter space is three-dimensional whereas the spatial dimension is two dimensional), using a cell-dynamical scheme (CDS) [77]. They found that, for uniaxial nematics: (a) the growing correlation length characterizing the sizes of domains increases as a power law in time with $L(t) \sim t^{\phi_{cor}}$, with $\phi_{cor} \simeq 0.40$. In contrast, (b) the length scale characterizing the separation of topological defects increases with time as $L_{def}(t) \sim t^{\phi_{def}}$, with $\phi_{def} \simeq 0.374$. The discrepancy between these growing length scales was interpreted as a break-down of dynamical scaling. Also,(c) these exponents, in addition to the exponent describing the decay of the energy density are very different from 0.5, the value predicted by naive scaling. For biaxial nematic systems, these authors find an exponent $\phi_{cor} \simeq 0.39$, as well as a discrepancy between the scaling exponents for growth as well as for the defect separation, suggesting that dynamical scaling may break down here as well.

Bray, Puri, Blundell and Somoza study spinodal decomposition in quenched uniaxial nematics, finding a growth exponent $\phi_{cor} \simeq 0.45$ and a good fit to $S(k)$ at large k of $S(k) \sim 1/k^5$, i.e. indicating a Porod exponent of 5 [14]. These authors also comment on the discrepancy between the 0.45 they obtain in numerics and the expected 0.5, noting that they cannot say whether this indicates a real discrepancy or whether the data are not yet in the right asymptotic regime. These authors use a methodology in which, as in the CDS simulations, amplitude fluctuations are ignored.

Priezjev and Pelcovits have studied the dynamics of two and three-dimensional biaxial nematic crystals using a Langevin dynamics for the orientation of the frame constituted by the eigenvectors of the order parameter tensor, in an effort to understand the effects of the complex defect structures in these systems [58]. Again, these simulations assume that amplitude order is saturated. Previous work by Kobdaj and Thomas provided a justification for the observation of Zapotocky *et al.* of the dominance of only two types of topological defects (both corresponding to half-integer charge) at late times, by showing that, within the one-constant approximation, one class of half-integer defects is always unstable to the other class [39]. Priezjev and Pelcovits point out that the relative values of the elastic constants, beyond the one-constant approximation, can yield rich coarsening behaviour, including the formation of junction points where defect lines meet. Priezjev and Pelcovits observe no line crossings or entanglements in their coarsening sequences.

Analytically, calculations of defect structure and properties in biaxial nematics are complex because of the underlying tensorial form of the order parameter and a sixth order nonlinear term in the free energy functional. The order parameter dynamics is governed through a set of coupled nonlinear PDE characterizing the five independent components of the tensor [10]. Numerically, finding defect-antidefect pairs is hard although not impossible, although complicated algorithms must be used to visualize tensorial data through the extensively used techniques of Müller and Westin metrics [8, 15]. On the other hand, lattice algorithms are computationally expensive because topological circuits must be constructed at each node of the lattice and the angular variation in the director and co-director performed along these circuits to identify and classify the defects. Such algorithms for tracking defects from all different classes arising in a bulk nematic system have been reported [77, 69]. An operator method for counting defect line segments is also reported [40].

Topological defects represent a non-continuity of the order parameter along regions of reduced dimensionality. At such defects, the direction of ordering is ill-defined. Such defects can be points in two dimensions and lines in three dimensions. A topologically stable defect cannot be eliminated through a continuous transformation of the order parameter. A defect is assigned an invariant quantity, the topological charge. The classification of defects lie in the map of the order parameter from physical space to a geometrical space $\mathcal{R}$ and defining the homotopy group $\pi_i(\mathcal{R})$ where $i = d_{sp} - d_{def} - 1$; d_{sp}, d_{def} are the physical and the defect dimension of the problem.

The uniaxial nematic order parameter is invariant under a local transformation $\mathbf{n} \rightarrow -\mathbf{n}$. Thus, the order parameter space is a sphere with antipodal points identified, termed as $\mathbb{S}^2/\mathbb{Z}_2$ [1] or more generically the projective plane $\mathcal{RP}_2$. In $\mathcal{R}$, the circular contours, which can be contracted to a point, correspond to the topologically unstable disclinations of integer strength, as this can be eliminated from the system by making the director *escape in the third dimension*, as in the case of an uniaxial nematic phase. The contours terminating at the antipodal points correspond to the stable class of half integer charge defects. As the contours corresponding to $+1/2$ defects can be continuously transformed to that of $-1/2$ defects, there is only one topologically stable class of defect. The order parameter space is identified as the first homotopy group $\pi_1(\mathcal{RP}_2)$ which is the two element group $\mathbb{Z}_2$. The conservation laws of topological charge are $1/2 + 0 = 1/2$ and $1/2 + 1/2 = 0$ respectively.

The biaxial nematic order parameter is invariant under a local transformation of the triad $\mathbf{n} \equiv -\mathbf{n}, \mathbf{l} \equiv -\mathbf{l}$ and $\mathbf{m} \equiv -\mathbf{m}$. The order parameter space is the group of full rotations of the triad with the antipodal points identified, termed as $\mathbb{S}^3/\mathbb{D}_2$[2] or more generically the projective plane $\mathcal{RP}^3$. The first homotopy group of the order parameter is identified as the non-Abelian eight-element group under multiplication of quaternions $\mathbb{Q}$, whose elements are represented with $\{\mathbb{I}, -\mathbb{I}, \sigma, -\sigma\}$ where $\mathbb{I}$ and σ denote the identity and Pauli matrices. The elements of the group form five conjugacy classes, $C_0 = \{\mathbb{I}\}$, $\bar{C}_0 = \{-\mathbb{I}\}$, $C_x = \{i\sigma_x, -i\sigma_x\}$, $C_y = \{i\sigma_y, -i\sigma_y\}$ and $C_z = \{i\sigma_z, -i\sigma_z\}$ respectively.

There are a total of five stable class of defects corresponding to these conjugacy classes. C_x, C_y and C_z class correspond to a π rotation of the director about the defect core representing to a half integer charge defect whereas $\bar{C}_0$ correspond to 2π rotation so as a stable integer charge defect, which cannot be removed by a continuous transformation unlike the uniaxial nematic phase. The topologically unstable (or trivial) class correspond to a 4π

---

[1] Sphere $\mathbb{S}^2 = \mathcal{SO}(3)/\mathcal{SO}(2)$ is the factorization of $\mathcal{SO}(3)$ with $\mathcal{SO}(2)$. $\mathbb{S}^2$ is again factored out with $\mathbb{Z}_2$, which consist of two elements 0 and 1.

[2] $\mathbb{S}^3$ is the three dimensional sphere in four dimensions. It is factored by the four element Dihedral group $\mathbb{D}_2$.

Figure	A	B	C	E'	L_1	κ	Γ	k_BT	System size
5.1-5.2	-0.08	-0.5	2.67	0	1.0	0	1/10	0	256^2
5.3	-0.1	-0.5	2.67	0	1.0	0	1/20	0	256^2
5.4	-0.025	-0.5	2.67	0	0.1	0	1/20	0	256^2
5.5-5.7	-0.008	-0.5	2.67	0	0.12	0	1	0	128^3
5.8	-0.1	-0.5	2.67	0	1.0	0	1/10	10^{-4}	256^2
5.9-5.12	-4.5	-0.5	2.67	3.56	17.0	0	1/50	0	512^2
5.13-5.14	-1	-0.25	1.0	1.0	10	0	1/100	0	128^3

Table 5.1: Numerical parameters in the Landau-de Gennes theory used for the computer experiments in spinodal kinetics presented in this chapter.

rotation of the director. The pairing and breaking of defects depend on the multiplication rule specific to a particular conjugacy class and also on the energetics. Multiplication to the same class yields either a trivial class C_0 or $\bar{C}_0$, but this joining-up strongly depends on the path of joining with other defects from other classes, because of the non-Abelian nature of the group $\mathbb{Q}$ [49].

We suggest a simple algorithm to locate all classes of defects, thus simplifying such calculations considerably. We propose that the calculation of the uniaxial and biaxial degree of alignment $S(\mathbf{x}, t)$ and $T(\mathbf{x}, t)$ suffices to locate the defect pair from all the classes. At the core of the defect, these scalar quantities differ from their equilibrium values in the uniform state. The topological charges are found from Schlieren textures, which represent the intensity of the transmitted light through a nematic film sandwiched between crossed polarizers. As the isotropic phase coarsens into the nematic phase, both integer and half integer charged defects are found at an early stage of the dynamics, whereas at the late stage only half integer charges are stable. These defect-antidefect pairs coalesce and disappear from the system, resulting in an equilibrium defect-free nematic phase [77, 20]. Our defect finding technique clearly locates the stream-tubes in three dimensions following a quench into the nematic phase.

Such a methodology cannot be implemented in approaches where order parameter amplitudes are assumed to be *a priori* saturated, as in the frame-based methods of Priezjev and Pelcovits. In contrast to the CDS methods, which replace the equations of motion by an equivalent discrete map, the full equations of motion are solved here, permitting access to the detailed structure of the core in both uniaxial and biaxial nematics.

The first two sections of this chapter are devoted to the description of the phase ordering

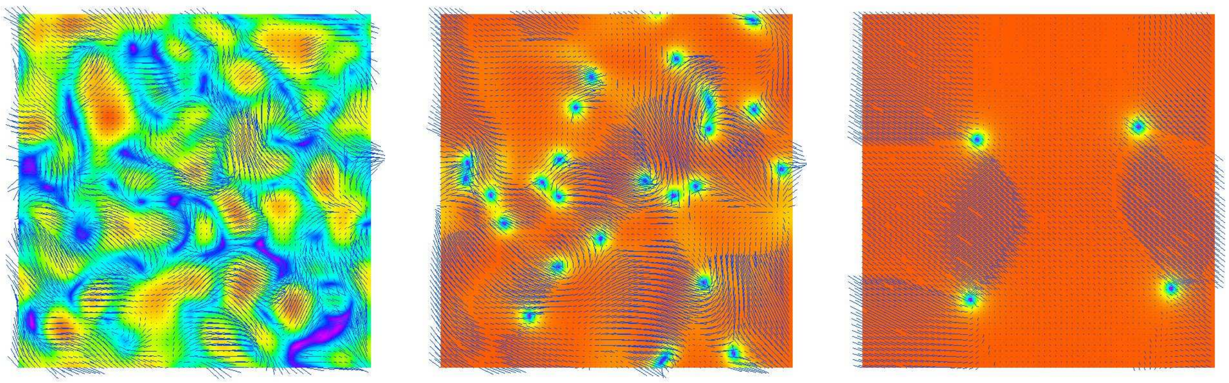

(a) $t = 700$ (b) $t = 2 \times 10^3$ (c) $t = 6 \times 10^4$

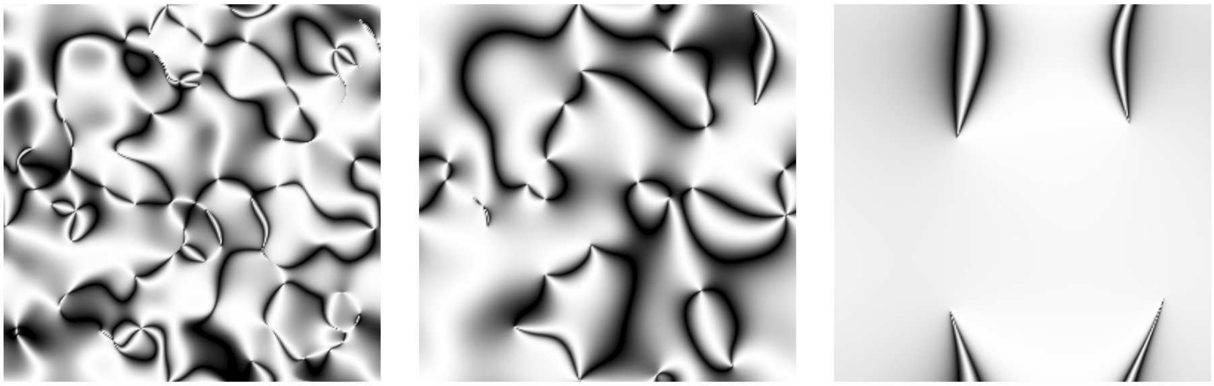

(d) $t = 700$ (e) $t = 2 \times 10^3$ (f) $t = 6 \times 10^4$

Figure 5.1: Uniaxial degree of alignment S and the nematic director field $\mathbf{n}$ on top of that and the corresponding Schlieren textures in a coarsening nematic from the isotropic phase. Topological defects of integer and half - integer charge are clearly observed, as seen in the coloured frames of S in (a)-(c) and the textures in (d)-(f). (a) Shows the formation of defects with coalesce of domains after quench from a random configuration. (c) and (f) show the defects at an early and late stage of the dynamics. The integration is performed over 6×10^4 MOL steps with unit step length.

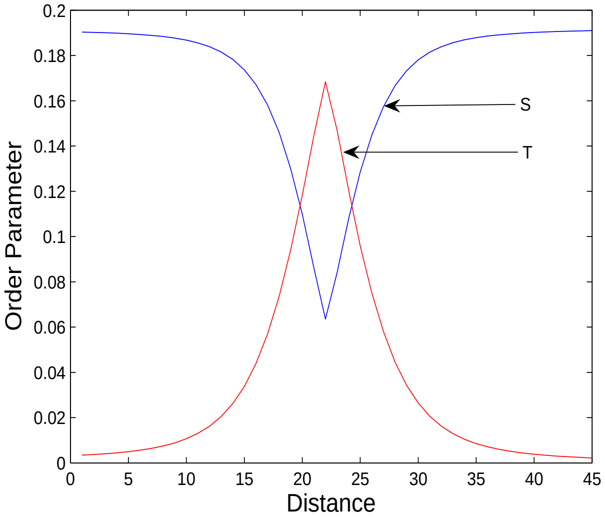

Figure 5.2: The variation of the uniaxial and biaxial order parameter along a line passing through the defect core in uniaxial quench. Note the presence of strong biaxiality within the defect core as seen previously [63]. The sharpness of the variation at the core reflects the coarseness of our discretization and would be smoothed out by a finer discretization.

in uniaxial and biaxial nematic phases, defect core structures and dynamical scaling in different stages of the kinetics. In the last section, we describe the defect dynamics in the presence of thermal fluctuations. The GLdG parameters used for the calculations are highlighted in Table 5.1.

5.2 Phase ordering in uniaxial nematics

5.2.1 Point defects : core structure and dynamics

For a quench below the spinodal temperature, the isotropic phase becomes locally unstable to a nematic perturbation and the system proceeds spontaneously to the nematic phase through spinodal kinetics. Coherent regions of local nematic order develop in time, with a distinct axis of order in each of these domains. Topological defects form at the intersections of these differently ordered domains. Coarsening proceeds through the annihilation of topological defects, increasing the correlation length of local orientational order. In two dimensions[3], the defects are points while line defects appear in three dimensions.

To study coarsening kinetics, we start from a random initial configuration where we draw the order parameters S and T randomly from a normal distribution with zero mean and variance proportional to F_c, ensuring the condition, $0 < T < S$. We obtain $\cos\theta$ from an uniform distribution between -1 and 1, and choose ϕ similarly between 0 and 2π to gen-

---

[3] In a 2D nematic film, the space variations are only in 2 Cartesian directions, while the spin dimension is retained to 3 i.e. all of the Cartesian directions accessible by the director to orient.

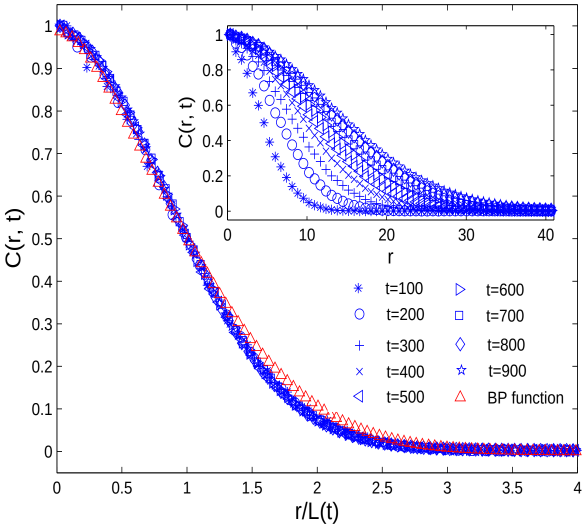

Figure 5.3: Data collapse of the direct correlation function $C(r)$ with scaled distance $r/L(t)$ for different times. The symbol Δ depicts the Bray - Puri function [13] for the O(2) vector model : $f_{BP}(x) = B^2(0.5, 1.5)F[0.5, 0.5, 2; \exp(-x^2)] \exp(-x^2/2)/\pi$. The inset shows the unscaled correlation function at different times.

erate the director and codirector. The joint normal is obtained through the Gram-Schmidt orthogonalization technique. We then relax the system from this initial isotropic state at a temperature below the supercooling spinodal temperature. The data presented below is averaged over 10^2 different initial conditions for a 256^2 system with periodic boundary conditions. From the coarsening simulations we obtain the strength of uniaxial and biaxial order S and T, and the director $\mathbf{n}$. Fig.[5.1(a-c)] shows S in false colours with $\mathbf{n}$ embedded on top of that. The director is used to construct the schlieren plots shown in Fig.[5.1(d-f)]. These plots are constructed by first projecting the director into the $x - y$ plane, finding the angle χ made by this projection with an arbitrary axis (say x-axis) and then computing $\sin^2(2\chi)$. The presence of both integer and half-integer defects is clearly visible in these plots as the meeting points of four and two dark brushes, respectively. In the corresponding plots for the strength of ordering, the defects are clearly visible as localized regions where S rapidly decreases. This is the core region of the topological defect, shown in Fig.(5.2). We confirm the surprising finding that there is strong biaxial ordering inside the defect core [63]. These results are in perfect qualitative agreement with both theoretical predictions and previous numerical results [63].

5.2.2 Dynamical scaling in two dimensions

To make a quantitative comparison with previous work, we compare results for the time-development of correlation functions during coarsening. Theoretical predictions and analytical work have verified that the correlation functions defined in Eq.(2.9-2.10) have a scaling

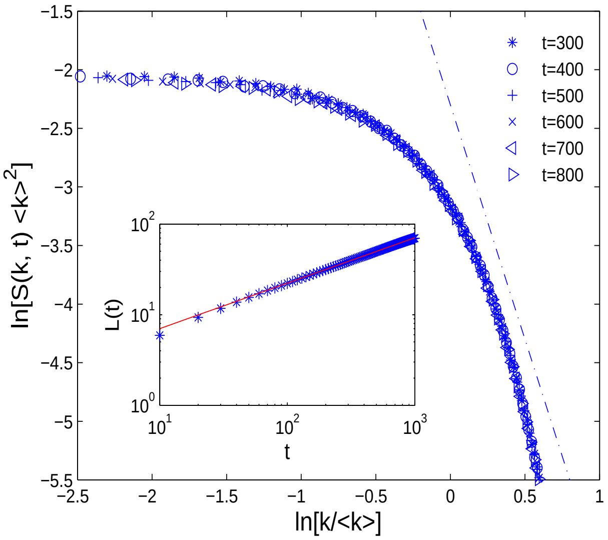

Figure 5.4: Data collapse of the structure function $S(k,t)$ at different times. The dash-dot line has a slope of -4 indicating the validity of generalized Porod's law for O(n) vector systems, with $n = d = 2$. The departure from Porod's law at high k is due to amplitude variation across the finite core size of the defects as discussed in the text. The inset shows the time dependence of the correlation length L(t). The length grows as a power law with an exponent of 0.5. The maximum value of the correlation length is approximately 1/4-th the system size, ensuring the absence of finite-size artefacts.

form $C(r,t) = \mathcal{F}[r/L(t)]$, and $S(k,t) = L^d(t)\mathcal{G}[kL(t)]$ [12]. Here, $C(r,t) = \sum_{|\mathbf{r}|=r} C(\mathbf{r},t)$ and $S(k,t) = \sum_{|\mathbf{k}|=k} S(\mathbf{k},t)$ are angular averages of the correlation functions in real and Fourier space respectively. The length $L(t)$ is extracted from the real-space correlation function using the implicit condition $C(r = L(t),t) = 1/2$. In Fig.(5.3) we confirm that the real-space correlation function does indeed scale as expected.

Our numerical data for the scaling function are in close agreement with an analytical calculation for a two-component *vector* model due to Bray and Puri [13], although the symmetry of this model is not the same as the tensorial symmetry of the nematic problem. A similar comparison has been made in [26]. In Fig.(5.4) we show the corresponding scaling of the Fourier space correlation function. The wavenumber $\langle k\rangle$ is the root of the second moment of the $S(\mathbf{k},t)$ defined by

$$\langle k\rangle^2 = L(t)^{-2} = \frac{\sum_{\mathbf{k}} k^2 S(\mathbf{k},t)}{\sum_{\mathbf{k}} S(\mathbf{k},t)}. \tag{5.1}$$

The inset of Fig.(5.4) shows the growth of the length scale as a function of time. Theoretically, this is expected to grow as a power $L(t) \sim t^{\alpha}$. Our estimate for this exponent is $\alpha = 0.5 \pm 0.005$. Our results are consistent with both analytical predictions and an earlier numerical simulation. The Fourier space correlation function is expected to exhibit a short-wavelength scaling $S(k,t) \sim k^{-4}$, known as a generalized Porod law [12]. We see a clear range of

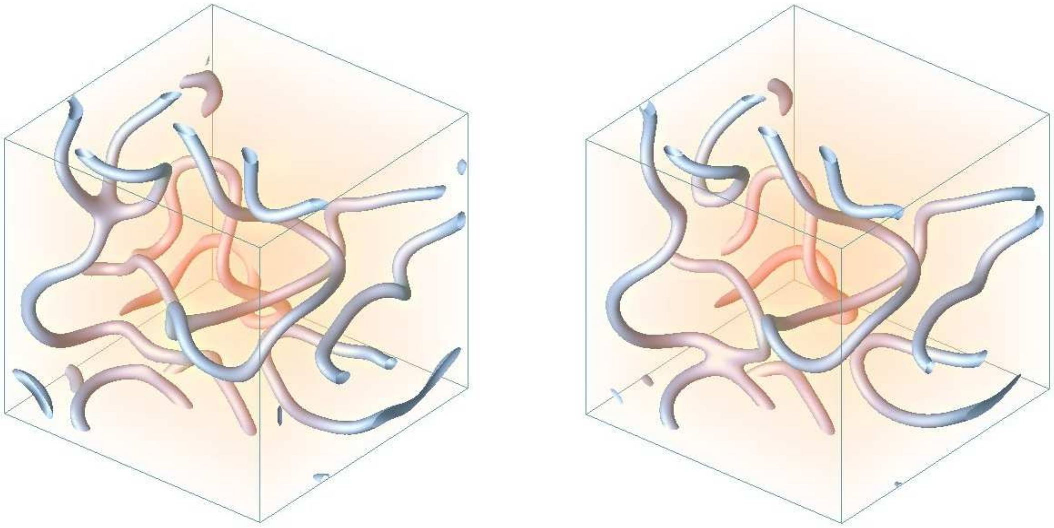

(a) $t = 1200$ (b) $t = 1600$

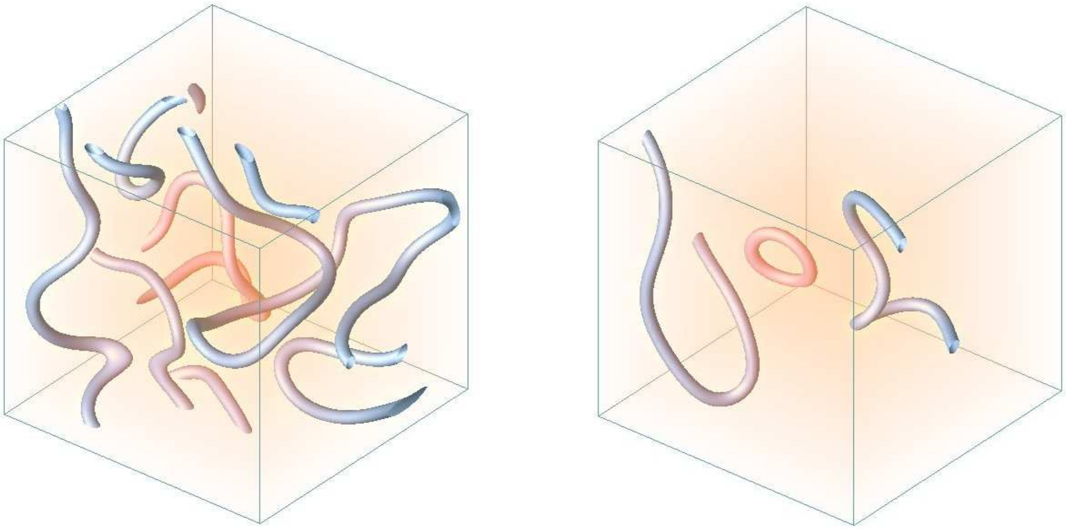

(c) $t = 1800$ (d) $t = 4400$

Figure 5.5: Time evolution of uniaxial degree of alignment [frames 5.5(a)-5.5(d)] in a coarsening 3D uniaxial nematic, plotted at an isosurface value 0.054 and volume rendered in false colours.

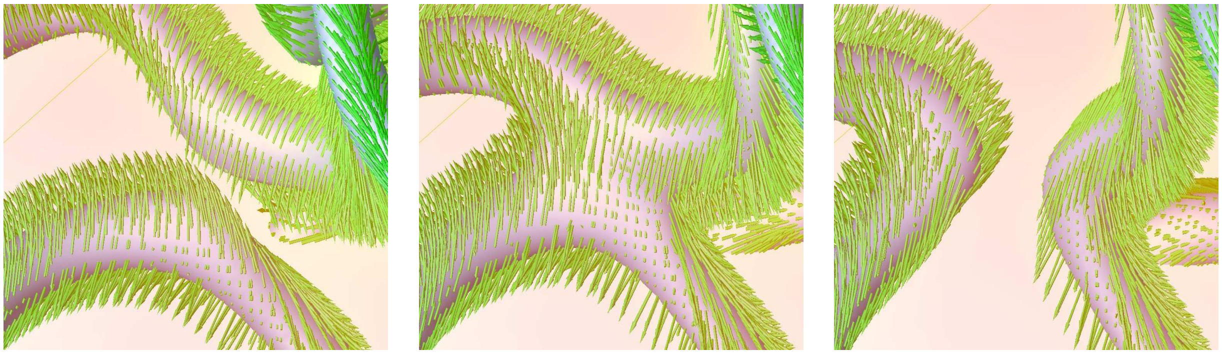

(a) $t = 1200$ (b) $t = 1600$ (c) $t = 1800$

Figure 5.6: The uniaxial degree S and the director **n** on the surface of the stream tube of S, plotted on false colours.

wavenumbers where Porod scaling is obtained. At very short wavelengths, corresponding to the size of the defect core where order parameter amplitude variations are important, such Porod scaling should breaks down. We see evidence for this as well, where the very highest wavenumbers in Fig.(5.4) corresponding to the size less than the size of a defect core show deviations from the Porod scaling. Our numerical results for spinodal decomposition, then, agree both qualitatively and quantitatively with theoretical results and previous numerical work [25].

5.2.3 Intercommutation, loop formation of line defects in three dimensions

Defects in two dimension are points, while they can be linear in one higher dimension. A uniaxial nematic phase in two dimensions coarsens through successive production and annihilation of point defect-antidefect pairs. In three dimensions, a coarsening nematic proceeds through the initial creation of line defect-antidefect pairs. The pair annihilates by inter-commutation of the line segments to form a closed loop. Different loops pass through each other to form distinct loops which finally contract and eventually disappear from the system in the late stage of the kinetics.

Fig.(5.5) shows the corresponding uniaxial scalar field S at successive time steps after a uniaxial nematic quench from isotropic phase. An inter-commutation of line disclination is clearly noticeable, which can be seen in the south-west corner of the first three frames [5.5(a)-5.5(c)]. Last frame [5.5(d)] shows a loop formed at a late stage of the phase ordering kinetics where only a few defects exist. Superimposed with the scalar field S, change of the director field conformation on the surface of the stream tubes of S is shown in Fig.[5.6(a)-5.6(c)] while an inter-commutation event of defect line segments take place.

In Fig.(5.7), we show the data collapse of the structure function as well as the uncollapsed data in the inset. However, accurate estimations of the growth exponent have not been carried out due to lack of sufficient data for statistical averages to be meaningful.

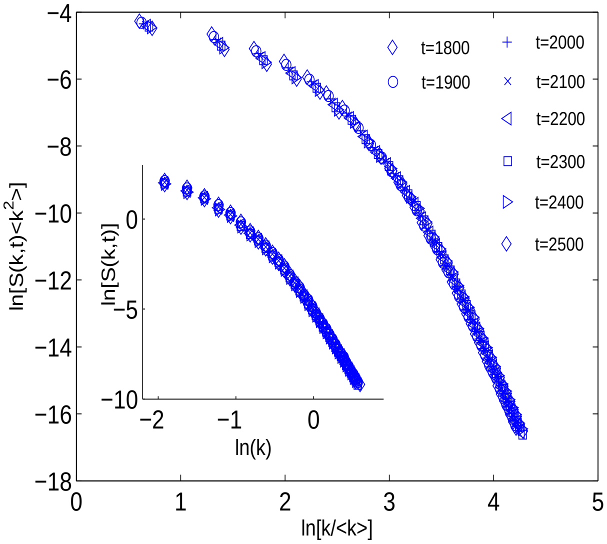

Figure 5.7: The data collapse of the scaled structure function with the scaled Fourier modes at different times is plotted. The inset depicts the behaviour of the unscaled correlator $S(k,t)$ with unscaled Fourier modes k at those times shown in the main figure.

5.3 Fluctuating defect kinetics

The dynamics of defects is greatly influenced by the presence of fluctuating thermal forces. To illustrate the role of fluctuations, we calculate the time evolution of the number density of defects. This is achieved through calculating the number of field values below a certain threshold value at a particular instant of time. For our numerics we set this value to be half the value of the maximum attainable value of the field for each and every instant in time.

We calculate the total number of defects at a particular time defined as

$$N_d(t) = \int \rho(\mathbf{x}, t) dx \tag{5.2}$$

where, $\rho(\mathbf{x}, t) = \sum_i q_i \delta^d(\mathbf{x} - \mathbf{x}_i)$ is the defect density, q^i is the winding number of the topological defect at the i^{th} space point.

Fig.(5.8) shows the variation of the defect density with time in the presence and absence of fluctuation. The initial slope in both the cases correspond to the early time diffusive scaling regime while the degree of uniaxiality saturates to their equilibrium values. In the presence of thermal fluctuation, the diffusive scaling regime is reduced in comparison to the non-fluctuating case. The fact that the slopes are equal in both cases suggests that the fluctuating force does not play any significant role in generating defect pairs, apart from speeding up the defect kinetics considerably. At the late stage of the dynamics, while a few defects diffuse in the saturated uniaxial nematic medium, the defect-anti defect pair annihilation process becomes faster than the zero temperature case, as shown in the inset of Fig.(5.8).

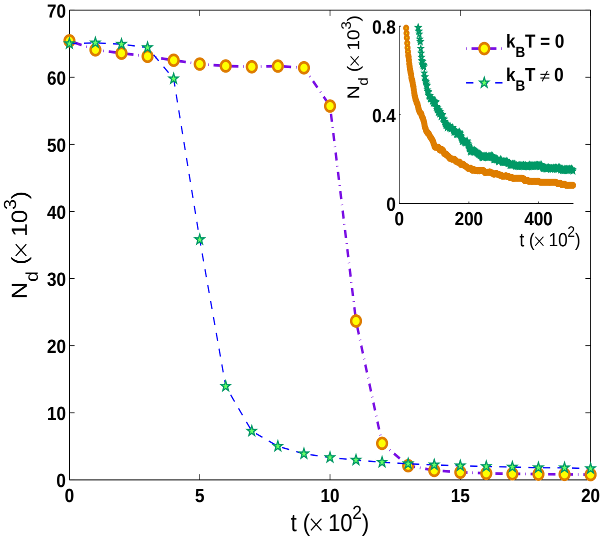

Figure 5.8: Effect of thermal fluctuations on the density of point defects with time is plotted. On a 256^2 lattice, time is iterated upto 5×10^4 steps with unit step length and averaged over 20 different initial configurations for both the cases with and without thermal fluctuation.

5.4 Phase ordering in biaxial nematics

5.4.1 Point defects : core structure and dynamics

Our study of the biaxial nematic incorporates the space variation of the triad **n**, **l** and **m** as well of the amplitude degrees of freedom S and T, unlike previous work [77]. As the system equilibrates after the biaxial quench, the magnitude of the order parameter converges to its equilibrium value.

Defects of all homotopy classes can be found after the extraction of the uniaxial and biaxial scalar order from the **Q** tensor. The homotopy classes are classified through the variation of the director configuration around the defect, by construction of topological circuits capturing the local minima. C_x (**n** rotates by $\pm\pi$, **l** does not rotate) and C_y (**n** does not rotate but **l** rotates by $\pm\pi$) class of defects are found, whereas no stable C_z (both **n** and **l** rotate by $\pm\pi$) class of defects are seen, consistent with the earlier analytical prediction [39] and numerical result [77].

Fig.(5.9) shows the uniaxial and biaxial order and the Schlieren textures at the indicated time steps after a biaxial nematic quench from an initial isotropic phase. In the Schlieren texture, both integer defects {four brushes at slightly north from the center of the frame [5.9(h)]} and half integer defects {two brushes in all of the three frames [5.9(g)-5.9(i)]} are seen at the early stage of the dynamics. Only half integer defects are present at the late stages of the dynamics, as indicated by two brushes in the texture frame [5.9(i)]. Although different class of defects are found in the texture, interestingly, signatures of all defect locations arising in the phase cannot be tracked only through the texture study, although they can be clearly

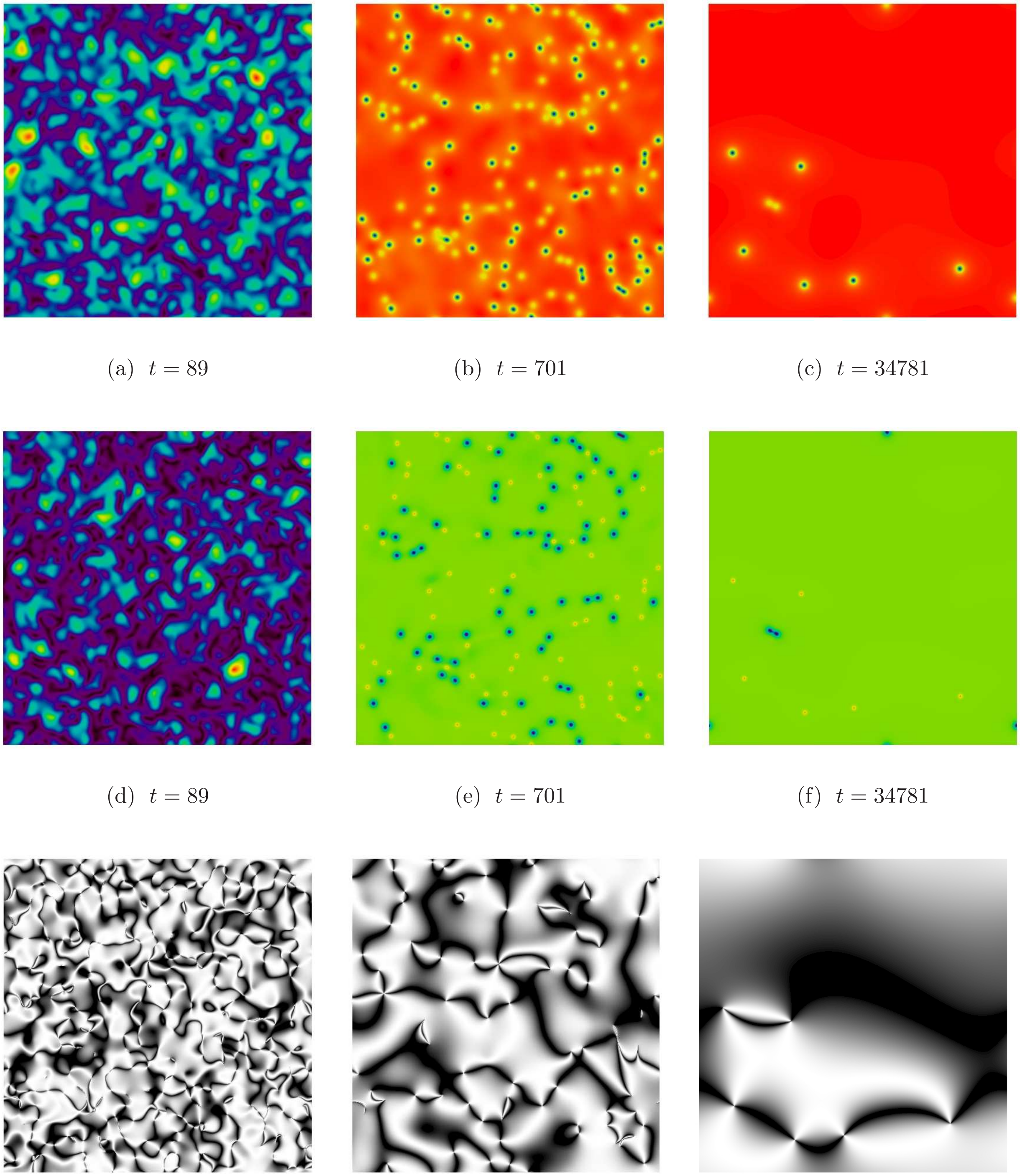

(a) $t = 89$

(b) $t = 701$

(c) $t = 34781$

(d) $t = 89$

(e) $t = 701$

(f) $t = 34781$

(g) $t = 89$

(h) $t = 701$

(i) $t = 34781$

Figure 5.9: Panel [(a)-(c)] shows the time evolution of the uniaxial degree of alignment, [(d)-(f)] the biaxial degree of alignment and [(g)-(i)] the Schlieren texture in a coarsening biaxial nematic.

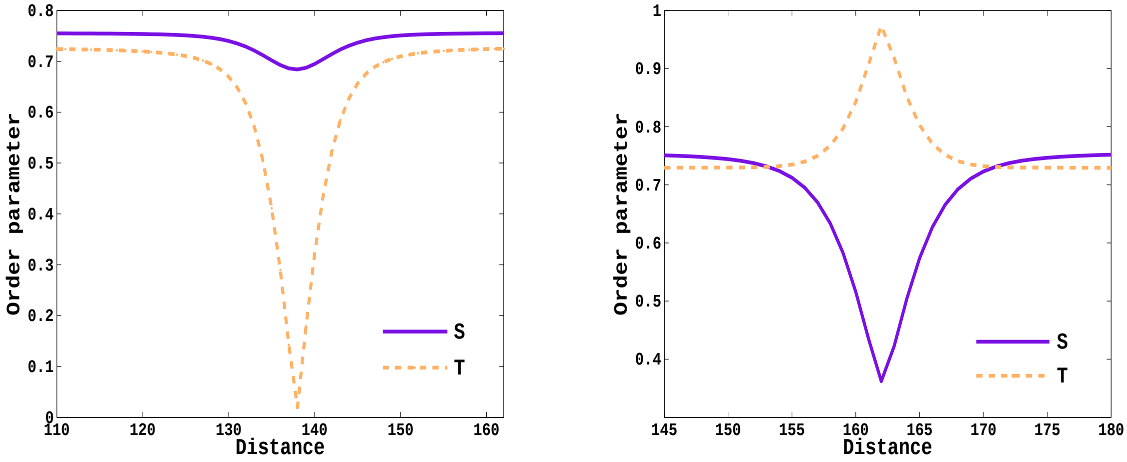

(a) (b)

Figure 5.10: Order parameter variation along the defect core of a quenched biaxial nematic phase. Panel (a) shows the uniaxial and biaxial degree of order in a C_x class of defect, while Panel (b) shows that of a C_y class of defect.

located in the uniaxial and biaxial scalar order. This also signifies those classes of defects where the deformation is solely embedded in the scalar order S and T and not in the vectorial order $\mathbf{n}$. We also note that the integer defects are purely due to deformation in the vector order $\mathbf{n}$ and no signature of deformation of S or T is noticeable in the field plots in Fig.[5.9(a)-(f)] at the place of texture with four brushes. Thus, our defect finding scheme, reported for the first time, is successful in locating all of the half-integer defect locations belonging to different classes, which cannot be tracked only from the study of Schlieren textures based on $\mathbf{n}$.

Fig.(5.10) shows the variation of S and T along the biaxial defect core located with our mentioned algorithm. In the C_x class of defects, though both uniaxial and biaxial order are reduced from their equilibrium values, biaxial order drops more significantly than the uniaxial order. In the C_y class of defects, while uniaxial order drops significantly from the equilibrium value inside the core, the biaxial order peaks. Thus the defect cores of the latter class behaves qualitatively like a half-integer defect-core in a uniaxial nematic.

5.4.2 Dynamical scaling in two dimensions: separation of time scale

To make a quantitative analysis of the dynamics of defects discussed in the previous subsection, we calculate the dynamical scaling exponent. In Fig.(5.11) we confirm the scaling of the direct correlation function and the structure function for a long period of time.

The length $L(t)$ is extracted from the real-space correlation function using the implicit condition $C(r = L(t), t) = 1/2$ as in the case of uniaxial quench discussed in the previous

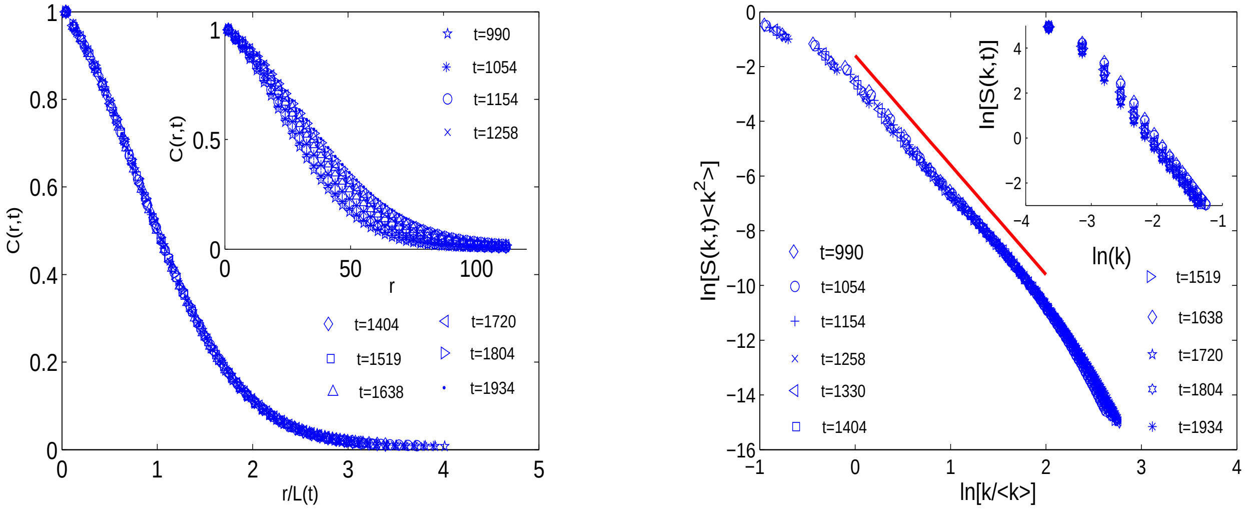

(a) (b)

Figure 5.11: (a) Data collapse of the direct correlation function $C(r,t)$ with the scaled distance $r/L(t)$ for different times. The inset depicts the unscaled correlator at different times. (b) Data collapse of the structure factor $S(k,t)$ with the scaled Fourier modes at different times. The depicted straight line with a slope of -4 indicates to the validity of generalized Porod's law for $O(n)$ vector model systems, with $n = d = 2$. The inset shows the unscaled correlator at different times.

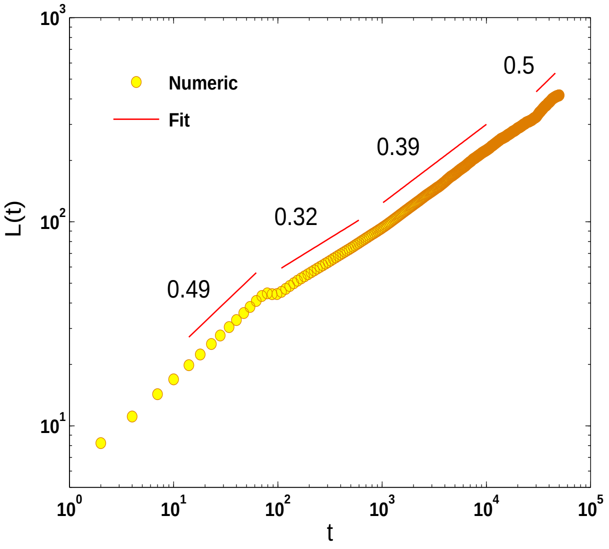

Figure 5.12: Growth of length scale with time in a biaxial quench. The time integration is done upto 5×10^4 steps with unit step length.

section. Fig.(5.12) shows the growth of the length scale as a function of time at different stage of the phase ordering kinetics. Theoretically the length scales with time as $L(t) \sim t^{\alpha}$. At an early stage of the kinetics, the dynamics shows a diffusive exponent with $\alpha = 0.49$. The diffusive nature of the dynamics at an early stage is attributed to the fact that the scalar order S and T reach equilibrium fast in comparison to the director $\mathbf{n}$ variable. The defect cores are not well-defined in this period of time.

In the later part of the dynamics, we observe a decrease of the exponent, with exponent values ranging from 0.32 to 0.39, finally regaining the diffusive exponent 0.5. In this intermediate regime of exponents, defect-defect kinetics proceeds via the annihilation of defect-antidefect pair of respective class. At still later stages of the kinetics, a small number of pairs of defects diffuse in the bulk nematic, and a diffusive scaling exponent is obtained.

In Fig.(5.15), we show the data collapse of the structure function as well as the uncollapsed data in the inset. We have, however, been unable to settle the question of the growth exponent conclusively.

5.4.3 Visualization of line defects commutation in three dimensions

Fig.(5.13) shows the corresponding uniaxial scalar field S at successive time steps after a biaxial nematic quench from isotropic phase. The inter-commutation of the line disclination is clearly noticeable, as seen in the south corner of the three frames [5.13(b)-5.13(d)]. The pair of lines corresponding to the defect-antidefect pair form a particular class which annihilates by forming a closed loop. Different loops pass through each other to form distinct loops which finally contracts and disappear from the system in the late stage of the kinetics. Superimposed with the scalar field S, change of the director field conformation on the stream tube of S is shown in Fig.(5.14) while an inter-commutation of defect line segments takes place.

As proposed from the topological restrictions on biaxial nematic defect classes forming the non-abelian group of quaternions, the inter-commutation of some classes of defect lines is forbidden because of the non-commutativity of the group elements. In our numerics, we do not observe any entanglement events. A plausible reason for the absence could be a local melting of the scalar order parameters while biaxial defect lines locally interact. Topological reasoning indicates that the merging of two defects depends strongly on the path which may or may not accompany the criterion of entanglement. Energetically a $\bar{C}_0$ defect lies higher in energy landscape than other C_i, $(i = x, y, z)$ class of defects. So a $\bar{C}_0$ defect dissociates into low energetic stable class of defect at late stages prohibiting two π defects entangle through a 2π "umbilical" cord, as been analytically predicted by Kobdaj and Thomas in two dimensions [39]. (The generalization of these results to three dimensions is natural.) The only possible ways of defect entanglement is found in the experiemntal and theoretical studies of: *i)* cholesterics or chiral nematics that exhibits of a defect-locked blue phase [48], *ii)* chiral nematic colloids [68], *iii)* nontrivial boundary driven nematogenic systems etc. The absence of chirality in our studied system can also be another plausible reason for the absence of defect entanglement.

In Fig.(5.15), we show the data collapse of the structure function as well as the uncol-

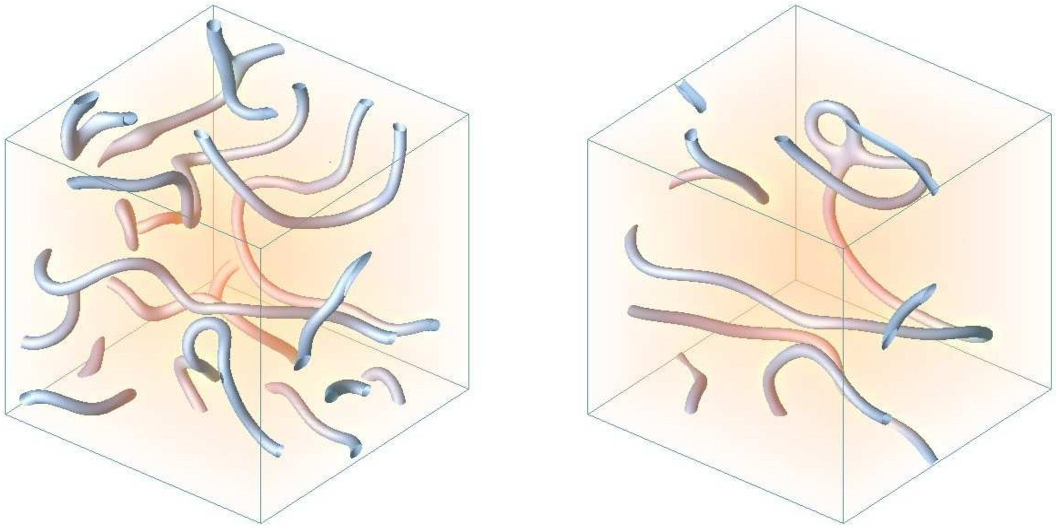

(a) $t = 1200$ (b) $t = 1600$

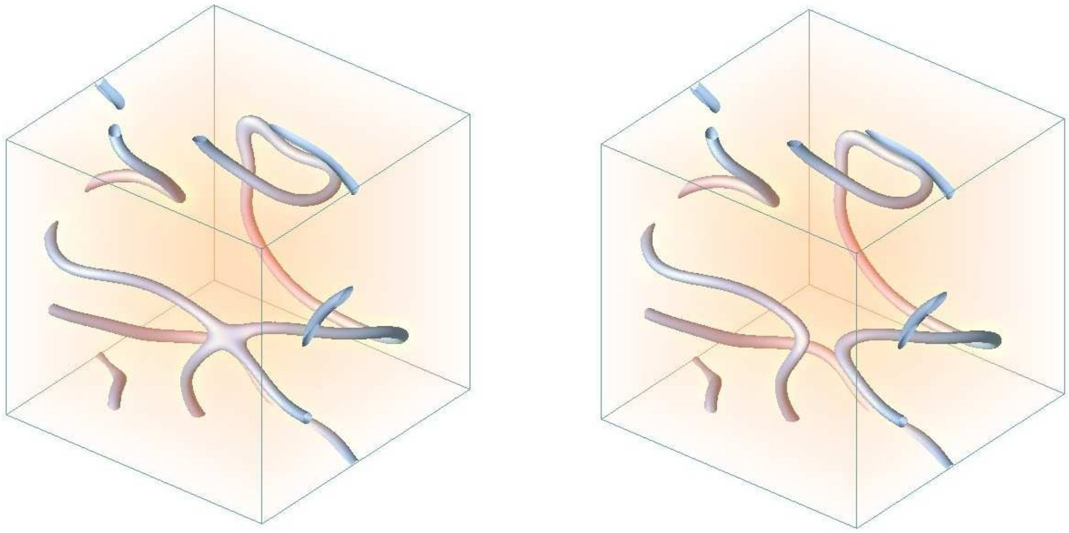

(c) $t = 1800$ (d) $t = 4400$

Figure 5.13: Time evolution of uniaxial degree of alignment [Frames {5.13(a)- 5.13(d)}] in a coarsening 3D biaxial nematic, plotted at an isosurface value 0.5 and volume rendered in false colours.

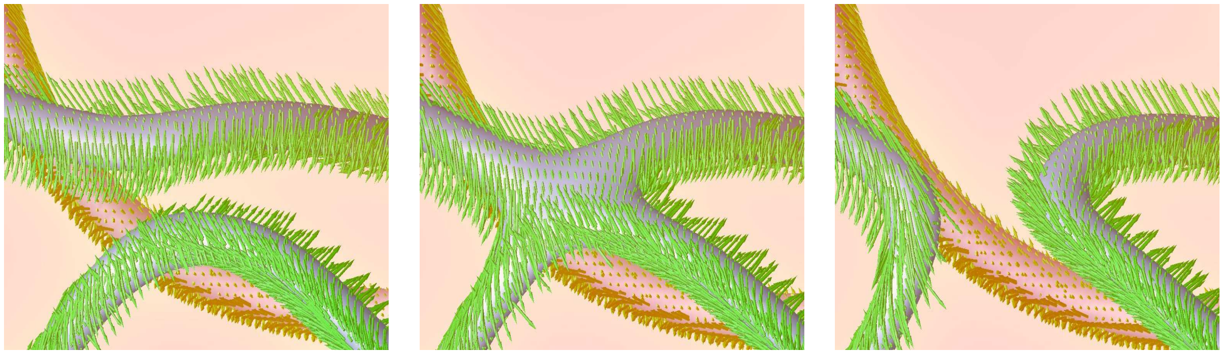

(a) $t = 4500$ (b) $t = 4900$ (c) $t = 5100$

Figure 5.14: Time evolution of uniaxial degree of alignment in a coarsening 3D biaxial nematic. Frames [5.14(a)- 5.14(c)] show zoom of the intercommutation with the director field conformation around the disclination.

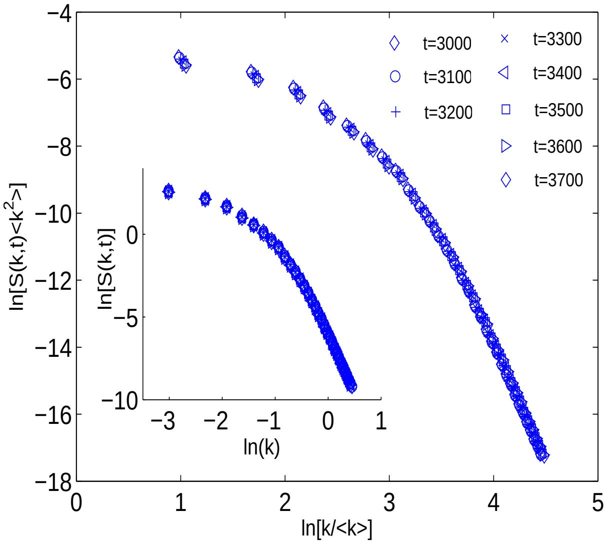

Figure 5.15: Data collapse of the structure function $S(k, t)$ with scaled Fourier modes for different times. The inset shows the unscaled correlator at different times.

lapsed data in the inset. However, accurate estimations of the growth exponent have not been carried out due to lack of sufficient data for the statistical averages to be meaningful.

5.5 Conclusion

In this chapter, we have described point and line defects of different homotopy classes which arise in our numerics. We discussed phase ordering kinetics in uniaxial nematic phases, validating the theory by locating integer and half integer defects corresponding to $\pi_i(\mathcal{R})$.

We demonstrate that the late-stage growth exponent in two-dimensional uniaxial nematics is 0.5, confirming scaling expectations. For uniaxial and biaxial nematics in three dimensions, we show the existence of an asymptotic 0.5 growth exponent.This asymptotic behaviour, however, is obtained only after a long crossover regime in which the data can be fit to numbers between 0.32 - 0.39, suggesting that the data of Zapotocky *et al.* and of other previous workers may have been confined to this crossover regime. We numerically observe defects in biaxial phase ordering but find no evidence for entanglement of defects, as posited by the topological theory of defects. However, we see clear indication for intercommutation of string defects in three dimensions and our novel visualization techniques enable us to track the detailed variation of the order parameter structure through such intercommutation events. These observation suggest that similar methodologies may find powerful application in the study of defect kinetics in these and similar systems with complex defects.

Chapter 6

Breakdown of classical nucleation theory in nucleation kinetics

In this chapter we present results of a study of nucleation of nematic droplets from the metastable isotropic phase. To the best of our knowledge, this is the first study of the kinetics of nematic nucleation which is based on a Ginzburg-Landau description. We use the stochastic equations of motion for the nematic director presented earlier, together with a method of lines integration scheme, to study this problem. As in the studies of the previous chapters, all five tensorial degrees of freedom of the nematic director are allowed to fluctuate. This allows for novel kinetic pathways, absent in liquid-gas or liquid-liquid nucleation, through which nematic droplets can form. The few previous studies of this problem where full director fluctuations are included were particle-based Monte-Carlo simulations of hard spherocylinders (HSC), whose kinetic interpretation can be ambiguous.

Our principal results are the following. In both two and three dimensions, the overall shape of the nematic droplet is generally ellipsoidal, and not spherical as assumed in classical nucleation theory. In two dimensions, depending on the signs of the elastic constants and the anchoring conditions they enforce on the director, we find that nematic nuclei contain defects within them. In three dimensions, we are not able to clearly discern their presence in the droplet, but we do find a non-uniform director distribution in the nuclei. Our study thus reveals pathways that involve states with non-trivial spatial distributions of the nematic director, which are not accounted for in classical nucleation theory. Our study shows that classical nucleation theory, with its assumption of spherical, spatially uniform nuclei, is insufficient to account for the complexity of nematic droplet nucleation.

6.1 Introduction

As the transition from isotropic to nematic phase is *weakly* first order, there exists a regime of parameters where the kinetics proceeds through nucleation of the stable phase in the unstable medium. This regime is bounded by the binodal and spinodal lines as indicated in the phase diagram Fig.(1.5). Classical homogeneous nucleation theory, with a non-conserved order parameter, studies the critical droplet size, the energy of the barrier height and the nucleation rate of a single droplet, all with an inherent assumption of nucleation that proceeds through the formation of spherical droplets of radius R.

The free energy of a droplet consists of contributions from the energy of the bulk (which is the volume energy of the nucleating stable phase) and the surface energy required to create the interface between the stable and the metastable medium. This can be defined as

$$\mathcal{F}(R) = -V\rho_N\Delta\mu + \mathbb{A}\sigma, \tag{6.1}$$

where $V = \frac{4}{3}\pi R^3$ is the volume and $\mathbb{A} = 4\pi R^2$ is the surface area of the spherical droplet, ρ_N is the density of the nucleating stable phase and $\Delta\mu = \mathbb{L}\Delta T/T^*$ is the change in the chemical potential of the unstable to stable phase. $\mathbb{L}$ is the latent heat emitted due to the change in temperature ΔT, critical temperature is denoted by T^* and σ is the surface tension.

A droplet of stable phase in an unstable background shrinks if it is smaller than a critical size R_c. Droplets which are larger than R_c grow in size till they expand to the size of the system. A droplet of size R_c is thus metastable. The critical shape of the droplet is obtained by maximizing $\mathcal{F}(R)$ with respect to R, resulting into $R_c = 2\sigma/\rho_N|\Delta\mu|$.

The barrier height can also be calculated by using this form of R_c as $\mathcal{F}_c = 16\pi\sigma^3/3\rho_N^2(\Delta\mu)^2$. From this, the nucleation rate can be calculated which is defined as, $I = Z\rho_I f_c^+ \texttt{exp}[-\mathcal{F}_c/k_BT]$. Here, $Z = \sqrt{|\Delta\mu|/6\pi k_BTn_c}$ is the Zeldovich factor, n_c is the number of monomers in the critical nucleus, ρ_I is the density of the unstable phase and f_c^+ is the rate of attachment to the critical nucleus [5]. Typically, in classical nucleation theory (CNT), the calculation of the rate is a formidable problem as the quantities f_c^+ and σ are outside the scope of experimental measurements which can be matched with theoretical predictions.

The development in time of a fluctuation-induced nematic droplet is a key factor in determining the nucleation rate in nematics [22]. Unlike conventional isotropic fluids, as the nucleation of crystalline phases does not proceed through formation of a spherical nucleus due to the anisotropic surface tension, the nucleus in a nematic is also not expected to be spherical [9]. Allowing the shape to deviate from perfect sphericity reduces the total energy, which is a sum of the elastic energy associated with the director deformation in the bulk and a surface energy associated with the anchoring condition at the interface of the droplet. Thus, determining the droplet shape of least energy involves a minimization over the strength of ordering as well as the director degrees of freedom [33, 16, 73].

Prinsen and Schoot studied the shape and director field conformation of nematic tactoids within a Frank description of the elastic free energy [59]. In their formulation, a planar anchoring condition of the director to the interface is enforced through a plausible surface free energy term proposed by Rapini and Papoular [61]. By minimization of the free energy, different morphology of ellipsoidal nematic droplets has been proposed as a function of the elastic stiffness and the anchoring strength. No kinetic description is available of the nucleation and the growth of nematic tactoids.

The only study of kinetic pathways of growth of nematic droplet is addressed by Cuetos and Dijkstra through a Monte Carlo study of HSC [22]. They studied the pressure controlled supersaturation of colloidal fluid with two different aspect ratios of the HSC, as well as the nucleation and growth from an isotropic to nematic transition below the critical temperature. Their principal findings are that for a high aspect ratio, an ellipsoidal nematic cluster with a homogeneous director field forms and grows in time to span the system size. However the

Figure	A	B	C	E'	L_1	κ	Γ	k_BT	System size
6.1	10^{-3}	-0.5	2.67	0	0.01	0	5	2.0807×10^{-7}	256^2
6.2	10^{-3}	-0.5	2.67	0	0.0236	0	1	0	128^2
6.3	10^{-3}	-0.5	2.67	0	0.01	20	5	2.0807×10^{-7}	256^2
6.4	10^{-3}	-0.5	2.67	0	0.0236	10	1	0	128^2
6.5	10^{-3}	-0.5	2.67	0	0.01	-0.5	5	2.0807×10^{-7}	256^2
6.6	10^{-3}	-0.5	2.67	0	0.0236	-1	1	0	128^2
6.7-6.8	10^{-4}	-0.5	2.67	0	0.01	0	20	2.0807×10^{-7}	128^3
6.9-6.10	10^{-5}	-0.5	2.67	0	0.01	10	10	2.0807×10^{-7}	128^3
6.11-6.12	5×10^{-5}	-0.5	2.67	0	0.01	-1	5	2.0807×10^{-7}	128^3

Table 6.1: Numerical parameters in the Landau-de Gennes theory used for the computer experiments in nucleation kinetics presented in this chapter.

kinetic description is not well-defined in a Monte Carlo technique as it samples only the most probable states. Although in Monte Carlo technique, the local moves can faithfully reproduce the Brownian dynamics trajectories for rod-like particles, but a true kinetic pathway is outside the scope of such studies. We mention that a truly kinetic scenario can only be captured through the dynamical study of the tensorial order parameter $\mathbf{Q}$ defined in Eq.(2.2). The GLdG parameters used for the calculations are highlighted in Table 6.1.

6.2 Structure of nucleated nematic droplets in two dimensions

We consider the nucleation of a nematic droplet in an isotropic background, in the presence of the fluctuations in the orientation due to temperature. We prepare an isotropic phase with the mean of S and T set to zero but with finite variance. We construct the $\mathbf{n}, \mathbf{l}, \mathbf{m}$ triad such that the direction is completely random in the three Cartesian directions. We evolve the nematodynamic equation (2.2) and study the phase behaviour in the early and late stage of the kinetics. The nematic droplets nucleate in the isotropic phase due to the external thermal noise ξ, which serves as the driving force that drives the isotropic state to overcome the nucleation barrier. We incorporate the anisotropic contribution to elasticity of both positive and negative signs of elastic constant while ensuring the positivity of the Frank elastic constants. We systematically discuss different cases while comparing the results with the zero temperature mean field calculation in the following subsections.

6.2.1 Circular droplets with uniform director at $\kappa = 0$

In the absence of the anisotropic elastic term in the equation of motion, several spherical droplets of uniaxial nematic phase nucleate in the fluctuating isotropic medium with homogeneous director anchoring inside the droplet. The direction of orientation of the director is local to the droplets, and is different from droplet to droplet. These droplets grow in size by reducing the isotropic region significantly and coalesce with each other while evolving in time, smoothing out the director field throughout the system to reduce the elastic energy. In this process, topological defects form due to the coalescence of droplets, which annihilate at the late stage of the dynamics satisfying topological constraints. Finally, the stable uniaxial nematic phase fluctuates in equilibrium.

Fig.(6.1) shows the scalar order parameter S in false colours and the director field **n** as needles superimposed on top of that. To avoid clumsiness in the description, the director is plotted on each and every fourth lattice point in all of the directions. The formation of several nematic droplets[1] are shown in Fig.[6.1(a)]. The nematic phase with defects at a late stage is shown in Fig.[6.1(b)], where the defect-anti defect pair eventually annihilates. Fig.[6.1(c)] and Fig.[6.1(d)] show the schlieren textures at the time of formation of droplets and a later time of fully developed defects at the fluctuating nematic phase. We notice that our previous assumption of uniform director field inside the immersed nematic droplet as discussed in the previous section, holds well with a spherical shape of the droplet.

To compare the obtained result with the mean field calculation, we have also studied the time evolution of a single nematic droplet immersed in an isotropic background working at the zero temperature limit of the problem. To study any conformational changes to the droplet, our initial condition was chosen so as the uniaxial order was set to the equilibrium value ($S = S_c$) with the director anchored at an angle of $\pi/4$ with the nematic-isotropic interface inside the droplet. We took $S = 0$ in the isotropic region, while randomly orienting the direction of the triad and relaxed the system at a temperature intermediate between the binodal and spinodal temperatures in the absence of fluctuation.

For droplets larger than the critical radius, the nematic region was observed to grow in size, finally evolving into the nematic state spanning the system size. For the parameters used, the alignment of the director did not change significantly during the evolution of the droplet. Fig.(6.2) shows the evolution of a single, initially circular droplet, illustrating how the droplet shape evolves in a circular fashion in the absence of elastic anisotropy $\kappa = 0$.

6.2.2 Complex droplet geometry with integer defect at $\kappa > 0$

With a positive contribution of the elastic anisotropy to the free energy, in the droplet growth regime, we notice a change in the geometry of the nucleated nematic droplet, satisfying earlier

---

[1] The formation of a single nematic droplet is outside the scope of computational time and resources, since to observe a single droplet nucleation event, the free energy must be deep inside the nucleation regime (not close to the spinodal lines as in the cases studied here). This increases the first passage time considerably, making droplet nucleation a rare event.

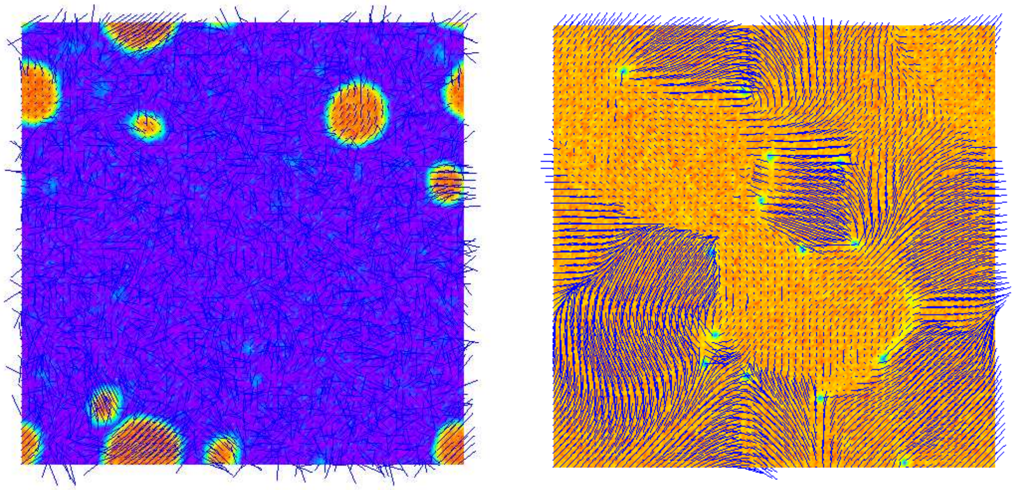

(a) $t = 1200$ (b) $t = 3300$

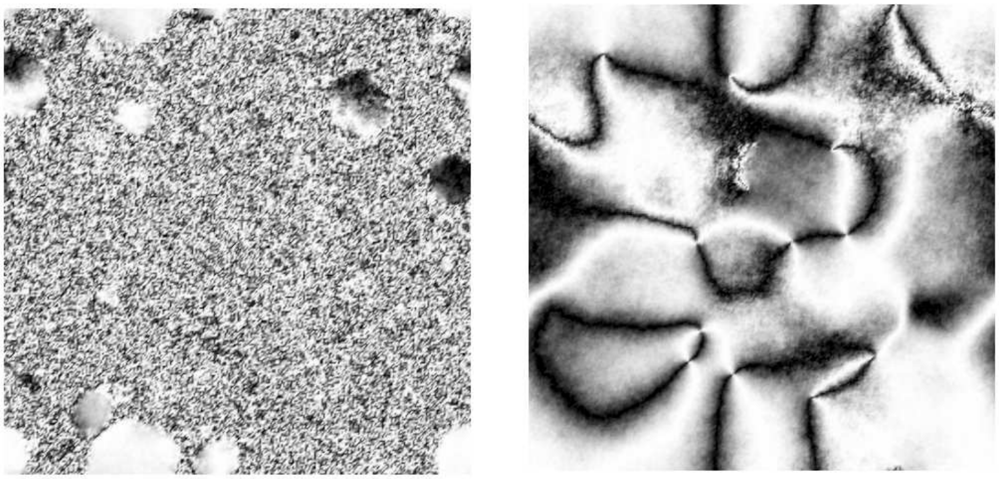

(c) $t = 1200$ (d) $t = 3300$

Figure 6.1: The first two frames designate the degree of uniaxial order and director conformation of the nucleating droplets. The last two show the corresponding schlieren textures. Panel (a) shows the circular droplets with uniform director at an early stage. The full grown defects at a late stage is been shown in panel (b). Panel (c) shows differently oriented, uniform nematic domains while the half integer defects (two brushes) are shown in panel (d). The SRK4 numerical integration is performed upto 1.2×10^4 iterations with unit time increment.

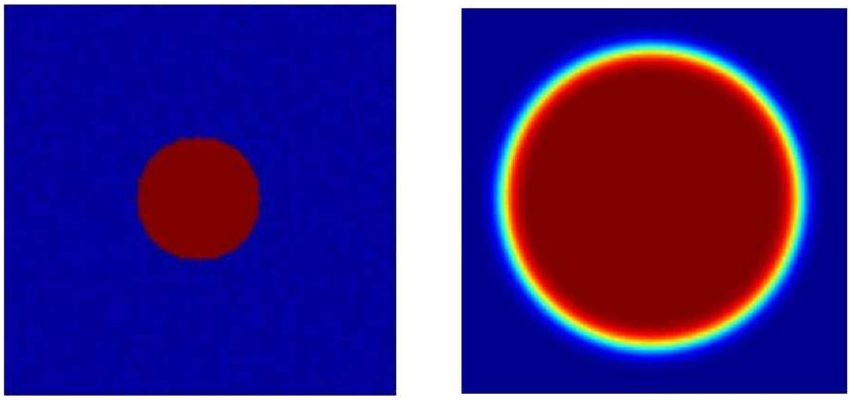
(a) $t = 0$ (b) $t = 3000$

Figure 6.2: Time evolution of the uniaxial order in the relaxation of a nematic droplet. Fig.(a) shows the circular droplet at time $t = 0$. The time evolution with $\kappa = 0$ of the circular droplet at a later time $t = 3 \times 10^3$ is shown in fig.(b).

theoretical predictions and numerical estimates. The initial elliptic nuclei, however, change shape to complex geometries before coalescence. Also, we observe the existence of topological defects with integer charge, a hedgehog conformation of the director, formed inside each and every droplet. This result has not been reported in the literature. A plausible reasoning for the formation of the defects could be the small ratio of the volume to surface free energy, which results into a deformation of the bulk nematic director inside the droplet to a hedgehog structure due to the strong anchoring of the director at the surface of the droplet. At late stages of the dynamics, the bubbles coalesce and the fluctuating uniaxial nematic phase spans the system size as discussed in the previous subsection. Unlike the previous case, we never observe half integer defects forming due to coalescence of the nematic droplets.

Fig.(6.3) shows the scalar order parameter S in false colors and the director field as needles superimposed on tops. For visualization purposes, the director is shown at every fourth lattice point. Fig.[6.3(a)] shows the formation of droplets with an ellipsoidal shape with an integer defect inside the droplets at an early stage. Fig.[6.3(b)] shows the evolution of the ellipsoidal droplets to complex structures at a late stage of the kinetics. The schlieren textures at these particular times are shown in Fig.[6.3(c)-6.3(d)]. The interesting fact we note is even at the late stage of the kinetics, while the droplets completely coalesce to form the fluctuating nematic phase, integer defects persist till the end of the kinetics with a relaxation time much larger than that of the computational time. Qualitatively, this matches the experimental predictions reported in the reference [60].

In our mean field calculation without incorporating fluctuation in temperature but in the presence of elastic anisotropy, the droplet orients along the direction of nematic order for planar anchoring ($\kappa > 0$). In our numerics, we quantify the geometrical change through measurements of the change in the aspect ratio. The aspect ratio, defined as the ratio of the

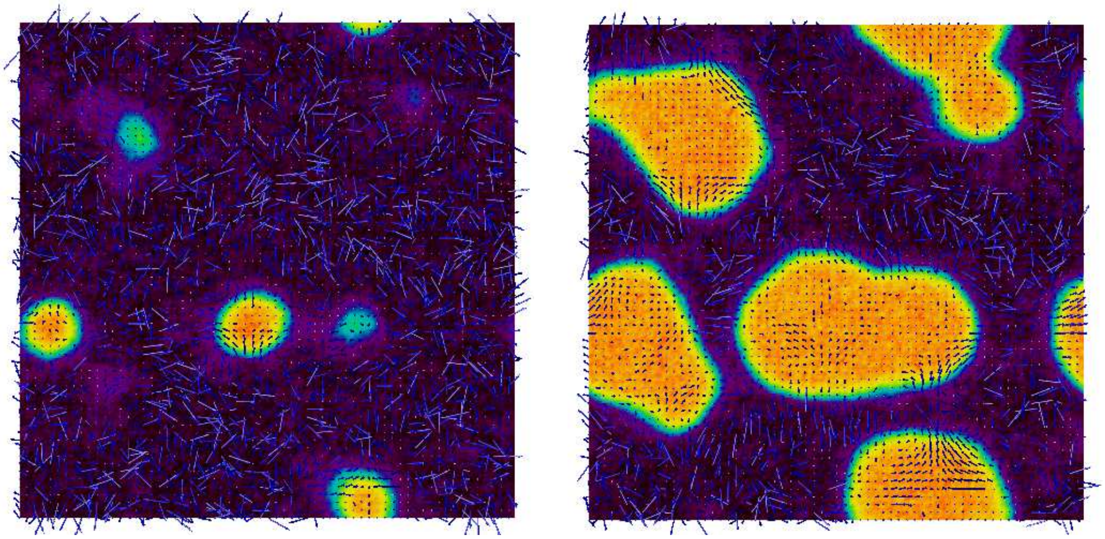

(a) $t = 2040$ (b) $t = 2400$

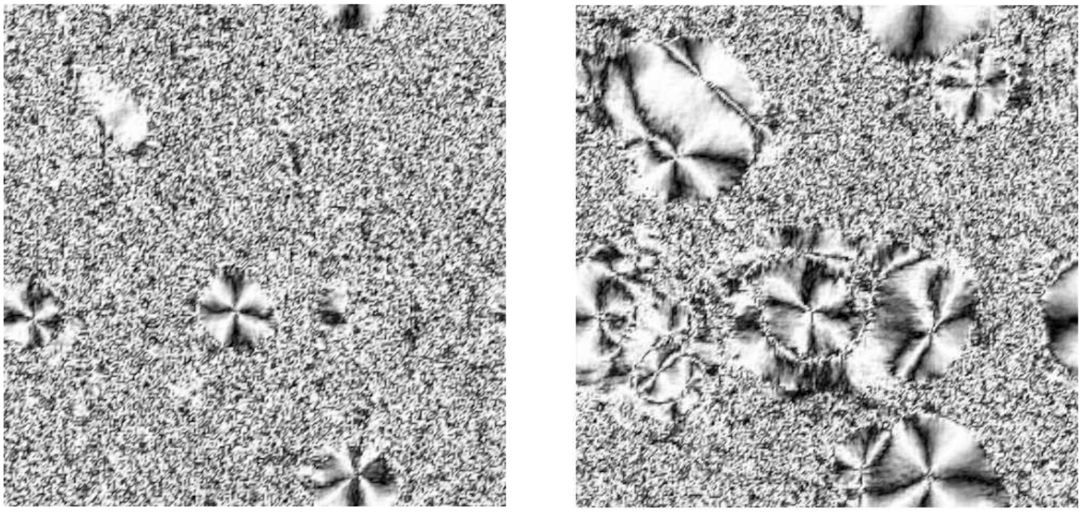

(c) $t = 2040$ (d) $t = 2400$

Figure 6.3: The first two frames show the degree of uniaxial order and director conformation of the nucleating droplets, while The last two show the corresponding schlieren textures. Panel (a) shows the nucleated ellipsoidal droplets at an early stage of the kinetics. Panel (b) shows complex droplet structures at a late stage (before coalescence of domains). Panel (c) shows the integer defect with four brush while panel (d) shows the grown brushes of the defects. The SRK4 numerical integration is performed upto 1.2×10^4 iterations with unit time increment.

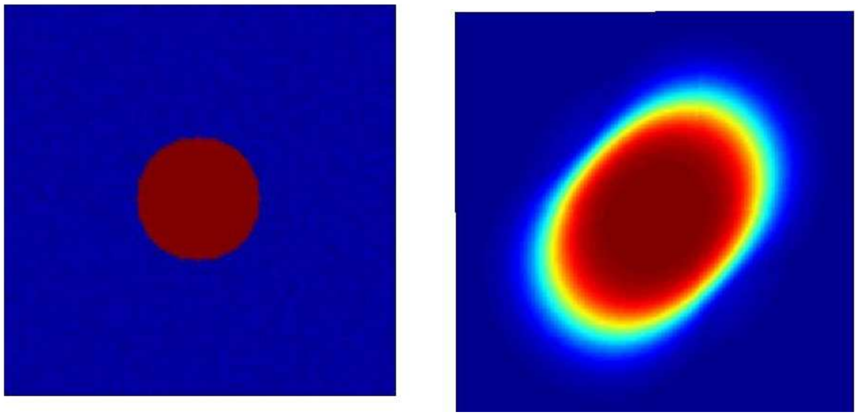

(a) $t = 0$ (b) $t = 900$

Figure 6.4: Time evolution of the uniaxial order in the relaxation of a nematic droplet. The initially circular droplet develops an anisotropy and becomes elliptical, the two-dimensional analogue of the ellipsoidal droplets (tactoids) seen in three dimensions. Fig.(a) shows the circular droplet at time $t = 0$. The elliptical conformation with $\kappa > 0$ at a time $t = 6 \times 10^2$ is shown in fig.(b) having aspect ratio 1.5037. The droplet radius is taken to be 20.

major to minor axis of the ellipse, are indicated in Fig.(6.4). This is calculated by extracting a contour at a fixed value of S (say $S_c/2$) and fitting it with an ellipse. The aspect ratio in $\kappa > 0$ changes from 1 as $1.1191, 1.3046$ and 1.5037 from time $t = 0$ to $300, 600$ and 900 respectively.

6.2.3 Ellipsoidal droplets with uniform director at $\kappa < 0$

In the presence of a negative contribution of the elastic anisotropy to the droplet surface energy, we notice formations of ellipsoidal droplets with homogeneous director anchoring. These droplets coalesce to form topological defects which eventually disappear from the system by the defect-antidefect annihilation process. Though we expect defects inside the droplets with a finite contribution from the anisotropic elasticity, a plausible explanation could be the higher volume to surface energy ratio. The surface anchoring of the nematic director is unable to deform elastically the director in the bulk significantly, thus resulting into a smooth director field inside the droplet.

Fig.(6.5) shows the scalar order parameter S in false colors with the director field $\mathbf{n}$, plotted as needles superimposed on top. For visualization purposes, the director is strided at every fourth lattice point. Fig.[6.5(a)-6.5(b)] shows the formation and complex structures of the nematic droplet in the growth kinetics. The schlieren textures at these particular times are shown in Fig.[6.5(c)-6.5(d)].

In our mean field calculation without incorporating fluctuation in temperature but in the presence of elastic anisotropy, the droplet orients perpendicular to the direction of nematic

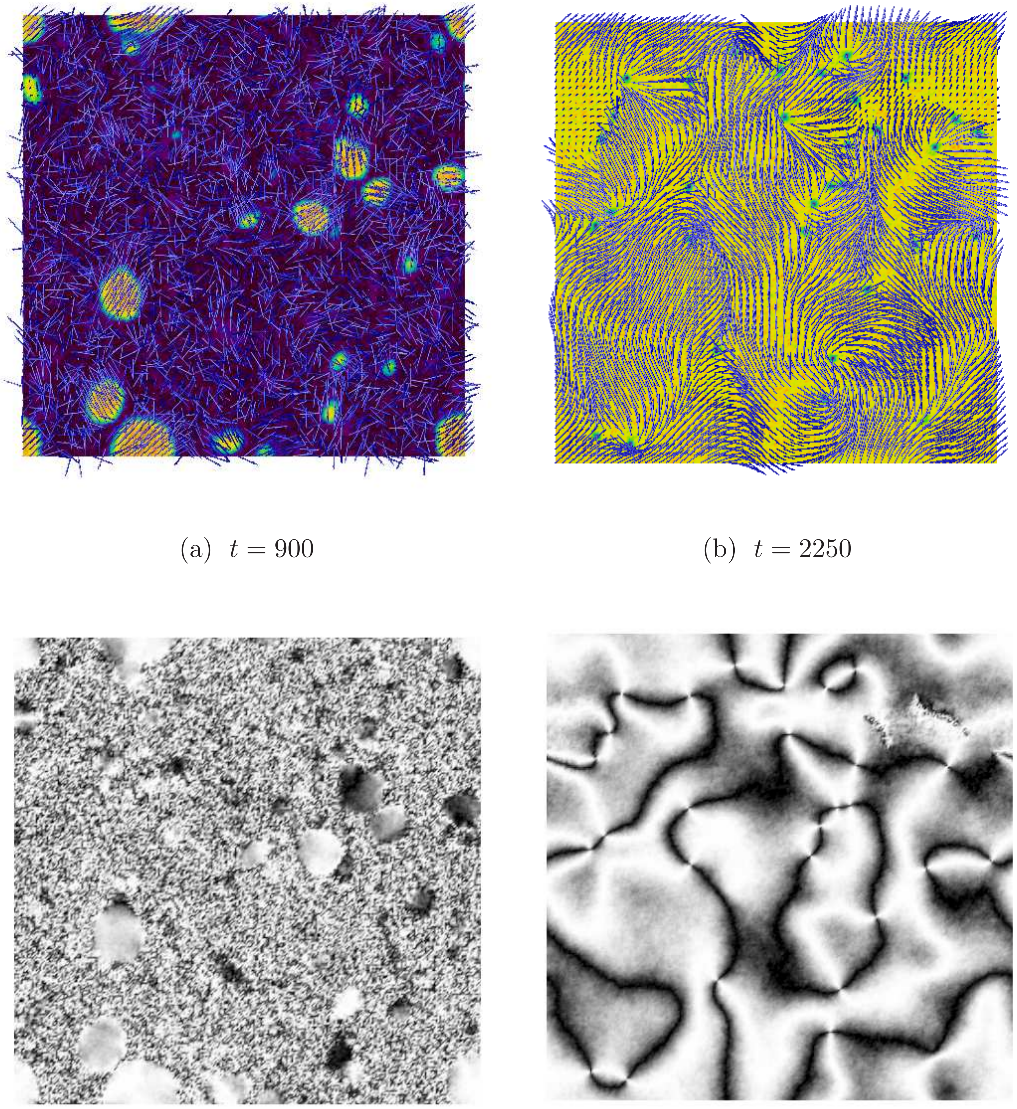

(a) $t = 900$

(b) $t = 2250$

(c) $t = 900$

(d) $t = 2250$

Figure 6.5: The first two frames show the degree of uniaxial order and director conformation of the nucleating droplets, while The last two show the corresponding schlieren textures. Panel (a) shows the elliptical droplets with uniform director conformation, panel (b) shows the grown defects at a late stage. Panel (c) shows the uniformity of the droplets while panel (d) shows the half integer two-brush defects. The SRK4 numerical integration is performed upto 1.2×10^4 iterations with unit increment.

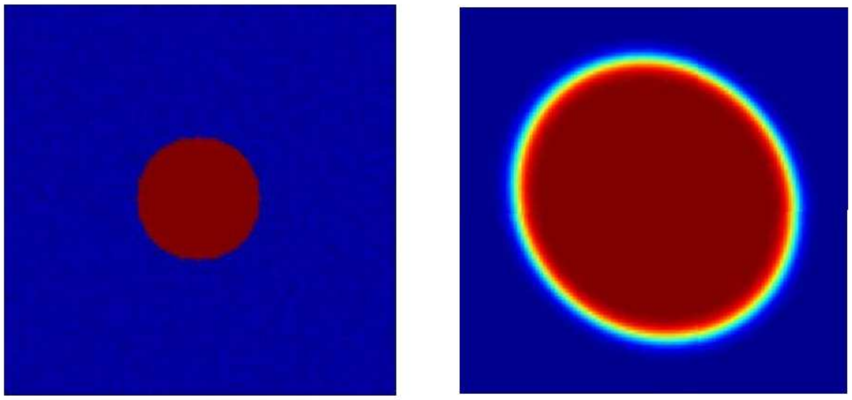

(a) $t = 0$ (b) $t = 1500$

Figure 6.6: Time evolution of the uniaxial order in the relaxation of a nematic droplet. Fig.(a) shows the circular droplet at time $t = 0$. With $\kappa < 0$ conformation is shown in fig.(b) having aspect ratio 1.1316.

order for homeotropic anchoring ($\kappa < 0$), while changing shape from circle to ellipse as indicated in Fig.(6.6). The aspect ratio at time $t = 0$ changes from 1 to $1.0122, 1.0718$ and 1.1316 in time $t = 500, 1000$ and 1500 respectively.

To the best of our knowledge, there are no analytical expressions for order parameter variations for nematic droplets in all these three cases of κ. Thus, our results cannot be compared directly against analytical theory. However, the results obtained are in qualitative agreement with previous work on the shape of nematic droplets as a function of anchoring strength [59, 33, 16, 73].

6.3 Structure of nucleated nematic droplets in three dimensions

We discuss the nucleation of nematic droplets in an isotropic environment in three space-spin dimensions with the three cases of κ in the following subsections.

6.3.1 Spherical droplets with $\kappa = 0$

Fig.(6.7) depicts four snapshots of the nucleation process of uniaxial nematic droplets at the isotropic medium. Nucleation events are followed by a coarsening kinetics while the droplets coalesce amongst themselves to form defect-anti defect strings. These eventually annihilate from the system by segment intercommutation and the formation of loops which contract.

Our central result is, with a zero contribution to the surface free energy from the anisotropic gradients, the nucleation event proceeds with the formation of spherical droplets. Fig.(6.8) shows the the uniaxial scalar field and the vector field conformation of the director at a particular time. The uniformity of the director is noticeable from the first two confor-

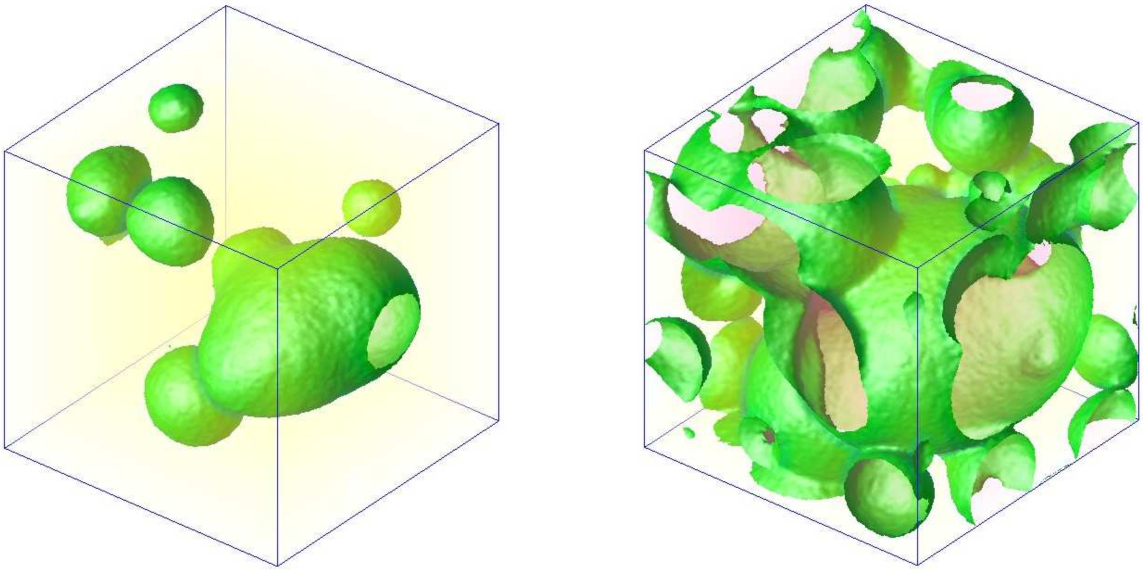

(a) $t = 600$ (b) $t = 690$

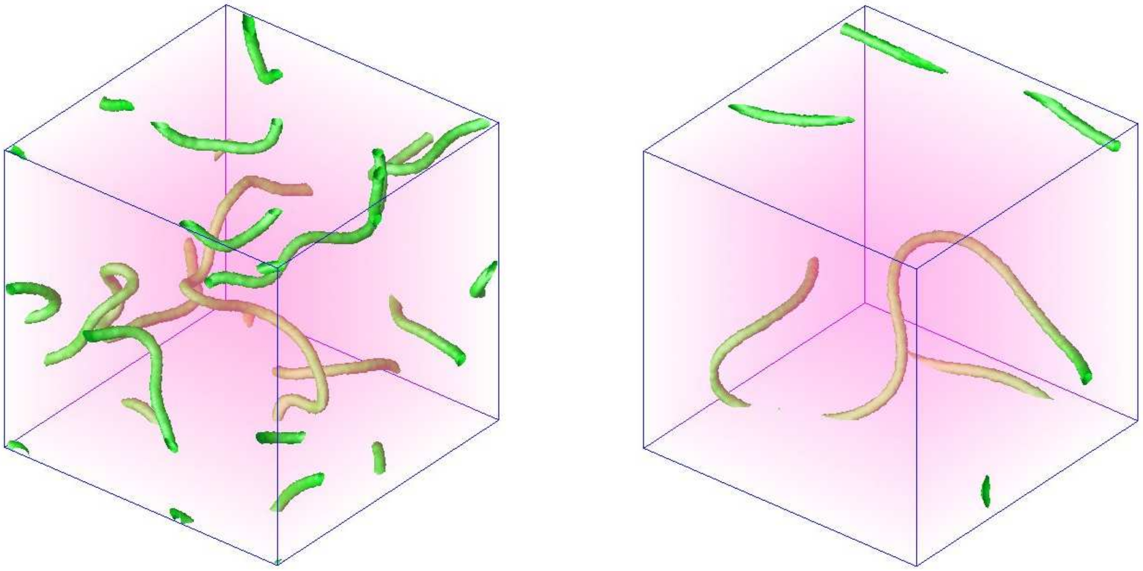

(c) $t = 900$ (d) $t = 3000$

Figure 6.7: Time evolution of uniaxial order in a three dimensional volume. Panel (a) shows the emergence of uniaxial nematic droplet in the fluctuating isotropic medium. The coalescence of droplets, as shown in panel (b), form line defects as shown in panel (c). The defects at a late stage of the kinetics is shown in panel (d). The isosurfaces are plotted for a fixed isovalue $S = 0.05$. The numerical integration is performed upto 3×10^3 SRK4 iterations with unit increment in time.

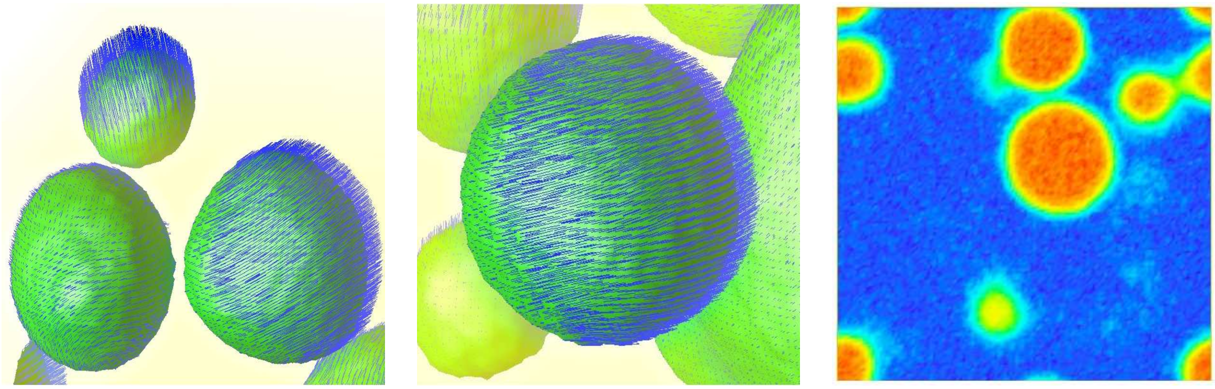

(a) $t = 600$ (b) $t = 600$ (c) $t = 600$

Figure 6.8: Panel (a) and (b) show the uniaxial order and director conformation on the surface of nucleated nematic droplets in three dimensions. Panel (c) shows the uniaxial order in a plane (say x-y) that slices the three dimensional volume at $z = 20$. The isosurface is plotted for a fixed isovalue $S = 0.05$. The numerics is performed upto 3×10^3 SRK4 iterations with unit time increment.

mations. The spherical shape is been shown through a cut in the three dimensional volume at a fixed value of z in the $z-$axis.

6.3.2 Ellipsoidal droplets with $\kappa > 0$

Fig.(6.9) depicts four frames of the nucleation event happening in the presence of elastic anisotropy in the free energy. The uniaxial nematic droplets nucleate in the isotropic background, which eventually coarsens through the coalescence of the droplets to form defects. These defects annihilate through the usual defect string dynamics.

Our central result is the change of shape in the droplet conformation in the early stages of nucleation. Fig.(6.10) depicts the local tilt angle $\theta = \cos^{-1}(\mathbf{k} \cdot \mathbf{n}), (0 \leq \theta \leq \pi)$ on the surface of the droplets as well as a slice of the three dimensional volume at a particular value of z in the $z-$axis. As can be clearly noticeable, the change of colours on the surface of the uniaxial droplet clearly confirms the variation of the director. Thus CNT predictions for the nucleation rate will not estimate the droplet nucleation rate correctly. However, we are unable to locate any defect conformation inside or on the surface of the droplet. The ellipsoidal nature of the droplet can be visualized in Fig.[6.10(b)]. Like the two dimensional case, we also notice that the first passage time is slightly higher than the previous case.

6.3.3 Ellipsoidal droplets with $\kappa < 0$

Fig.(6.11) depicts the nucleation of the uniaxial nematic droplets in an isotropic medium in the presence of a negative contribution of the elastic anisotropy to the free energy. Like

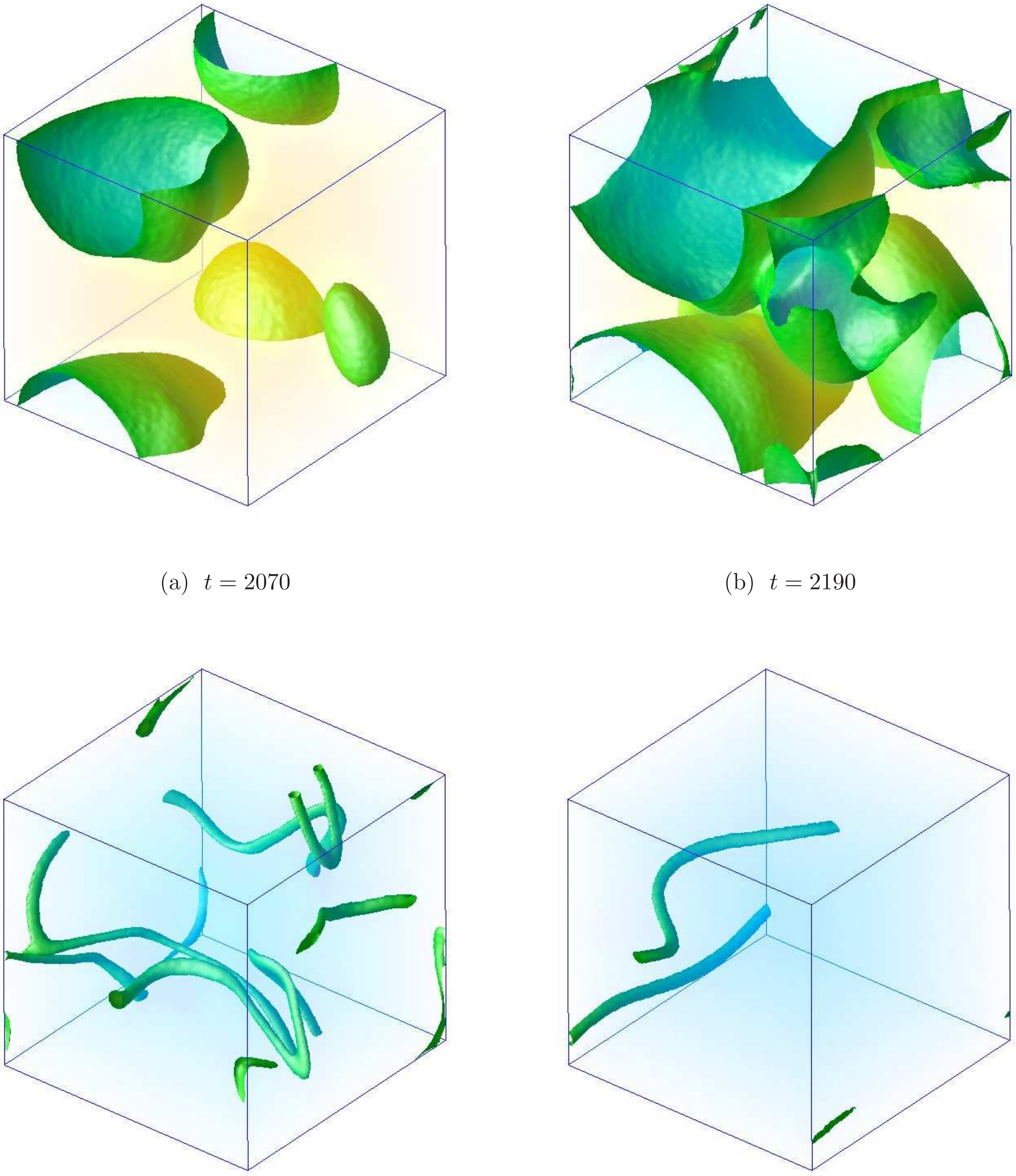

(a) $t = 2070$

(b) $t = 2190$

(c) $t = 2370$

(d) $t = 6000$

Figure 6.9: Time evolution of uniaxial order in a three dimensional volume. Panel (a) shows the emergence of uniaxial nematic droplet in the fluctuating isotropic background. Panel (b) shows the coalescence of droplets, and the formation of line defects are shown in panel (c). The defects at a late of the kinetics is shown in panel (d). The isosurfaces are plotted for a fixed isovalue $S = 0.04$. The numerics is performed upto 6×10^3 SRK4 iterations with unit increment in time.

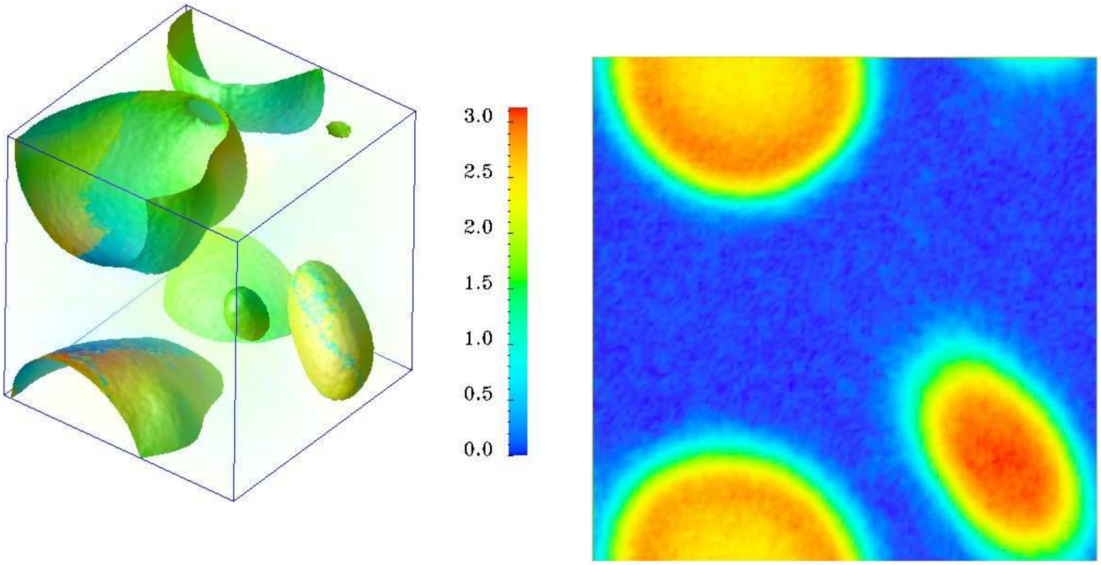

(a) $t = 2100$

(b) $t = 2070$

Figure 6.10: Panel (a) shows the uniaxial order and director field on the surface of a nucleated nematic droplet in the three dimensional volume at an early stage. The isosurface is plotted for a fixed isovalue $S = 0.04$. Panel (b) shows the uniaxial order in a x-y plane that slices the three dimensional volume at $z = 20$.

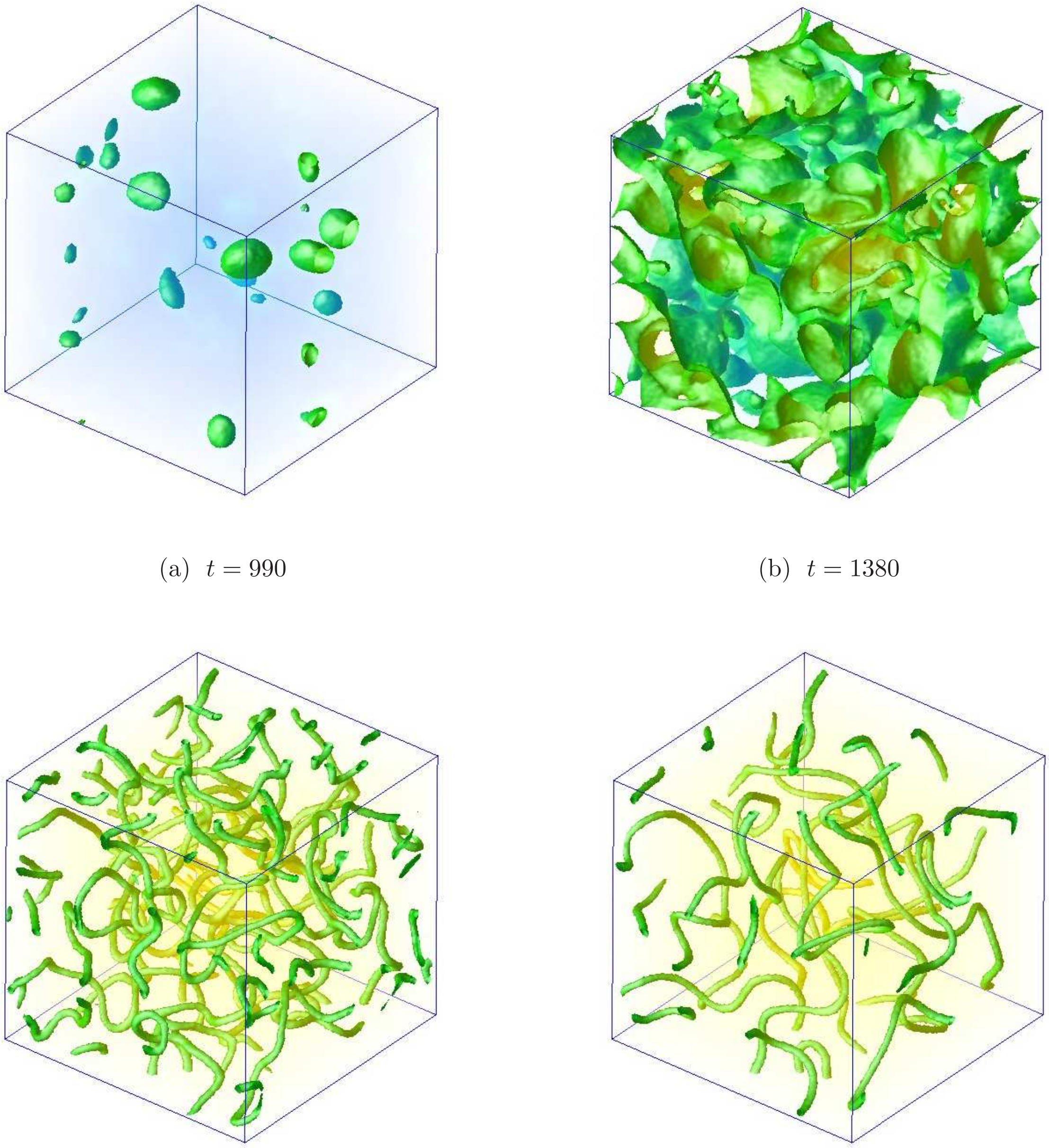

(a) $t = 990$

(b) $t = 1380$

(c) $t = 1860$

(d) $t = 3900$

Figure 6.11: Time evolution of uniaxial order in a three dimensional volume. Panel (a) shows the emergence of uniaxial nematic droplet in the fluctuating isotropic background. Panel (b) shows the coalescence of droplets to form line defects shown in panel (c). The defects at a late of the kinetics is shown in panel (d). The isosurfaces are plotted for the fixed isovalue $S = 0.05$. The numerics is performed upto 3.9×10^3 SRK4 iterations with unit time increment.

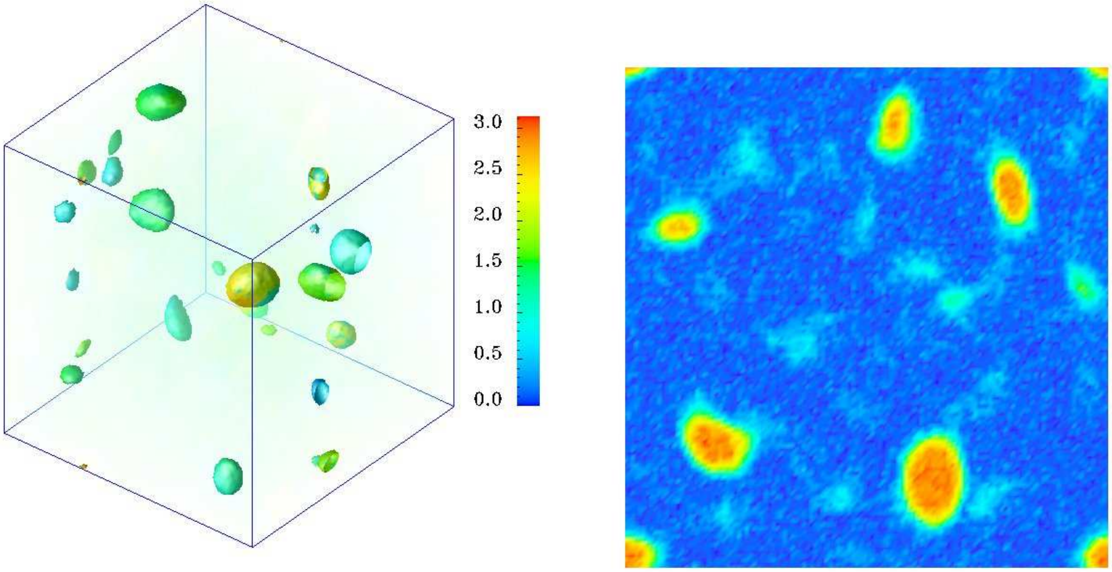

(a) $t = 990$ (b) $t = 1140$

Figure 6.12: Panel (a) shows the uniaxial order and director field on the surface of a nucleated nematic droplet in the three dimensional volume. The isosurface is plotted for the isovalue $S = 0.05$. Panel (b) shows the uniaxial order in a x-y plane that slices the three dimensional volume at $z = 19$.

the other cases, we see the nucleation kinetics followed by a phase ordering kinetics with coalescence of droplets leading to defects which eventually annihilate from the system.

Our central result is the ellipsoidal shape of the droplet conformation in the early stage of nucleation. Fig.(6.12) depicts the local tilt angle θ on the surface of the droplets as well as a slice of the three dimensional volume at a particular value of z in the $z-$axis. We notice defect ellipsoidal droplets with different conformation of the director at the surface of the droplet. We are unable to locate any defect conformation inside or on the surface of the droplet. The ellipsoidal nature of the droplet can be visualized in Fig.[6.12(b)]. Like the two dimensional case, we also notice the first passage time to be slightly higher than the previous case.

6.4 Conclusion

In this chapter we have studied various uniaxial nematic droplet conformation nucleated in an isotropic fluid medium, through a computational study of nucleation kinetics in nematics. We have shown, in the absence of temperature fluctuations, that a uniaxial nematic nuclei with uniform director conformation grows in size, preserving the circular symmetry, if the contribution from anisotropic gradient terms are not incorporated in the Landau-de Gennes theory. This situation breaks down in the more general case, with the emergence of an elliptic nucleus with the long axis of the ellipse oriented along the direction of the director for $\kappa > 0$ while remaining perpendicular to this direction for $\kappa < 0$. We have verified that in the presence of moderate thermal fluctuations, the nucleating uniaxial nematic nuclei grows as in the case of $\kappa = 0$. The first signature of an anomaly in the director configuration is for the $\kappa > 0$ case, where ellipsoidal nuclei grow in size with an integer defect trapped inside. While the droplets coalesce among themselves, these defects last till the late stage of the kinetics until the annihilation process kicks in. We obtain ellipsoidal droplets with uniform director configuration for $\kappa < 0$.

We also present nematic droplet conformations in three dimensions for all three cases. Though we are unable to detect any integer defect inside the ellipsoidal droplet in the case of $\kappa > 0$, we notice an abrupt variation of the director on the surface of the droplet for both positive and negative values of κ.

Chapter 7

Conclusions

This thesis has studied various static and dynamic properties of nematic liquid crystals through accurate numerical methodologies. As examples of the variety of uses our methods can be put to, we address a few central problems in the statics and dynamics of nematics modeled within the Landau-Ginzburg-de Gennes formulation: the static properties of the isotropic-nematic interface, the incorporation of the effects of thermal fluctuations in the TDGL equations for nematics, phase ordering and the dynamics of defects in the spinodal kinetics of uniaxial and biaxial quenches in nematics and the structure of nucleating nematic droplets.

We have shown how a noisy TDGL equation for nematics can be formulated, and described a method-of-lines (MOL) approach and its stochastic variant, the stochastic method of lines. We have illustrated the uses of the MOL approach in solving the tensorial inhomogeneous equations governing the overdamped dynamics of nematics. These calculations make no ad-hoc assumptions and take into account all the degrees of freedom of the tensorial order parameter. We have also developed a highly accurate spectral scheme, benchmarking the algorithm against the scalar problem. We have extended our MOL algorithm for high-performance computational purposes, to run in a parallel cluster. These algorithms make it possible to study the TDGL equations appropriate to nematics in a far more computationally efficient way than any previously reported study.

We have applied the MOL algorithm to integrate the deterministic part of the TDGL equation to study the static properties of the nematic-isotropic interface. We show that in the absence of elastic anisotropy, the classical de Gennes ansatz is valid, while the inclusion of such contributions to the free energy induces *biaxiality* at the interface for any anchoring condition of the director other than homeotropic. By applying spectral methods to solve the nematic equations for a fixed nematic director anchoring in the nematic boundary we have shown that, for oblique nematic anchoring, the local tilt angle linearly interpolates between the interface and nematic boundary, making the interface nonlocal in nature. However, scalar order varies significantly only over a small region in the vicinity of the boundary. Finally, we describe, pictorially, the effects of thermal fluctuation on the roughening of the isotropic-nematic interface. This work can be easily extendable to the study of the capillary wave spectrum induced by thermal fluctuations [62].

In the study of spinodal kinetics in uniaxial and biaxial nematics, we have developed a new defect visualization scheme which enables easy detection and visualization of point and line defects through the alteration of the scalar order with respect to the bulk value in the vicinity of the defects. A numerical test of phase field theories requires the study of the large scale, long time limit of the problem so as to ensure a true scale separation. We have carried out high performance computations with large lattice systems to achieve such a limit. In our study of phase ordering in two dimensional systems within the TDGL framework, we demonstrate dynamical scaling with a length scale growing as $t^{1/2}$ at late times. Our numerics detects a rapid crossover in the dynamics at early times, with a diffusive $t^{1/2}$ growth at early times arising from order parameter magnitude evolution changes crossing over into a late-time regime dominated by the diffusion and annihilation of topological defects. This physics is absent in earlier simulations of hard-spin models of nematics. We regain a diffusive regime at the final stage of the dynamics [13]. This study helps us to settle the question of the dynamical exponents in both phases in a more definitive way than previous studies [13, 77, 25]. We have demonstrated the effect of temperature fluctuations on the dynamics of point defects in uniaxial nematics. In general, our computation of dynamic properties in the presence of fluctuations can be used to investigate a wide range of phenomena in both $O(n)$ models and uniaxial nematics [45].

Defect dynamics is richer in three dimensions as opposed to two dimensions. For uniaxial nematic system, defect lines can exchange segments while interacting, leading to loops which contract and vanish from the system. Interesting phenomena have been predicted for biaxial nematics where, due to the underlying non-Abelian structure of the group, topological restrictions have been predicted to prevent defects of different classes from crossing, possibly leading to novel glassy states. Within our calculations, we do not observe a jamming of defect lines in quenched biaxial system. However, we clearly see defect-segment exchange in both uniaxial and biaxial nematics within our simulations. Our work can easily be extended to include higher order derivative in the free energy, thus achieving distinct energy channels for defects of different homotopy classes. Work in this direction is in progress.

To study the shape and director field structure in the nucleation of nematic droplets in an isotropic environment, we have solved the deterministic and fluctuating TDGL equation in the nucleation regime. In the absence of thermal fluctuations, we have shown how the contribution from the elastic anisotropy changes the shape of the droplet from an initially circular to an ellipsoidal shape in the growth stage. Without elastic anisotropic the circular symmetry of the droplet is preserved. Our methods are more general than methods used in previous calculations, where surface terms are introduced to account for the elastic anisotropy in an ad-hoc way [61]. Our theory automatically guarantees such contributions from the anisotropic gradients in the LGdG free energy functional.

For nucleation in two dimensions, a positive contribution to the elastic anisotropy not only changes the shape of the droplet, but also creates an integer charged defect inside the droplet. For a negative contribution, we obtain elliptical droplets with uniform director conformation inside the droplets. We have also studied nucleation in three dimensions. We notice an abrupt variation of the director on the surface of droplet but are unable to detect any integer defect inside the ellipsoidal droplet in the presence of a positive contribution to the anisotropic surface energy. Work aimed at detecting and classifying defects in three dimensions is in progress.

Appendix A

Nematodynamic equations

As a symmetrical tensor $Q_{\alpha\beta}$ can be diagonalized at any given point by choosing the principal axes (in other words taking a similarity transform so that the matrix become diagonal) which does not diagonalize for the other points, the equations are needed to be projected onto the tensorial basis $T^i_{\alpha\beta}$ to give a set of equations for the independent components a_i,

$$\partial_t a_i = -\Gamma\ [(A + CTrQ^2)a_i + (B + 6E'TrQ^3)T^i_{\alpha\beta}\overline{Q^2_{\alpha\beta}} - L_1\nabla^2 a_i - L_2\ \overline{T^i_{\alpha\beta}T^j_{\beta\gamma}\partial_\alpha\partial_\gamma a_j}\ ]. \quad \text{(A.1)}$$

Using the orthonormality of the basis tensors $T^i_{\alpha\beta}T^j_{\beta\alpha} = \delta_{ij}$, this can be expanded to the set of five equations,

$$\begin{aligned}\partial_t a_1 \quad = \quad & -\Gamma\ [(A + CTrQ^2)a_1 + (B + 6E'TrQ^3)\frac{1}{\sqrt{6}}(a_1^2 - a_2^2 - a_3^2 + \frac{a_4^2}{2} + \frac{a_5^2}{2}) - \\ & L_1\nabla^2 a_1 - L_2(\frac{1}{6}\nabla^2 a_1 + \frac{1}{2}\partial_z^2 a_1 + \frac{1}{\sqrt{12}}\{(\partial_y^2 - \partial_x^2)a_2 + \partial_x\partial_z a_4 + \partial_y\partial_z a_5\} - \\ & \frac{1}{\sqrt{3}}\partial_x\partial_y a_3)], \end{aligned} \qquad \text{(A.2)}$$

$$\begin{aligned}\partial_t a_2 \quad = \quad & -\Gamma\ [(A + CTrQ^2)a_2 + (B + 6E'TrQ^3)(-\sqrt{\frac{2}{3}}a_1 a_2 + \frac{a_4^2}{\sqrt{8}} - \frac{a_5^2}{\sqrt{8}}) - \\ & L_1\nabla^2 a_2 - L_2\{\frac{1}{\sqrt{12}}(\partial_y^2 - \partial_x^2)a_1 + \frac{1}{2}((\partial_x^2 + \partial_y^2)a_2 + \partial_x\partial_z a_4 - \partial_y\partial_z a_5)\}], \end{aligned} \quad \text{(A.3)}$$

$$\begin{aligned}\partial_t a_3 \quad = \quad & -\Gamma\ [(A + CTrQ^2)a_3 + (B + 6E'TrQ^3)(-\frac{2a_1 a_3}{\sqrt{6}} + \frac{a_4 a_5}{\sqrt{2}}) - \\ & L_1\nabla^2 a_3 - L_2\{-\frac{1}{\sqrt{3}}\partial_x\partial_y a_1 + \frac{1}{2}((\partial_x^2 + \partial_y^2)a_3 + \partial_y\partial_z a_4 + \partial_x\partial_z a_5)\}], \end{aligned} \qquad \text{(A.4)}$$

$$\begin{aligned}\partial_t a_4 \quad = \quad & -\Gamma\ [(A + CTrQ^2)a_4 + (B + 6E'TrQ^3)(\frac{a_1 a_4}{\sqrt{6}} + \frac{a_2 a_4}{\sqrt{2}} + \frac{a_3 a_5}{\sqrt{2}}) - \\ & L_1\nabla^2 a_4 - L_2\{\frac{1}{\sqrt{12}}\partial_x\partial_z a_1 + \frac{1}{2}((\partial_x^2 + \partial_z^2)a_4 + \partial_x\partial_z a_2 + \partial_y\partial_z a_3 + \\ & \partial_x\partial_y a_5)\}], \end{aligned} \qquad \text{(A.5)}$$

$$\begin{aligned}\partial_t a_5 &= -\Gamma\ [(A + CTrQ^2)a_5 + (B + 6E'TrQ^3)(\frac{a_1a_5}{\sqrt{6}} + \frac{a_3a_4}{\sqrt{2}} - \frac{a_2a_5}{\sqrt{2}}) - \\ &\quad L_1\nabla^2 a_5 - L_2\{\frac{1}{\sqrt{12}}\partial_y\partial_z a_1 + \frac{1}{2}((\partial_y^2 + \partial_z^2)a_5 - \partial_y\partial_z a_2 + \partial_x\partial_z a_3 + \\ &\quad \partial_x\partial_y a_4)\}]. \end{aligned} \tag{A.6}$$

We now present the Jacobian matrix (for $L_2 = 0$), for this purpose, we use Lexicographic projection for the three dimensional problem, defined as

$$m = p + 5i + 5jL_x + 5kL_xL_y \tag{A.7}$$

where, $p = 1, \cdots, 5$; i, j, and k varies from 0 to $L_x - 1$, $L_y - 1$ and $L_z - 1$ respectively. The Jacobian matrix is defined as,

$$J^{\{p\}}_{m;n} = \frac{\partial_t a^{\{p\}}_m}{\partial a^{\{q\}}_n}\delta_{pq} \tag{A.8}$$

consist of two contribution from local and non-local part of the nematodynamic equation. From Eq.(A.2, $\cdots$, A.6), the local part is,

$$\begin{aligned} J^{\{1\}}_{m;n}(\texttt{local}) &= -\Gamma\ [(A + CTrQ^2) + 2Ca_1^2 + \frac{2}{\sqrt{6}}(B + 6E'TrQ^3)a_1 + \\ &\quad \frac{E'}{\sqrt{6}}(a_1^2 - a_2^2 - a_3^2 + \frac{a_4^2}{2} + \frac{a_5^2}{2})\{\sqrt{54}a_1^2 - \sqrt{\frac{27}{2}}(2a_2^2 + 2a_3^2 - \\ &\quad a_4^2 - a_5^2)\}]\delta_{mn}, \end{aligned} \tag{A.9}$$

$$\begin{aligned} J^{\{2\}}_{m;n}(\texttt{local}) &= -\Gamma\ [(A + CTrQ^2) + 2Ca_2^2 - \sqrt{\frac{2}{3}}(B + 6E'TrQ^3)a_2 + \\ &\quad E'(\sqrt{\frac{2}{3}}a_1a_2 - \frac{a_4^2}{\sqrt{8}} + \frac{a_5^2}{\sqrt{8}})\{\sqrt{216}a_1a_2 - \sqrt{\frac{9}{2}}(a_4^2 - a_5^2)\}]\delta_{mn}, \end{aligned} \tag{A.10}$$

$$\begin{aligned} J^{\{3\}}_{m;n}(\texttt{local}) &= -\Gamma\ [(A + CTrQ^2) + 2Ca_3^2 - \frac{2}{\sqrt{6}}(B + 6E'TrQ^3)a_1 + \\ &\quad +E'(\sqrt{\frac{2}{3}}a_1a_3 - \sqrt{\frac{1}{2}}a_4a_5)(\sqrt{216}a_1a_3 - \sqrt{162}a_4a_5)]\delta_{mn}, \end{aligned} \tag{A.11}$$

$$\begin{aligned} J^{\{4\}}_{m;n}(\texttt{local}) &= -\Gamma\ [(A + CTrQ^2) + 2Ca_4^2 + (\frac{1}{\sqrt{6}}a_1 + \frac{1}{\sqrt{2}}a_2)(B + 6E'TrQ^3) + \\ &\quad E'(\frac{1}{\sqrt{6}}a_1a_4 + \frac{1}{\sqrt{2}}a_2a_4 + \frac{1}{\sqrt{2}}a_3a_5)\{\sqrt{54}a_1a_4 + \sqrt{\frac{81}{2}}(2a_3a_5 + \\ &\quad 2a_2a_4)\}]\delta_{mn}, \end{aligned} \tag{A.12}$$

$$\begin{aligned} J^{\{5\}}_{m;n}(\texttt{local}) &= -\Gamma\ [(A + CTrQ^2) + 2Ca_5^2 + (\frac{1}{\sqrt{6}}a_1 - \frac{1}{\sqrt{2}}a_2)(B + 6E'TrQ^3) + \\ &\quad E'(\frac{1}{\sqrt{6}}a_1a_5 + \frac{1}{\sqrt{2}}a_3a_4 - \frac{1}{\sqrt{2}}a_2a_5)\{\sqrt{54}a_1a_5 + \sqrt{\frac{81}{2}}(2a_3a_4 - \\ &\quad 2a_2a_5)\}]\delta_{mn} \end{aligned} \tag{A.13}$$

In the finite difference approximation, the non-local part of the nematodynamic equation takes,

$$\partial_t a^{\{p\}}_m = \Gamma L_1[a^{\{p\}}_{m+5} + a^{\{p\}}_{m-5} + a^{\{p\}}_{m+5L_x} + a^{\{p\}}_{m-5L_x} + a^{\{p\}}_{m+5L_xL_y} + a^{\{p\}}_{m-5L_xL_y} - 6a^{\{p\}}_m] \tag{A.14}$$

and the Jacobian matrix becomes,

$$\begin{aligned} J^{\{p\}}_{m;n}(\texttt{nonlocal}) &= \Gamma L_1[\delta_{m+5;n} + \delta_{m-5;n} + \delta_{m+5L_x;n} + \delta_{m-5L_x;n} + \delta_{m+5L_xL_y;n} + \\ &\quad \delta_{m-5L_xL_y;n} - 6\delta_{m;n}]\delta_{pq} \end{aligned} \tag{A.15}$$

Appendix B

Equation for the isotropic-nematic interface

The nematic equation in at the long time limit are defined in Eq.(4.6) in the basis of the five set of "a". In the problems, we always consider a planar interface, where the only variation of the order parameter $\mathbf{Q}$ can happen is in the z direction. So, all the derivatives consisting of ∂_x, ∂_y of any order gives a vanishing contribution. The elastic contribution results only from the derivatives of ∂_z of any order.

The equation for the interface then expands into the set of equations given as

$$\begin{aligned}
(A+CTrQ^2)a_1+\frac{B}{\sqrt{6}}(a_1^2-a_2^2-a_3^2+\frac{a_4^2}{2}+\frac{a_5^2}{2}) &= (L_1+\frac{2}{3}L_2)\,\partial_z^2 a_1, && \text{(B.1)}\\
(A+CTrQ^2)a_2+B(-\sqrt{\frac{2}{3}}a_1a_2+\frac{a_4^2}{\sqrt{8}}-\frac{a_5^2}{\sqrt{8}}) &= L_1\partial_z^2 a_2, && \text{(B.2)}\\
(A+CTrQ^2)a_3+B(-\sqrt{\frac{2}{3}}a_1a_3+\frac{a_4a_5}{\sqrt{2}}) &= L_1\partial_z^2 a_3, && \text{(B.3)}\\
(A+CTrQ^2)a_4+B(\frac{a_1a_4}{\sqrt{6}}+\frac{a_2a_4}{\sqrt{2}}+\frac{a_3a_5}{\sqrt{2}}) &= (L_1+\frac{L_2}{2})\,\partial_z^2 a_4, && \text{(B.4)}\\
(A+CTrQ^2)a_5+B(\frac{a_1a_5}{\sqrt{6}}+\frac{a_3a_4}{\sqrt{2}}-\frac{a_2a_5}{\sqrt{2}}) &= (L_1+\frac{L_2}{2})\,\partial_z^2 a_5. && \text{(B.5)}
\end{aligned}$$

The boundary conditions for the uniaxial nematic side is fixed from the definition of the order parameter $Q_{\alpha\beta}$ as

$$\frac{S}{2}(3n_\alpha n_\beta-\delta_{\alpha\beta})=\Sigma_i a_i T^i_{\alpha\beta}, \qquad \text{(B.6)}$$

which results into the condition,

$$\begin{aligned}
(a_1)_{\texttt{nem}} &= -\sqrt{\frac{3}{32}}S[3(n_x^2+n_y^2-n_z^2)-1], && \text{(B.7)}\\
(a_2)_{\texttt{nem}} &= \frac{3}{\sqrt{8}}S(n_x^2-n_y^2), && \text{(B.8)}\\
(a_3)_{\texttt{nem}} &= \frac{3}{\sqrt{2}}Sn_xn_y, && \text{(B.9)}\\
(a_4)_{\texttt{nem}} &= \frac{3}{\sqrt{2}}Sn_xn_z, && \text{(B.10)}\\
(a_5)_{\texttt{nem}} &= \frac{3}{\sqrt{2}}Sn_yn_z. && \text{(B.11)}
\end{aligned}$$

Appendix C

Index of animations

The enclosed CD-ROM contains the presentation of some of the animations we develop in the numerical simulation of nematic liquid crystal, partly described in the thesis. Some of them can be viewed in the web address:

http://www.youtube.com/view_play_list?p=7F62606B554B63A6 .

- Animation-I : align-BN-1D.avi

  This short presentation shows the numerical simulation of the dynamics of the nematic director and co-director, while thermally cooled from an isotropic fluid phase through a biaxial nematic quench. The nematic director and co-director is shown as double-arrowed vectors with false colours to signify it's non-directional nature. This numerics is performed on a one dimensional lattice of size 32, while the molecules can rotate in three Cartesian directions.

- Animation-II : phaseorder-UN-2D.avi

  The computer experiment of spinodal kinetics of quenched uniaxial nematics from isotropic fluid phase is shown in two dimensions. The uniaxial degree of alignment and the director field is been superimposed. Point defect - anti defect pairs appear throughout the simulation grid, which eventually annihilate from the uniaxial nematic phase. The parameters are as enlisted in the Table 5.1.

- Animation-III : phaseorder-UN-2D-Sch.avi

  The schlieren textures that appear as the intensity of light scattered between a crossed polarizer is shown from a numerical simulation of spinodal kinetics in quenched uniaxial nematics from isotropic fluid phase in two dimensions. Defects with 2-brush and 4-brushes appear throughout the system. Annihilation of 2-brush defects is seen throughout the numerical time.

- Animation-IV : phaseorder-BN-2D.avi

  The computer experiment of spinodal kinetics of quenched biaxial nematics from isotropic fluid phase is shown in two dimensions. The uniaxial degree of alignment and the director field is been superimposed. Point defect - anti defect pairs from different homotopy classes appear throughout the simulation grid, which eventually annihilate between their respective classes.

- Animation-V : phaseorder-BN-2D-Sch.avi

  The schlieren textures that appear as the intensity of light scattered between a crossed polarizer is shown from a numerical simulation of spinodal kinetics in quenched biaxial nematics from isotropic fluid phase in two dimensions. Defects with 2-brush and 4-brushes appear throughout the system. Annihilation of 2-brush defects is seen throughout the numerical time.

- Animation-VI : phaseorder-UN-3D.avi

  The computer experiment of spinodal kinetics of quenched uniaxial nematics from isotropic fluid phase is shown in three dimensions. Line defect - anti defect pairs appear throughout the simulation grid, which eventually annihilate from the uniaxial nematic phase by intercommutation of segment and forming contractile loops.

- Animation-VII : phaseorder-BN-3D.avi

  The computer experiment of spinodal kinetics of quenched biaxial nematics from isotropic fluid phase is shown in three dimensions. Line defect - anti defect pairs from different classes appear throughout the simulation grid, which eventually annihilate within the same class from the biaxial nematic phase by intercommutation of segment and forming contractile loops.

- Animation-VIII : nucl-2D-L2zero.avi

  This small animation presents the nucleation of uniaxial nematic droplets in the isotropic environment in the absence of κ. The director configuration is superimposed on the degree of uniaxial order. Spherical droplets grow in size and while coalesce form defects which eventually annihilate from the simulation box. The parameters are as enlisted in the Table 6.1.

- Animation-IX : nucl-2D-L2pos.avi

  This animation presents the nucleation of uniaxial nematic droplets in the isotropic environment in the presence of a positive contribution of κ. The director configuration is superimposed on the degree of uniaxial order. Ellipsoidal droplets grow in size and before coalescence form complex geometry. Bubble coalescence does not generate any defect.

- Animation-X : nucl-2D-L2pos-Sch.avi

  This animation presents the schlieren texture corresponding to the results of the previous animation. The growth of droplets with a 4-brush defects inside are clearly identified. Although the droplets coalesce, but the structure of the defect persists upto a late stage of the dynamics while at the late stage the fluctuation in nematic phase prevails.

- Animation-XI : nucl-2D-L2neg.avi

  This small animation presents the nucleation of uniaxial nematic droplets in the isotropic environment in the presence of a negative contribution of κ. The director configuration is superimposed on the degree of uniaxial order. Ellipsoidal droplets grow in size and while coalesce form defects which eventually annihilate from the simulation box.

- Animation-XII : nucl-3D-L2zero.avi

  The computer experiment of nucleation kinetics into the nematic phase from isotropic fluid phase is shown in three dimensions. Spherical droplets form which coalesce and form line defects. These eventually annihilate from the uniaxial nematic phase by making contractile loops.

- Animation-XIII : nucl-3D-L2pos.avi

  The computer experiment of nucleation kinetics into the nematic phase from isotropic fluid phase is shown in three dimensions. Ellipsoidal droplets form which coalesce and form line defects. These eventually annihilate from the uniaxial nematic phase by making contractile loops.

- Animation-XIV : theta-UN-3D-L2pos.avi

  This shows the dynamics of the local tilt angle θ on the surface of the nematic droplet for the previous animation. Notice the different colours on the surface which signify an abrupt change in the direction of the director.

- Animation-XV : nucl-3D-L2neg.avi

  The computer experiment of nucleation kinetics into the nematic phase from isotropic fluid phase is shown in three dimensions. Ellipsoidal droplets form which coalesce and form line defects. These eventually annihilate from the uniaxial nematic phase by making contractile loops.

- Animation-XVI : theta-UN-3D-L2neg.avi

  This shows the dynamics of the local tilt angle θ on the surface of the nematic droplet for the previous animation. Notice the different colours on the surface which signify an abrupt change in the direction of the director.

- Animation-XVII : phaseorder-UN-2D-wn.avi

  The computer simulation of the phase ordering kinetics of quenched uniaxial nematic phase from the isotropic fluid phase in the presence of thermal fluctuation.

- Animation-XVIII : allencahn-3D.avi

  The computer simulation of the Allen-Cahn equation for a scalar field with two saturation values ± 1 with the interface in between. Note the pinch off effect as well as the sudden disappearance of the isosurfaces signifying of the non-conserved property of the order parameter field.

Bibliography

[1] M. Abramowitz and I. A. Stegun. *Handbook of Mathematical Functions: with Formulas, Graphs, and Mathematical Tables*. Dover, 1964.

[2] M. S. Al-Barwani and M. P. Allen. Isotropic-nematic interface of soft spherocylinders. *Phys. Rev. E*, 62(5):6706–6710, Nov 2000. `http://dx.doi.org/10.1103/PhysRevE.62.6706`.

[3] M. P. Allen. Molecular simulation and theory of the isotropic-nematic interface. *The Journal of Chemical Physics*, 112:5447, 2000. `http://dx.doi.org/10.1063/1.481112`.

[4] D. Allender and L. Longa. Landau–de gennes theory of biaxial nematics reexamined. *Phys. Rev. E*, 78(1):011704, Jul 2008. `http://dx.doi.org/10.1103/PhysRevE.78.011704`.

[5] S. Auer and D. Frenkel. Numerical simulation of crystal nucleation in colloids. *Adv. Polym. Sci.*, 173:149–207, 2005. `http://dx.doi.org/10.1007/b99429`.

[6] S. Balay, J. Brown, K. Buschelman, W. D. Gropp, D. Kaushik, M. G. Knepley, L. C. McInnes, B. F. Smith, and H. Zhang. PETSc Web page, 2011. `http://www.mcs.anl.gov/petsc`.

[7] M. A. Bates and C. Zannoni. A molecular dynamics simulational study of the nematic-isotropic interface of a Gay-Berne liquid crystal. *Chemical Physics Letters*, 280:40, 1997. `http://dx.doi.org/10.1016/S0009-2614(97)01089-0`.

[8] E. Berggren, C. Zannoni, C. Chiccoli, P. Pasini, and F. Semeria. Computer simulations of nematic droplets with bipolar boundary conditions. *Phys. Rev. E*, 50(4):2929–2939, Oct 1994. `http://dx.doi.org/10.1103/PhysRevE.50.2929`.

[9] J. D. Bernal and I. Fankuchen. X-ray and crystallographic studies of plant virus preparations. *J. Gen. Physiol.*, 25:111, Mar 1941. `http://www.ncbi.nlm.nih.gov/pmc/articles/PMC2142030/`.

[10] A. K. Bhattacharjee, G. I. Menon, and R. Adhikari. Numerical method of lines for the relaxational dynamics of nematic liquid crystals. *Phys. Rev. E*, 78:026707, 2008. `http://dx.doi.org/10.1103/PhysRevE.78.026707`.

[11] A. K. Bhattacharjee, G. I. Menon, and R. Adhikari. Fluctuating dynamics of nematic liquid crystals using the stochastic method of lines. *J. Chem. Phys.*, 133:044112, 2010. `http://dx.doi.org/10.1063/1.3455206`.

[12] A. J. Bray. Theory of phase ordering kinetics. *Adv. Phys.*, 43:357, 1994. `http://arxiv.org/abs/cond-mat/9501089`.

[13] A. J. Bray and S. Puri. Asymptotic structure factor and power-law tails for phase ordering in systems with continuous symmetry. *Phys. Rev. Lett.*, 67(19):2670–2673, Nov 1991. `http://dx.doi.org/10.1103/PhysRevLett.67.2670`.

[14] A. J. Bray, S. Puri, R. E. Blundell, and A. M. Somoza. Structure factor for phase ordering in nematic liquid crystals. *Phys. Rev. E*, 47(4):R2261–R2264, Apr 1993. `http://dx.doi.org/10.1103/PhysRevE.47.R2261`.

[15] A. Callan-Jones, R. A. Pelcovits, V. Slavin, S. Zhang, D. Laidlaw, and G. Loriot. Simulation and visualization of topological defects in nematic liquid crystals. *Phys. Rev. E*, 74:061701, 2006. `http://dx.doi.org/10.1103/PhysRevE.74.061701`.

[16] S. Chandrasekhar. Surface tension of liquid crystals. *Molecular Crystals and Liquid Crystals*, 2:71 – 80, Dec 1966. `http://dx.doi.org/10.1080/15421406608083061`.

[17] S. Chandrasekhar, G. G. Nair, D. S. S. Rao, S. K. Prasad, K. Praefcke, and D. Blunk. A thermotropic biaxial nematic liquid crystal. *Current Science*, 75:1042–1046, 1998. `http://www.ias.ac.in/j_archive/currsci/75/10/1042-1046/viewpage.html`.

[18] Z. Y. Chen. Biaxial effect at an isotropic-nematic interface. *Phys. Rev. E*, 47(5):3765–3767, May 1993. `http://dx.doi.org/10.1103/PhysRevE.47.3765`.

[19] Z. Y. Chen and J. Noolandi. Numerical solution of the onsager problem for an isotropic-nematic interface. *Phys. Rev. A*, 45(4):2389–2392, Feb 1992. `http://dx.doi.org/10.1103/PhysRevA.45.2389`.

[20] C. Chiccoli, I. Feruli, O. D. Lavrentovich, P. Pasini, S. V. Shiyanovskii, and C. Zannoni. Topological defects in schlieren textures of biaxial and uniaxial nematics. *Phys. Rev. E*, 66(3):030701, Sep 2002. `http://dx.doi.org/10.1103/PhysRevE.66.030701`.

[21] I. Chuang, R. Durrer, N. Turok, and B. Yurke. Cosmology in the laboratory:defect dynamics in liquid crystals. *Science*, 251(4999):1336–1342, Mar 1991. `http://dx.doi.org/10.1126/science.251.4999.1336`.

[22] A. Cuetos and M. Dijkstra. Kinetic pathways for the isotropic-nematic phase transition in a system of colloidal hard rods: A simulation study. *Phys. Rev. Lett.*, 98:095701, Feb 2007. `http://dx.doi.org/10.1103/PhysRevLett.98.095701`.

[23] P. G. de Gennes. Short range order effects in the isotropic phase of nematics and cholesterics. *Molecular Crystals and Liquid Crystals*, **12**:193–214, 1971. `http://dx.doi.org/10.1080/15421407108082773`.

[24] P. G. de Gennes and J. Prost. *The Physics of Liquid Crystals*. Clarendon Press, Oxford, second edition, 1993.

[25] C. Denniston, E. Orlandini, and J. M. Yeomans. Phase ordering in nematic liquid crystals. *Phys. Rev. E*, 64(2):021701, Jul 2001. `http://dx.doi.org/10.1103/PhysRevE.64.021701`.

[26] S. Dutta and S. K. Roy. Dynamical scaling in two-dimensional quenched uniaxial nematic liquid crystals. *Phys. Rev. E*, 71(2):026119, Feb 2005. `http://dx.doi.org/10.1103/PhysRevE.71.026119`.

[27] M. G. et al. GNU Scientific Library Reference Manual (3rd Ed.). `http://www.gnu.org/software/gsl/`.

[28] S. Faetti and V. Palleschi. Molecular orientation and anchoring energy at the nematic-isotropic interface of 7cb. *J. Physique Lett.*, 45:313, 1944. `http://dx.doi.org/10.1051/jphyslet:01984004507031300`.

[29] B. Fornberg. Calculation of weights in finite difference formulas. *SIAM Review*, 40(3):685–691, 1998. `http://www.jstor.org/stable/2653239`.

[30] G. Rienäcker, M. Kröger and S. Hess. Chaotic and regular shear-induced orientational dynamics of nematic liquid crystals. *Physica A: Statistical Mechanics and its Applications*, 315:537–568, 2002. `http://dx.doi.org/10.1016/S0378-4371(02)01008-7`.

[31] C. W. Gardiner. *Handbook of Stochastic Methods*. Springer, Berlin, 1983.

[32] E. F. Gramsbergen, L. Longa, and W. H. de Jeu. Landau theory of the nematic-isotropic phase transition. *Physics Reports*, **135**:195–257, 1986. `http://dx.doi.org/10.1016/0370-1573(86)90007-4`.

[33] C. Herring. Some theorems on the free energies of crystal surfaces. *Phys. Rev.*, 82(1):87–93, Apr 1951. `http://dx.doi.org/10.1103/PhysRev.82.87`.

[34] R. Holyst and A. Poniewierski. Director orientation at the nematic-phase–isotropic-phase interface for the model of hard spherocylinders. *Phys. Rev. A*, 38(3):1527–1533, Aug 1988. `http://dx.doi.org/10.1103/PhysRevA.38.1527`.

[35] S. M. Kamil, A. K. Bhattacharjee, R. Adhikari, and G. I. Menon. Biaxiality at the isotropic-nematic interface with planar anchoring. *Phys. Rev. E*, 80:041705, 2009. `http://dx.doi.org/10.1103/PhysRevE.80.041705`.

[36] S. M. Kamil, A. K. Bhattacharjee, R. Adhikari, and G. I. Menon. The isotropic-nematic interface with an oblique anchoring condition. *J. Chem. Phys.*, 131:174701, 2009. `http://dx.doi.org/10.1063/1.3253702`.

[37] T. W. B. Kibble. Topology of cosmic domains and strings. *J. Phys. A*, 9:1387, 1976. `http://dx.doi.org/10.1088/0305-4470/9/8/029`.

[38] M. Kleman and O. Lavrentovich. *Soft Matter Physics: An Introduction*. Springer Verlag, New York, 2002.

[39] C. Kobdaj and S. Thomas. Nonabelian vortices. *Nucl. Phys. B*, 413:689, 1994. http://dx.doi.org/10.1016/0550-3213(94)90008-6.

[40] P. E. Lammert, D. S. Rokhsar, and J. Toner. Topology and nematic ordering. i. a gauge theory. *Phys. Rev. E*, 52(2):1778–1800, Aug 1995. http://dx.doi.org/10.1103/PhysRevE.52.1778.

[41] D. Langevin and M. A. Bouchiat. Molecular order and surface tension for the nematic-isotropic interface of MBBA, deduced from light reflectivity and light scattering measurements. *Mol. Cryst. Liq. Cryst.*, 22:331, 1973. http://dx.doi.org/10.1080/15421407308083354.

[42] R. J. LeVeque. *Finite Volume Methods for Hyperbolic Problems*. Cambridge University Press, 2002.

[43] R. J. LeVeque. *Finite Difference Methods for Ordinary and Partial Differential Equations, Steady State and Time Dependent Problems*. SIAM, 2007.

[44] O. A. Liskovets. The methods of lines. *J. Diff. Eqs.*, 1:1308, 1965.

[45] F. Liu and G. F. Mazenko. Defect-defect correlation in the dynamics of first-order phase transitions. *Phys. Rev. B*, 46(10):5963–5971, Sep 1992. http://dx.doi.org/10.1103/PhysRevB.46.5963.

[46] G. Maruyama. Continuous markov processes and stochastic equations. *Rend. Circolo. Math. Palermo*, 4:48–90, 1955. http://dx.doi.org/10.1007/BF02846028.

[47] A. J. McDonald, M. P. Allen, and F. Schmid. Surface tension of the isotropic-nematic interface. *Phys. Rev. E*, 63(1):010701, Dec 2000. http://dx.doi.org/10.1103/PhysRevE.63.010701.

[48] S. Meiboom, J. P. Sethna, P. W. Anderson, and W. F. Brinkman. Theory of the blue phase of cholesteric liquid crystals. *Phys. Rev. Lett.*, 46:1216–1219, May 1981.

[49] N. D. Mermin. The topological theory of defects in ordered media. *Rev. Mod. Phys.*, 51(3):591–648, Jul 1979. http://dx.doi.org/10.1103/RevModPhys.51.591.

[50] G. N. Milstein. *Numerical integration of stochastic differential equations*. Kluwer, London, 1995.

[51] C. D. Modes, M. Warner, C. L. van Oosten, and D. Corbett. Anisotropic response of glassy splay-bend and twist nematic cantilevers to light and heat. *Phys. Rev. E*, 82:041111, Oct 2010. http://link.aps.org/doi/10.1103/PhysRevE.82.041111.

[52] B. G. Moore and W. E. McMullen. Isotropic-nematic interface of hard spherocylinders : Beyond the square-gradient approximation. *Phys. Rev. A*, 42:6042, 1990. `http://dx.doi.org/10.1103/PhysRevA.42.6042`.

[53] P. D. Olmsted and P. Goldbart. Theory of the nonequilibrium phase transition for nematic liquid crystals under shear flow. *Phys. Rev. A*, 41(8):4578–4581, Apr 1990. `http://dx.doi.org/10.1103/PhysRevA.41.4578`.

[54] M. Patra and M. Karttunen. Stencils with isotropic discretization error for differential operators. *Numerical Methods for Partial Differential Equations*, 22:936–953, Nov 2005. `http://dx.doi.org/10.1002/num.20129`.

[55] H. Pleiner and H. Brand. Light scattering in nematic liquid crystals in a nonequilibrium steady state. *Phys. Rev. A*, 27(2):1177–1183, Feb 1983. `http://dx.doi.org/10.1103/PhysRevA.27.1177`.

[56] V. Popa-Nita and T. J. Sluckin. Kinetics of the nematic-isotropic interface. *J. Phys. II (France)*, **6**:873–884, 1996. `http://dx.doi.org/10.1051/jp2:1996216`.

[57] V. Popa-Nita, T. J. Sluckin, and A. A. Wheeler. Statics and kinetics at the nematic-isotropic interface: Effects of biaxiality. *J. Phys. II (France)*, **7**:1225–1243, 1997. `http://dx.doi.org/10.1051/jp2:1997183`.

[58] N. V. Priezjev and R. A. Pelcovits. Coarsening dynamics of biaxial nematic liquid crystals. *Phys. Rev. E*, 66(5):051705, Nov 2002. `http://dx.doi.org/10.1103/PhysRevE.66.051705`.

[59] P. Prinsen and P. van der Schoot. Shape and director-field transformation of tactoids. *Phys. Rev. E*, 68(2):021701, Aug 2003. `http://dx.doi.org/10.1103/PhysRevE.68.021701`.

[60] P. A. Pullarkat. New defect structures in liquid crystals. *Ph.D. Thesis*, 1998. `http://dspace.rri.res.in/handle/2289/3515`.

[61] A. Rapini and M. J. Papoular. *J. Phys. (Paris)*, Colloq. 30:C4–54, 1969.

[62] F. Schmid, G. Germano, S. Wolfsheimer, and T. Schilling. Fluctuating interfaces in liquid crystals. *Macromolecular Symposia*, 252(4):110–118, June 2007. `http://dx.doi.org/10.1002/masy.200750611`.

[63] N. Schopohl and T. J. Sluckin. Defect core structure in nematic liquid crystals. *Phys. Rev. Lett.*, 59(22):2582–2584, Nov 1987. `http://dx.doi.org/10.1103/PhysRevLett.59.2582`.

[64] A. K. Sen and D. E. Sullivan. Landau de gennes theory of wetting and orientational transitions at a nematic-liquid substrate interface. *Phys. Rev. A*, 35(3):1391–1403, Feb 1987. `http://dx.doi.org/10.1103/PhysRevA.35.1391`.

[65] A. Shinozaki and Y. Oono. Spinodal decomposition in 3-space. *Phys. Rev. E*, 48(4):2622–2654, Oct 1993. `http://dx.doi.org/10.1103/PhysRevE.48.2622`.

[66] A. Sonnet, A. Kilian, and S. Hess. Alignment tensor versus director: Description of defects in nematic liquid crystals. *Phys. Rev. E*, 52(1):718–722, Jul 1995. `http://dx.doi.org/10.1103/PhysRevE.52.718`.

[67] R. Stratonovich. Fluctuations in liquid crystals near the liquid-nematic phase transition. *Sov.Phys.JETP*, 70:1290–1299, April 1976.

[68] U. Tkalec, M. Ravnik, S. Čopar, S. Žumer, and I. Muševic. Reconfigurable knots and links in chiral nematic colloids. *Science*, 333(6038):62–65, 2011. `http://dx.doi.org/10.1126/science.1205705`.

[69] H. Toyoki. Cell dynamics simulation for the phase ordering of nematic liquid crystals. *Phys. Rev. E*, 47(4):2558–2561, Apr 1993. `http://dx.doi.org/10.1103/PhysRevE.47.2558`.

[70] L. N. Trefethen. *Spectral Methods in Matlab.* SIAM, 2000.

[71] E. Velasco, L. Mederos, and D. E. Sullivan. Density-functional study of the nematic-isotropic interface of hard spherocylinders. *Phys. Rev. E*, 66:021708, 2002. `http://dx.doi.org/10.1103/PhysRevE.66.021708`.

[72] R. L. C. Vink and T. Schilling. Interfacial tension of the isotropic-nematic interface in suspensions of soft spherocylinders. *Phys. Rev. E*, 71:051716, 2005. `http://dx.doi.org/10.1103/PhysRevE.71.051716`.

[73] E. G. Virga. *Variational Theories for Liquid Crystals.* Chapman and Hall, London, 1994.

[74] J. A. Weideman and S. C. Reddy. A matlab differentiation matrix suite. *ACM Trans. Math. Softw.*, 26(4):465–519, 2000. `http://doi.acm.org/10.1145/365723.365727`.

[75] J. Wilkie. Numerical methods for stochastic differential equations. *Phys. Rev. E*, 70(1):017701, Jul 2004. `http://dx.doi.org/10.1103/PhysRevE.70.017701`.

[76] S. Wolfsheimer, C. Tanase, K. Shundyak, R. van Roij, and T. Schilling. Isotropic-nematic interface in suspensions of hard rods: Mean-field properties and capillary waves. *Phys. Rev. E*, 73(12):061703, 2006. `http://dx.doi.org/10.1103/PhysRevE.73.061703`.

[77] M. Zapotocky, P. M. Goldbart, and N. Goldenfeld. Kinetics of phase ordering in uniaxial and biaxial nematic films. *Phys. Rev. E*, 51(2):1216–1235, Feb 1995. `http://dx.doi.org/10.1103/PhysRevE.51.1216`.

[78] R. Zwanzig and N. K. Ailawadi. Statistical error due to finite time averaging in computer experiments. *Phys. Rev.*, 182(1):280–283, Jun 1969. `http://dx.doi.org/10.1103/PhysRev.182.280`.